Abstract

This thesis contains two projects, both using electron microscopy as the primary technique. In the first project, nuclear envelope budding (NEB) is investigated as an alternate method of transport across the nuclear envelope. We show that NEB is a conserved aspect of eukaryotic cells grown under normal conditions, and that it is upregulated during various types of cellular stress.

In the second part of the thesis, we investigate novel aspects of human flagellar structure using cryo-electron microscopy and tomography. We show that in the tip of human flagella, doublet microtubules can split into two complete singlet microtubules. These singlet MTs contain a helical structure called TAILS, which we hypothesize has a stabilizing effect on the microtubules. Using single particle analysis, we are attempting to identify the proteins that form TAILS by identifying protein domains in the structure. We also reconstructed doublet microtubules from near the tip region, and describe novel microtubule inner proteins, notably large bundles of filaments in the A-tubule.

Publication List

Paper I Dimitra Panagaki* and **Jacob T Croft***, Katharina Keuenhof, Lisa Larsson-Berglund, Stefanie Andersson, Markus J Tamás, Thomas Nyström, Richard Neutze, Johanna L Höög.
*These authors contributed equally to the manuscript.
Nuclear envelope budding is a response to cellular stress. Unpublished manuscript (2021).

Paper II **Jacob T Croft***, Davide Zabeo*, Radhika Subramanian, Johanna L Höög.
*These authors contributed equally to the manuscript.
Composition, structure and function of the eukaryotic flagellum distal tip.
Essays Biochem, 62 (6): 815–828 (2018).
https://doi.org/10.1042/EBC20180032

Paper III Davide Zabeo, **Jacob T Croft**, Johanna L Höög. *Axonemal doublet microtubules can split into two complete singlets in human sperm flagellum tips*. FEBS Lett, 593: 892-902 (2019). https://doi.org/10.1002/1873-3468.13379

Paper IV **Jacob T Croft***, Davide Zabeo*, Vajradhar Acharya, Václav Bočan, Mandy Rettel, Frank Stein, Christer Edvardsson, Lenka Libusová, Mikhail Savitski, Per O Widlund, Radhika Subramanian, Justin M Kollman, Johanna L Höög.
*These authors contributed equally to the manuscript.
Identification and biochemical characterization of TAILS: a microtubule inner complex. Unpublished manuscript (2021).

Contribution Report

Paper I I led the project together with DP under JLH's supervision. I contributed to experimental design and direction of the project. I prepared samples by HPF/FS, imaged, and analyzed data for many of the immuno-EM experiments. I prepared samples for the AZC experiments, which were imaged by DP. Several of the experiments were performed together with DP. Together, DP, JLH and I wrote the manuscript.

Paper II All authors contributed to the writing of the manuscript and made figures. I wrote the sections on the ultrastructure of sensory flagella tips, and the protein composition of the flagella tip, and assisted with editing the other sections.

Paper III I prepared and imaged samples of bovine spermatozoa by HPF/FS. JLH designed the study, and collected the cryo-ET data. DZ and JLH analyzed the data and wrote the manuscript.

Paper IV I led the project together with DZ under JLHs supervision. I developed the method for preparing samples, collected and analyzed the data for SPA. MCJ and JMK supervised and assisted with SPA data analysis. DZ and I both prepared samples for cryo-ET. DZ reconstructed tomograms and performed subtomogram averaging of bovine spermatozoa. DZ and VB developed the method for enriching flagella tips for proteomics. I performed the comparative genomics analysis of the proteomics candidates. DZ and VA assisted in analysis of candidates, and VA and I created homology models and performed fitting of candidate domains. DZ performed the purification and biochemical characterization of DCDC2C, and VB performed the immunofluorescence experiments.

Abbreviations

EM: Electron microscopy

NEB: Nuclear envelope budding

HPF/FS: High pressure freezing & freeze substitution

Cryo-EM: Cryo-electron microscopy

ET: Electron tomography

SPA: Single particle analysis

HPF: High pressure freezing

INM: Inner nuclear membrane

ONM: Outer nuclear membrane

NE: Nuclear envelope

TAILS: Tail axoneme intralumenal spiral

Acknowledgements

So many people have contributed to my journey as a PhD student, it's hard to know where to start. You all have my sincere gratitude.

Johanna, you have been an awesome supervisor. I appreciate how you really care about the team and making sure everybody is happy. You also have a high standard from us without imposing too much stress or expectations. Plus, your passion for EM is contagious!

To my examinator, Richard, thank you for having my best interests at heart. Discussions with you are always interesting. And to my co-supervisors, Per and Gisela, I really valued your input.

Thank you to everybody in my lab, you are the most pleasant and supportive group of people to work with! Davide, thank you for mentoring me when I began. I learned a lot from you! You have such a chill and positive attitude, whenever I came into your office freaking out about something, I left feeling like it would all be OK. Umeå trips would not have been the same without you. Long live your jar of pond scum! Dimitra, thanks for letting me become so involved with the nuclear budding project! It was really fun working on it together. Katharina, you are such a caring person and I admire your boldness and willingness to stand up for what you believe is right. Vaj, it's too bad our time in the lab didn't overlap for very long. I'm confident the flagella project is in good hands with you! Lisa, thank you for always being so willing to drop what you're doing to help anyone with anything they are struggling with. I've never worked with anyone as generous and helpful as you. I was lucky to share our office! Christer, thank you for being so curious and thorough. I learned a lot from the questions you asked. Vašek, you are hard-working and passionate. I'm sad you had to leave before we got to assemble our band. Hopefully one day we can play music together.

To the Kollman lab, thank you for taking me in and making me feel welcome! You have so much EM knowledge collectively and I learned a ton from you. Justin, thank you for taking an interest in my project and being so generous with your resources! Matt, you devoted a lot of time to helping me learn SPA methods, and I really appreciate it, especially considering how little I knew at the beginning. Joel and Quinton, thank you so much for helping me with data acquisition.

Chip and Nick from the UW Male Fertility Lab, thank you for providing samples and being supportive of the project!

Camilla and Michael from the SciLifeLab in Umeå, thank you for helping us acquire tomograms! You never complained even though we brought so many broken grids along with us and had such tricky samples.

Bruno, thank you for helping me with installing software and with solving all of my computer problems.

Hanna, Michelle, Sansan, Joana, Stefanie, Emma, Karl, and Simon, thank you for all of the *interesting* discussions at lunch!

Adam and Ylva, thank you for making me feel so welcome in Sweden!

Kate, it sure hasn't been easy doing our PhDs in different countries, but I'm glad we made it work. Thank you for being so supportive of me throughout this journey. I'm looking forward to never living in different places again. I love you!

And finally, to my family, thank you for being so supportive of my goals even though I decided to live half the world away!

Table of Contents

Chapter 1: Introduction

1.0 Aim of Thesis

This thesis is a compilation of four research papers, all of which use electron microscopy (EM) as the primary technique. These papers concern two independent biological topics; nuclear envelope budding (NEB) and the eukaryotic flagella. Although the two parts to my project cover vastly different aspects of cellular function, they are united by a common theme: Both projects concern observations of mysterious structures inside of cells, and attempt to determine their significance.

This chapter serves as an introduction to EM techniques, with special emphasis on the sample preparation techniques high-pressure freezing/freeze substitution (HPF/FS) and cryo-electron microscopy (cryo-EM). It also highlights electron tomography (ET), and single particle analysis (SPA), both data processing techniques that are used extensively in this thesis to visualize the 3-dimensional structures of organelles and proteins.

Chapter 2 focuses on the findings of **Paper I**, where I present nuclear envelope budding (NEB) as an evolutionary conserved process and investigate the link between NEB and cellular stress.

Chapter 3 introduces the eukaryotic flagellum, with a focus on the distal tip region. The variation of flagellar ultrastructure throughout evolution is explored, while relating findings to the structure of the human flagellar tip. This chapter recapitulates information reviewed in **Paper II**, and data from **Paper III**, and unpublished data are presented.

Chapter 4 explores our attempts to identify TAILS, a helical structure that occurs inside of the microtubules in the tip region of the human sperm flagella. This chapter mainly focuses on the findings of **Paper IV**, in which SPA is used to generate a high-resolution structure of TAILS.

Chapter 5 is an extension of the techniques used in the previous chapter, and applies SPA approach to the doublet microtubule occurring near the tip of human sperm. This chapter will serve as the beginnings of a manuscript, however, at the time of printing this work is ongoing is not yet ready to be presented as a complete manuscript.

1.1 Electron microscopy

1.1.0 Introduction to electron microscopy

Electron microscopy (EM) is a fundamental technique for imaging biological samples at high resolution. Although similar in concept to light microscopy, instead of using visible light to observe samples which has a relatively long wavelength (400 – 700 nm), electron microscopes utilize a beam of electrons which has a wavelength of 2 – 4 pm (depending on the voltage of the microscope). In an ideal system, resolution is limited to half the wavelength of radiation used, although in a real transmission electron microscope resolution is limited to about 1 Å (.1 nm) (1)

which is about the radius of a hydrogen atom and still around 2,000 X greater than is possible by light microscopy. Therefore, while large organelles can be seen by light microscopy, in order to clearly visualize the lipid bilayers separating these compartments, or individual proteins and protein complexes inside the cell, EM must be applied. Although atomic resolution is regularly achieved in material science applications of EM (2), biological tissues are highly susceptible to radiation damage, so the biological sciences have historically lagged behind in the resolution achieved. Therefore, other techniques such as x-ray crystallography and nucleic magnetic resonance were developed to study the molecular structures of proteins. However, during the last decade, the development of direct electron detectors and improvements in computational averaging methods has led to a "resolution revolution" (1), which recently led to the first atomic resolution structure of a protein by cryo-EM (4), a special type of EM in which samples frozen in vitreous ice are imaged. Owing to these recent developments, electron microscopists are more regularly solving protein structures by cryo-EM with comparable resolution to X-ray crystallographic and NMR techniques.

Cryo-EM offers several advantages compared to other two main techniques for studying protein structure; X-ray crystallography and NMR spectroscopy. In X-ray crystallography, the technique that has solved the absolute majority of protein structures, proteins must be highly concentrated and packed into crystals, the formation of which often requires expression of single domains rather than the entire protein of interest. In contrast, cryo-EM samples are studied free in solution. Like cryo-EM, NMR spectroscopy allows study of protein structure in solution, however, it is usually unfeasible to study proteins larger than 35 kDa (5). Although Cryo-EM is most effective for studying large proteins and protein complexes, larger than 100 kDa using SPA, it can extend in sample size to include organelles or small cells using cryo-ET. Recently, cryo-EM was successfully applied to proteins smaller than 100 kDa, indicating this lower limit may be breached more often in the near future (6). Another advantage of cryo-EM, particularly cryo-ET and subtomogram averaging, is that it is not limited to just purified proteins and can be applied to protein complexes in their natural cellular environment (7). This bridges the gap between cell and structural biology, and can provide insights to the biological relevance of structures. Additionally, cryo-EM allows study of heterogenous samples, both in composition and conformation. A beautiful example of this is a study by Behrmann et al, in which 11 functional states of actively translating ribosomes were solved from the same dataset, elucidating mechanistic details of ribosome function and allowing quantification of states and identification of rate-limiting steps (8).

Although X-ray crystallography, NMR, and cryo-EM are often pitted against each other as rival techniques, in reality they are all useful in certain situations and are best used in combination. Lower resolution EM-density maps can be generated for large protein complexes, where previously solved NMR or crystal structures of smaller subunits can then be fitted to determine the arrangement and interactions between subunits (9,10).

Electron microscopes differ in type according to which electrons are used to form the image. Scanning electron microscopes detect scattered electrons, forming an image corresponding to the outside surface of the sample (11). All of the EM data presented in this thesis, however, are the result of transmission electron microscopy, in which electrons that passed through the sample are picked up by a detector on the other side (12). Contrast in the image is obtained when electrons are scattered nonuniformly and do not reach the detector, resulting in darker "electron dense" regions of the image, whereas lighter "electron translucent" regions indicate that a greater number of electrons passed through the sample undeflected. Consequently, information from a 3-dimensional object is compressed into a 2-dimensional image, resembling a semi-transparent shadow of the object. To allow the electron beam to transmit through the sample, thin slices of biological material are often used to study cross sections of cells. However, various 3DEM data processing techniques can be used to recover the 3-dimensional information of larger cell sections or small protein structures.

1.1.1 Overview of EM techniques

A wide range of EM techniques exist, each with its own advantages and limitations compared to the others (13). In general, choosing an EM technique depends upon the sample of interest and the question being asked. Broadly speaking, the EM workflow can be fit into two categories: sample preparation and data acquisition/processing techniques. As sample preparation significantly affects quality of the data collected, good sample preparation is of the utmost importance.

In contrast to light microscopy, in which live cells are imaged in real-time, EM is must be performed in a vacuum and therefore requires sample fixation. Fixation techniques are often classified as room-temperature (conventional techniques), or cryo-techniques (modern) (14,15). Conventional sample preparation techniques require chemical fixatives which cause aggregation artefacts, creating a non-native meshwork of proteins, warping the membranes of organelles and chemically altering proteins (16); while cryo-fixation freezes the sample within vitreous (glass-like) ice, immobilizing it in its natural, hydrated form, without chemical alteration or the formation of ice crystals (17). For this reason, most of the work in this thesis was performed on cryo-prepared samples, with the exception of negatively stained samples, which were used to efficiently screen sample preparation conditions prior to preparation of samples for cryo-EM.

The second step of the EM work flow, data acquisition and processing, also depends on what biological question should be answered. To look at cellular architecture and organelles, image acquisition usually occurs at room-temperature where the samples have been embedded in plastic and heavy metals added to improve contrast. However, to visualize molecular detail the samples need to stay frozen and be imaged in a liquid nitrogen cooled EM – cryo-EM. A drawback to cryo-EM is that radiation from the electron beam can melt the sample and damage biological structures. Therefore, images are acquired at low-dose, resulting in images with very low contrast. The subsequent image processing techniques available ranges from ocular interpretation

of 2D images, to reconstruction of 3D images requiring advanced computational algorithms. The two main 3D-reconstruction techniques are termed electron tomography (ET), and single particle analysis (SPA). Both of these techniques require their own methods for data collection, and will be explained in greater detail later on in this chapter.

1.1.2 Negative stain EM

Negative stain is a sample preparation technique that is quick and easy to perform, and can be very useful for screening a sample before using it in other, more time-consuming methods (18). The "negative stain" used is an aqueous solution containing a heavy metal salt, most often uranyl acetate or uranyl formate (19). The procedure goes as follows: Sample is applied to an EM grid which has been "glow-discharged" (exposed to plasma to increase hydrophilicity), and excess solution is blotted away. A heavy metal stain is then applied on top of the sample, and blotted away to deposit a crust of heavy metal salt over the sample. In this way the stain is both a fixative by creating a solid mold around the biological material, and acts as a contrast agent. Thus, the sample has become "negatively" stained, because the electron dense heavy metal salt occupies the space around the sample, causing the sample to appear white in the image, similar to photographic negatives. In contrast, in techniques such as cryo-EM, the sample itself appears dark in the image (Fig 1.1.2). Since the heavy metal stain, instead of the sample itself, is being imaged by negative stain, information about the inside of the sample is lost and only the shape of the outside surface can be obtained. Nevertheless, this technique provides useful information about general size, shape, and concentration of a sample, and was indispensable for fine tuning a protocol to prepare flagellar microtubules for SPA as detailed in chapter 4, and commonly used as a complement to cryo- sample preparation techniques.

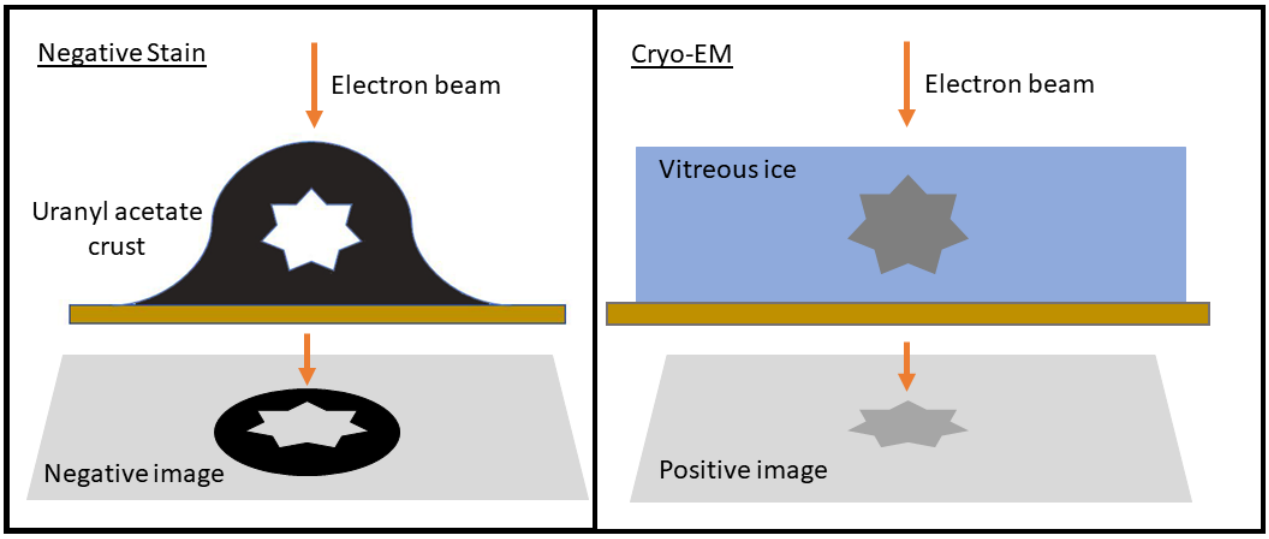

Figure 1.1.2 Image formation in negative stain and cryo-EM

When images are collected of negatively stained samples, the electron beam does not penetrate the heavy metal stain as effectively as the biological sample. Therefore, the outline of the sample appears dark while the sample itself appears light. Thus, the image formed is considered a negative. In cryo-EM, the sample itself appears dark in the images obtained, and information about the inside of the inside of the structure is retained. However, the resulting contrast in the image is much lower than that produced by negatively stained samples.

1.1.3 Cryo-sample preparation techniques

Fixation is achieved in cryo-EM by freezing the sample in a thin layer of vitreous ice. When liquid water forms crystalline ice it expands in volume, thereby rupturing and/or dislocating cellular structures in the vicinity of ice crystals, and therefore the sample must be fully vitrified instead. Vitreous ice can be created either by one of two cryo-preparation techniques; plunge freezing, or high pressure freezing (HPF). Plunge freezing is effective when vitrifying small samples that reside in a thin layer of solution on top of the EM grid such as purified proteins, vesicles, organelles and small cells. The sample is applied to an EM grid, excess liquid is blotted away until only a thin layer remains, and the grid is then plunged into a container of liquid ethane cooled to a temperature of -196 C (17,20). Liquid ethane is used rather than the more easily available liquid nitrogen, since liquid nitrogen boils upon contact with warmer objects forming a bubble of isolating gaseous nitrogen around the sample, preventing vitrification.

In the work presented in the thesis, sperm cells sperm cells were chosen as our model for flagella because they are ideally suited to preparation by plunge freezing. Their small cell bodies only thicken the ice on the grid in their immediate vicinity. Their long, thin flagella on the other hand, are frozen in a thin layer of vitreous ice and can be studied by cryo-EM without any damaging isolation procedures.

While plunge freezing is effective in vitrifying thin samples, thicker samples require higher pressures to delay ice crystal formation initiation and achieve vitrification throughout the entirety of the sample (15). In our studies concerning NEB, we chose to cryo-immobilize cells using a technique called high-pressure freezing. High-pressure freezing is followed by freeze-substitution where a cocktail of heavy metals are introduced to increase sample contrast, and to replace the water inside with a plastic resin, which polymerizes and hardens on exposure to UV light. The sample can then be brought up to room temperature and cut into thin sections using a microtome (Fig 1.2). While this can no longer be called “cryo-EM” and does not allow study of macromolecular structure, it still allows study of organelle structure largely avoiding the artefacts associated with chemical fixation (15,16,21). Plastic embedded cells are then sectioned using an ultramicrotome, and solutions containing heavy metals such as uranyl acetate and lead citrate are applied to permeate cellular material and further increase contrast in images.

Alternate techniques such as FIB-milling and CEMOVIS can be used to image cryo-sections of cells directly without embedding the sample in plastic (22,23), however we have chosen to utilize HPF/FS instead due to its ease of use, and comparatively high-throughput nature.

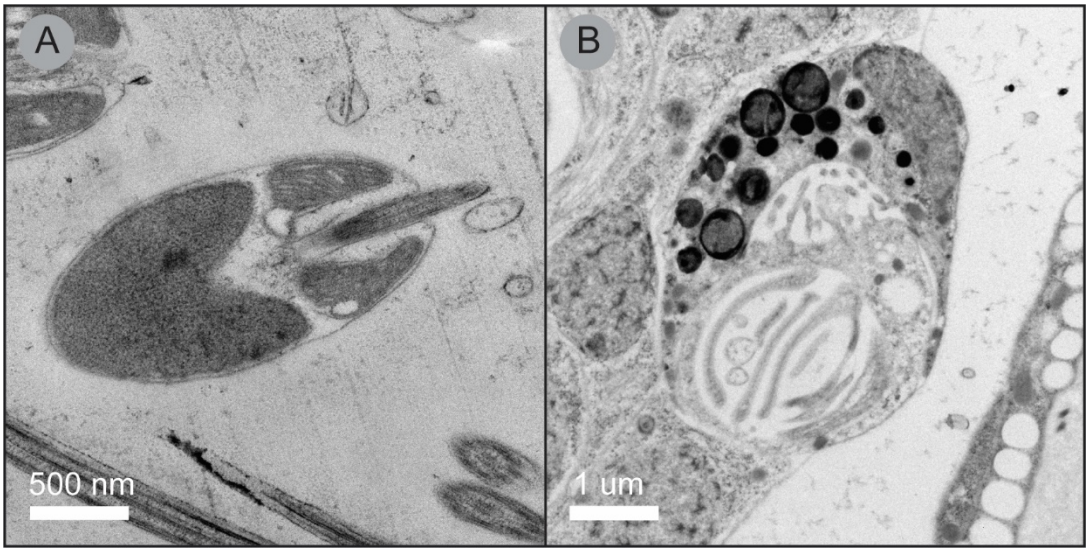

Figure 1.2

Micrographs of samples prepared with high pressure freezing & freeze substitution. (A) Sperm cell head from the blue mussel (Mytilus edulis). (B) The eye of a tardigrade (Hypsibius exemplaris). Scale bars: 500 nm in A and 1 um in B.

Another sample preparation technique that is used extensively in chapter 2 of this thesis is immuno-EM, in which antibodies coupled to gold particles are used to detect specific antigens in samples prepared for EM (24). First, a primary antibody is applied to cell sections prepared via HPF/FS to bind the molecule of interest. Next, a secondary antibody linked to a large gold particle (10 nm in most cases) is applied to the sections, which binds the primary antibody. The gold molecule then appears as an electron dense circle in images, and marks detection of an antigen on the surface of the cell section. Cryo-preparation of cells does not chemically alter antigens by fixation, therefore reactivity towards antibodies is often retained. However, as antibodies can bind non-specifically, it is important to validate the specificity of an antibody before interpreting the results of an immuno-EM experiment. Labeling of a specific structure must be validated in images of many different cells, using other cellular structures as positive and negative controls.

1.1.4 3-Dimensional electron microscopy of cells and tissues

Several techniques can be used to recover the 3-dimensional information that is compressed in 2-dimensional electron micrographs One such technique, electron tomography (ET), combines images acquired from multiple angles to generate a 3-dimensional digital "volume" called a tomogram. ET is performed using a series of images of the same region of sample acquired at various "tilts", which refers to the physical tilting of the stage upon which the sample is held inside the microscope. These tilted images can then be used to calculate a tomogram in one of several existing software via a process called back-projection (25). Calculation of a quality tomogram requires accurate alignment of the tilt-series, therefore gold particles are often added

to aid in alignment. ET can be applied to both thick plastic sections, and thinner cryo-samples. ET offers the advantage that a thick sample can be imaged, and the structures within can be viewed from multiple angles providing a more revealing picture than a single 2D section could, making it indispensable when visualizing large and complicated cellular structures.

1.1.5 3-Dimensional electron microscopy of macromolecules

Due to the low signal-to-noise ratio of cryo-micrographs, computational averaging methods must be used to obtain high resolution 3D structures of macromolecular complexes. These methods fall under two categories; subtomogram averaging and single particle analysis (SPA), differing in the type of data that is averaged. Subtomogram averaging combines many small 3D cubes of data called "subtomograms" or "subvolumes" extracted from larger tomograms, while SPA uses segments of 2D images called "particles" corresponding to different views of thousands of copies of the same molecule. SPA regularly results in near-atomic resolution structures, while subtomogram averaging currently rarely breaks past the nanometer scale (26). However, SPA can usually only be applied to purified proteins, while subtomogram averaging is often applied to structures *in situ.* Both techniques have their advantages and disadvantages, and often the best approach to study complicated cellular processes will include the combination of both these techniques.

While subtomogram averaging was fundamental to the initial observations that led to my project (27), I mostly utilized SPA and thus will explain the method in greater detail here. First, a solution containing purified proteins or protein complexes is applied to glow-discharged EM grids and vitrified via plunge freezing. An ultra-fast series of micrographs are taken as "movies" of the same region of the sample. The first few images, when the sample tends to move more, and later frames can then be removed if the cumulative electron dose incurs radiation damage on the sample, and the remaining beam-induced motion of the particles can be corrected by aligning frames. Alignment of frames, termed "motion-correction", is the first step of data processing and effective algorithms have been developed for this process (28). In the next step micrographs must be "CTF-corrected", to restore proper contrast to the image. Due to the low signal-to-noise ratio of cryo-EM, micrographs are collected out of focus to enhance contrast and allow identification of particles (29). "Defocus" values correspond to the distance between the focal point and the sample, and contrast in the image is affected by the contrast transfer function (CTF) which is a product of defocus and aberration of the lens (30). Effects of the CTF become more severe at higher frequencies, so accurate calculation of the CTF for each micrograph must be determined in order to restore high-resolution structural information. Once micrographs have been CTF-corrected, particles can be picked either manually (by clicking on them), or by the use of image recognition software (31). Once particles have been selected, they are extracted, meaning square boxes around each particle are saved as individual images. Filamentous particles, are picked as start and end points with a line drawn between them along the length of the filament, and overlapping boxes are extracted with an interval corresponding to the length of each subunit (32). Pseudo-helical filaments such as microtubules require special considerations

in subsequent steps (33,34), which will be discussed in more detail in Chapter 4.2. The basic SPA pipeline is described here.

The next steps of single particle analysis serve to eliminate low-quality particles and align the particles to each other to create a 3-dimensional image. First, 2D-classification and averaging separates particles into classes, in which each class is a different view of the particle. If structural heterogeneity exists, it can be separated at this stage and low-quality particles are removed. Particles from classes that seem biologically relevant then move on to 3D refinement, in which each particle is assigned a set of three Euler angles (ϕ, θ, ψ) that describe the rotation of that view of the particles with respect to the others (Fig 1.3).

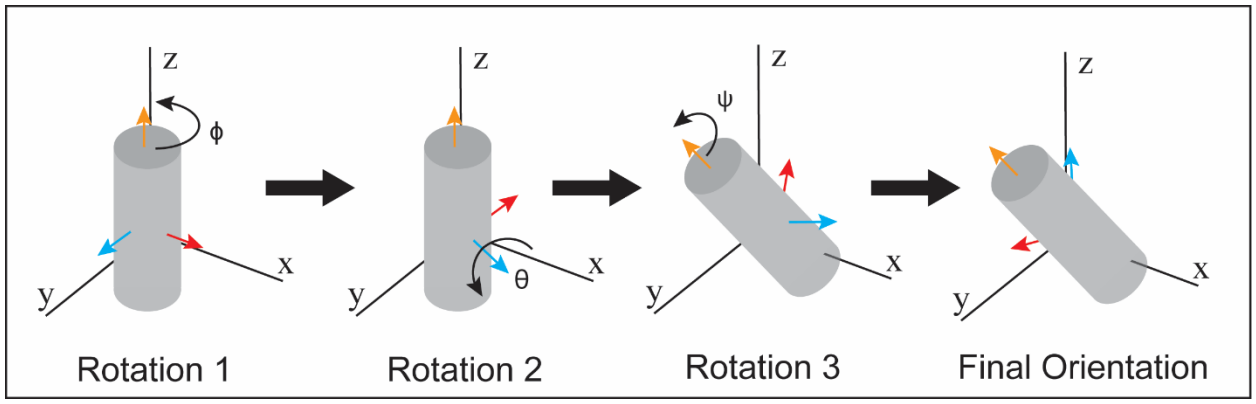

Figure 1.3

The orientation of a particle can be described via rotations around 3 Euler angles. The most common convention is first a rotation around the z axis (ϕ), then a rotation about the y axis (θ), and finally a rotation about the z axis again (ψ). These rotations are defined as rotations about the axes of the particle itself, not the space that it is rotated in.

A variety of programs exist to perform 3D alignment, all of which rely on iterative alignment of particles in Fourier space (35–37). Angles are fine-tuned during each iteration until more accurate orientations cannot be found. To reduce overfitting of noise, 3D maps are created by the correlation of two "half-maps" which are each generated by randomly chosen subsets of particles. After an initial alignment is obtained, 3D classification can be used to once again sort heterogenous samples. In this step, the user specifies the number of classes based on the amount of heterogeneity expected in the sample. The refinement process is similar to 3D refinement, except in each round particles are divided into subsets and multiple 3D structures are obtained, one corresponding to each class. After 3D classification, identical classes are combined and unique classes are separated for continued 3D refinement. Several tricks exist to improve resolution such as masked refinement to better align individual regions of a flexible structure, and "particle polishing", which improves movie-alignment for each particle individually (38), and application of symmetry. CTF-correction can also be improved for each particle at this stage

to account for variations in defocus resulting from height of each particle in the ice, and the ice layer not being perfectly flat with respect to the image. Once a final 3D electron density map has been obtained, various modeling tools can be used to create a molecular model of the protein.

My approach to applying SPA to the microtubules of human sperm flagella was a bit unconventional as we did not know the identities of proteins binding our microtubules beforehand. Details of our approach are discussed in chapters 4 and 5.

Chapter 2: Nuclear envelope budding is a response to cellular stress

2.0 Introduction

Perhaps the most definitive characteristic of Eukaryotes is the nucleus, in which the cells genetic material is enveloped in a double lipid bilayer, insulating it from the rest of the cell. The nucleus is not accessible to material in the cytoplasm, guarded by selective pores called nuclear pore complexes (NPCs) that facilitate selective translocation across the nuclear envelope (39). Classically, the NPC is accepted as the only known passage between the nucleus and cytoplasm during normal cellular function. However, in virus-infected cells, an alternative method of nuclear export has been described. Herpes simplex virus, which replicates in the nucleoplasm, is released into the cytosol via outwards budding of the nuclear envelope (40,41). Since 1955, there have also been many observations and reports suggesting that such nuclear budding (NEB) probably occurs in healthy cells as well, although the phenomenon has received little attention due to lack of mechanistic details and has mostly been written off as an oddity of developing organisms (42–46). Recently, however, some mechanistic insight was gained when it was discovered that NEB events in *D. melanogaster* contain large ribonucleoprotein granules, but whether this function is consistent in other cell types still remains unknown (47,48). Furthermore, ESCRT proteins have been implicated in the membrane remodeling process (49). The proteins Chm7 and Heh1 were shown to function together to monitor the integrity of the NE and trigger sealing of breakages via the ESCRT pathway. Correlative light and electron microscopy showed NEB events at sites of Chm7 activation, although the precise function of these structures is still unclear.

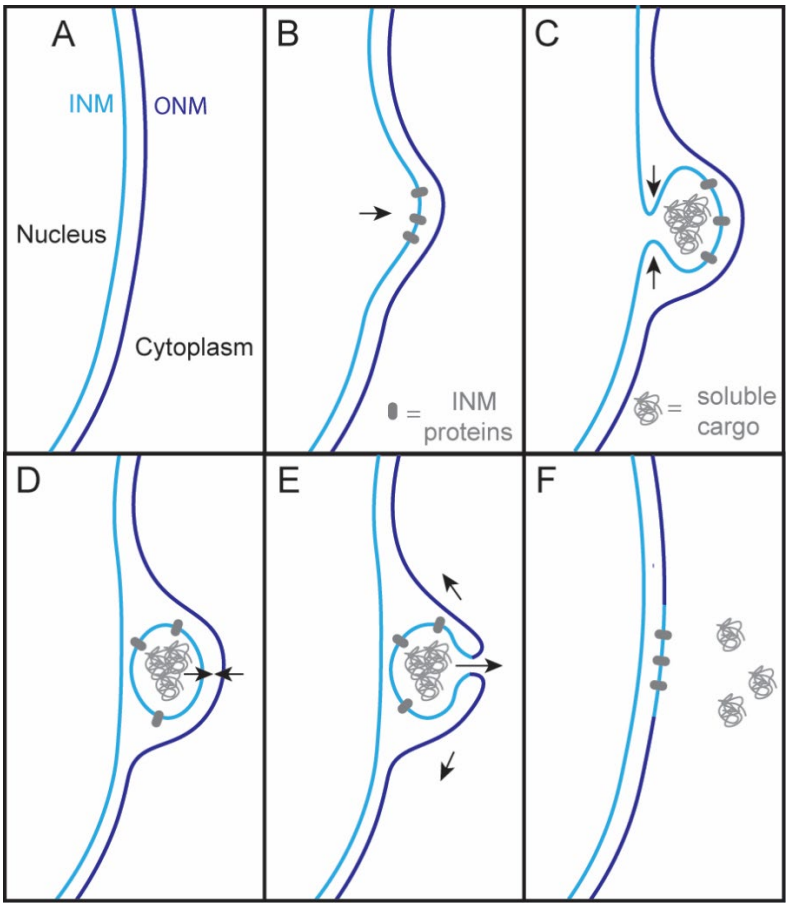

Figure 2.1 Export of soluble cargo or INM components by NEB

NEB provides a mechanism by which soluble cargo, as seen in nuclear egress of HSV viral particles (40,41)*, or INM components could be transferred to the cytoplasm or ONM & ER, respectively. (A) Normal morphology of the NE, in which the INM and ONM lie side by side without much separation between them. (B) The INM protrudes slightly, causing the ONM to protrude as well. Certain INM components could be targeted to this protruding region. (C) The INM continues to protrude, and eventually starts to seal, forming a small vesicle in the perinuclear space connected to the INM by a narrow "neck". Possibly, soluble cargoes in the nucleoplasm could be enveloped in the forming vesicle. (D) The neck linking the INM and vesicle is completely sealed, and the vesicle begins to fuse with the ONM. (E) The vesicle now becomes continuous with the ONM, and soluble cargoes are released into the cytoplasm. (F) The NE reforms its original, flat shape. Both lipids and proteins from the INM have now been transferred to the ONM, where they can diffuse or be transported to the ER membrane.*

Evidence that material can be exported from the nucleus via this alternate route has led to speculation that other cargoes, for example protein aggregates, could be removed from the nucleus by NEB (50). Protein misfolding can be highly toxic to the cell, and can even result in

mutagenesis, which demonstrates the importance of protein quality control in the nucleus (38). Therefore, several mechanisms exist to cope with aggregation of nuclear proteins such as chaperones and the ubiquitin-proteasome system (51–53). During cell stress such as heat shock, large scale protein misfolding occurs and misfolded proteins can be shuffled both in and out of the nucleus between various protein quality control compartments (52). Since protein aggregates as a whole can be much larger in size than the size limit of the NPC, a possible function of NEB could be to rapidly export a large quantity of toxic cargo from the nucleus for degradation in the cytoplasm, although this function is very speculative.

In addition to protein quality in the nucleus and cytoplasm, the endoplasmic reticulum (ER) is well equipped with its own set of degradation pathways, to contend with the large quantity of newly synthesized proteins entering the ER (54). Degradation at the ER is highly dependent on the ubiquitin proteasome system, and facilitates removal of both soluble and membrane proteins. Similarly, degradation of INM proteins can occur via biochemically similar pathways to ER-associated degradation of membrane proteins (55). Although several branches of INM-associated degradation exist, each relies on a different E3 ubiquitin ligase to recognize and tag misfolded substrates. Another speculative function of NEB could be the transfer of INM components to the ONM and ER membranes, which are continuous. It is plausible, that during cell stress, the INM-associated degradation pathways cannot keep up with the quantity of misfolded proteins generated, and the excess must be transferred to the ER for degradation.

The aim of this project is to determine the function of NEB, and investigate a possible connection to protein misfolding by studying how various cellular stressors affect NEB. Prior to my involvement in the project, another student in our lab investigated cells of 5 different organisms grown under normal conditions and using thin section EM of cells prepared by HPF-FS. It was found that the nuclei of all organisms investigated exhibit rare NEB events during normal cellular function, confirming that NEB is a conserved cellular process. ET-models revealed the 3D structure of NEB events in two of the organisms, revealing that a complete vesicle was contained in between the inner nuclear membrane (INM) and outer nuclear membrane (ONM). Together we worked to investigate the link between NEB and cellular stress, and investigate potential cargoes transported by NEB (Fig 2.1). This chapter presents the findings of **Paper I**, which is a manuscript that is currently in submission.

2.1 Methodology

High-pressure freezing of cells for electron microscopy. All cells were loaded into aluminum specimen carriers and were high-pressure frozen in a Wohlwend Compact 3 (M. Wohlwend GmbH, Sennwald, Switzerland). A short freeze substitution protocol was applied, using 2% uranyl acetate dissolved into acetone (UA; from 20% UA stock in methanol) for one hour (56). The UA incubation was followed by two washes in 100% acetone for one hour each. Before embedding, the temperature was raised from -90ºC to -50ºC overnight with a rate of 3ºC/h. Samples were then embedded in K4M or HM20 resin in increasing concentrations of 20%, 40%,

50%, 80% and finally three times in 100% plastic (2 hours per solution). Polymerization of the plastic occurred over 48h using UV light at -50ºC followed by 48h in room temperature. (57) All samples were cut into 70 nm thin sections and placed on formvar coated copper grids. Sections were stained with 2% UA for 5 minutes and Reynold's lead citrate for 1 minute.

Treatment with AZC. For the AZC experiments, a logarithmically growing *S. cerevisiae* culture in YPD media at a temperature of 30 ºC was split into two flasks. One flask was treated with AZC to a final concentration of 1 mg/mL. Samples of the AZC treated culture were high-pressure frozen after 30 and 90 minutes. The untreated culture was high-pressure frozen as a control an hour after the culture was split.

Preparation of sections for immuno-electron microscopy. For the immunolabeling experiments, the same high-pressure frozen samples embedded in HM20 resin were used. Grids with 70 nm thick sections were fixed in 1% paraformaldehyde (PFA) in PBS for 10 minutes. After three PBS washes of 1 minute each, samples were blocked with 0.1% fish skin gelatin and 0.8% BSA in PBS for 1 hour. For detection of NPC proteins, grids were then incubated in a 1:50 dilution of mAb414 (BioLegend, San Diego, USA) for two hours, followed by a 1:150 dilution of rabbit anti-mouse immunoglobulins (Agilent/Dako, Glostrup, Denmark) for an hour, and then a 1:70 dilution of 10 nm gold-conjugated protein A (CMC UMC Utrecht, The Netherlands) for 30 minutes. For labeling of ubiquitin, grids were incubated in a 1:20 dilution of antibody ab19247 (Abcam, Cambridge, UK) for 2 hours, followed by a 1:20 dilution of Goat-anti-Rabbit IgG 10 nm gold (Electron Microscopy Sciences, Hatfield PA, USA) for an hour. All incubations were performed at room temperature, except for the primary antibody which was kept at 4ºC. Three washing steps (20 min in PBS) were carried out after incubations with each antibody. 2.5% glutaraldehyde was applied to sections for 1 hour followed by three washes (1 min in dH_2O). Sections were then contrast stained in 2% UA for 5 minutes (wash 3x 2 min in PBS) and 1 minute in Reynold's lead citrate (washed 5x 1 min in PBS).

For a more detailed description of the methods, readers are referred to the methods section of **Paper II.**

2.2 NEB increases during heat shock

To investigate whether NEB is involved in the cellular stress response, a mild, constant heat shock (38ºC) was applied to *S. cerevisiae* cells for up to 90 minutes, with samples being cryo-immobilized for electron microscopy at various points along that time. This technique simultaneously visualizes NEB events and protein aggregates which appears as electron dense content (EDC) inside the nucleus. Between 60 to 80 electron micrographs were acquired of randomly chosen cell sections for each time point, all containing a nucleus. NEB events contained visible lipid bilayers enclosing electron dense material with an internal structure resembling the nucleoplasm (Fig 2.2A). Images were scored both for presence of NEB events and EDC in the nucleus (Fig 2.2B). Both NEB and EDC increased during heat shock, before decreasing again near the end of the time course, potentially showing a cellular adaptation to the

new temperature (Figure 2.2B). EDC reaches a maximum (82% of sections) after 15 minutes, and stays relatively stable at this level before decreasing by 90 minutes, at which it is only present in 60% of sections. NEB events were found in 1.3% of cellular sections in undisturbed cultures, but increased to 10.3% after 30 minutes of heat shock. The coincided increase in frequency of NEB and protein aggregation led to the hypothesis that NEB may indeed have an important function during the cellular stress response. NEB could function to remove nuclear protein aggregates, remove material from the INM, or perform a signaling role by transporting RNPs similar to the role of NEB of *D. melanogaster* embryos. All of these possibilities assume a transport of material out of the nucleus, owing to the fact most observed NEB events protrude outwards. However, since directionality cannot be established in our images, we cannot exclude nuclear import as a possibility. Another possibility is that increased membrane fluidity resulting from heat shock is adjusted for by storage of specific membrane components within NEB events. Although the function of NEB remains unclear, we moved on to investigate its involvement in other stress responses to see whether the function is heat-shock specific, or more general.

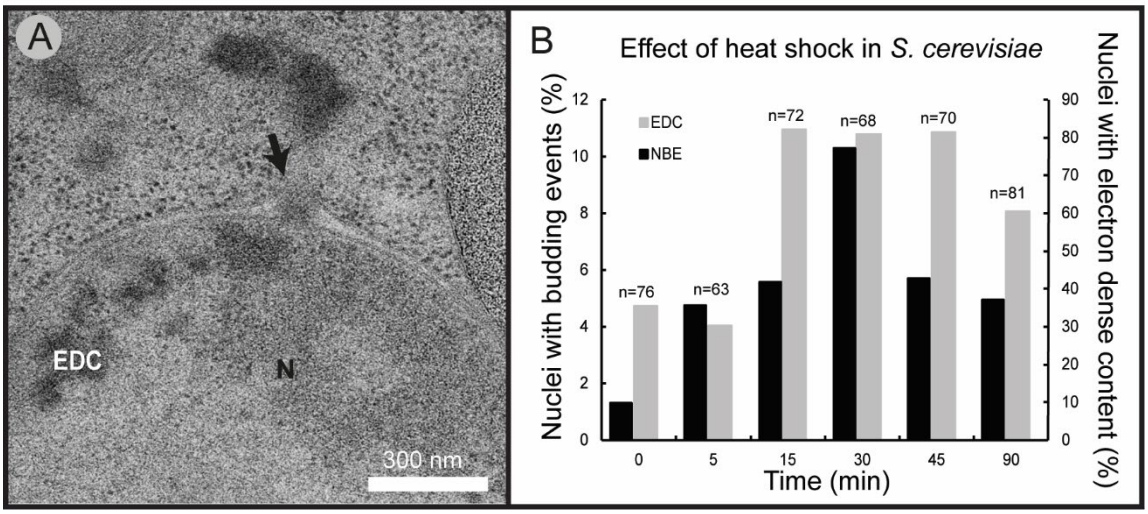

Figure 2.2 – The effect of heat shock on NEB in S. cerevisiae

(A) Electron micrograph showing an example of a NEB event in a S. cerevisiae cell that was exposed to heat shock. (B) The frequency of NEB and EDC increased during heat shock in S. cerevisiae, with a peak occurring after about 30 minutes. Abbreviations: N, nucleus; EDC, Electron Dense Content (protein aggregates); Black arrow points out NEB event.

2.3 NEB increases in response to 4 other cellular stressors

After the discovery that NEB increases during heat shock, we investigated whether other stressors also resulted in an increase in NEB or whether this was unique to heat shock. Exposure to sodium arsenite, hydrogen peroxide, and cellular aging were all found to result in an increased

frequency of NEB as well (Fig 2.3A-D). Young control cells for the aging experiment also exhibited an increase in NEB (this value happened to fall just below the cutoff of our statistical test for significance), likely due to the mechanical handling involved in isolating old cells, although the increase was lesser than that observed in old cells. All the stressors tested above have been shown to create aggregation of misfolded proteins in the cytoplasm and the nucleus (58–60). In order to investigate whether or not the observed increase in NEB events is specifically triggered by proteotoxic stress, we examined *S. cerevisiae* cells after treatment with azetidine-2-carboxylic acid (AZC).

AZC competes with proline for incorporation into proteins, but due to the presence of one fewer carbon atom in its ring, it forces the amino acid backbone into an unnatural conformation, resulting in protein aggregation (61,62). Cells grown at normal temperature (30ºC) were treated with AZC, and cryo-immobilized by HPF before, and after 30 and 90 minutes of treatment (Fig 2.3E-F). The NEB frequency appeared unchanged after 30 min of AZC exposure compared to untreated cells (2.6% n= 114 sections and 3.1% n= 161 sections, respectively). However, after 90 minutes of exposure to AZC NEB events had a dramatic increase in frequency reaching 22% (n= 100 sections), which was the greatest increase measured among the stressors tested. This NEB increase shows a direct link between the NEB pathway and cellular response to proteotoxic stress. Furthermore, the increase in NEB due to other stressors makes the hypothesis that NEB is a mechanism for regulating membrane fluidity unlikely, since these stressors do not have the same effect as temperature change on membranes. We therefore hypothesized that misfolded proteins in the nucleoplasm or INM are removed by NEB, although the contents of the NEB events and machinery involved in bud formation remain unclear.

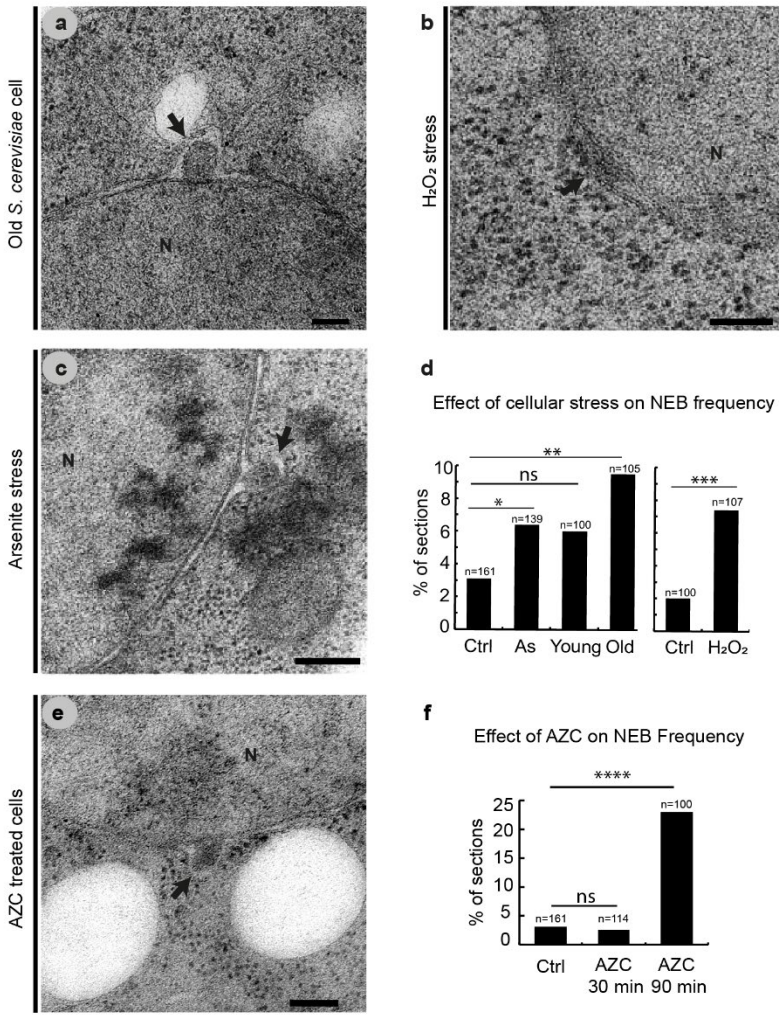

Figure 2.3 Four different cellular stressors increase NEB frequency in S. cerevisiae cells

*Thin sections containing NEB events in cells exposed to 4 different cellular stressors: (**A**) Aging (n=105) (**B**) oxidative stress caused by hydrogen peroxide exposure (n=107) These cells were grown in different media than the other conditions and required a separate control (n = 100) (**C**) exposure to sodium arsenite (n=139). (**D**) Percentage of nuclei containing NEB events in cells in each stress condition compared to control cultures (n=161) grown under normal conditions. Young cells (n=100) were also examined after separation from old cells and show an increase in NEB compared to the control. (**E**) Thin section containing a NEB event in cells treated with AZC, a chemical which causes proteotoxic stress. (**F**) Percentage of nuclei exhibiting NEB events before as well as 30 and 90 minutes after treatment with AZC (n=161, 114, 100 respectively). Scale bars 200 nm. Abbreviations: NEB, nuclear envelope budding; N, nucleus; black arrows indicate NEB events. *P<.05, **P<.01, ***P<.001, ****P<.0001 vs. control; ns no significant differences between groups.*

2.4 Ubiquitin localizes to NEB

The observation that protein misfolding can trigger an increase in NEB led us to hypothesize that NEB may function to transport proteins across the nuclear envelope to be degraded. Most proteins that are destined for degradation through the proteasome system must first bind to a poly-ubiquitin chain (63). Furthermore, ubiquitin signaling is known to target cytosolic proteins and organelles for degradation by autophagy (64). Possibly, the population of proteasomes in the nucleus cannot cope with such high levels of misfolded proteins during cellular stress so large aggregates must be transported out of the nucleus by NEB for storage, degradation via cytoplasmic proteasomes, or autophagy. Another intriguing possibility is that misfolded INM proteins are removed by NEB.

To probe if the NEB cargo is targeted for protein degradation via ubiquitin signaling, I performed immuno-EM on *S. cerevisiae* cells with a polyclonal antibody that has a stronger affinity to poly-ubiquitin chains than monomeric ubiquitin (Abcam ab19247). The secondary antibody is coupled to a gold particle for detection under the electron microscope. In order to increase the NEB events visualized, cells were subjected to 30 minutes of heat shock. Images of 60 randomly chosen cell sections were recorded and the number of gold particles per area of various cell structures were quantified to establish specificity of the antibody (Fig 2.4A). Lipid droplets were used as a negative control (4 gold particles/um^2). Autophagosomes were chosen as a positive control (67 gold particles/um^2) due to the role of ubiquitin in targeting cargoes for selective autophagy (65). Nucleoplasm (excluding areas containing EDC), did not differ from the negative control (4 gold/um^2). However, EDC was labeled fivefold more frequently (21 gold/um^2) than lipid droplets (Fig 2.4B). Due to the relative rarity of NEB events compared to other organelles, additional NEB structures were specifically found and recorded to increase the number of examined ubiquitin labeled events (n=12). NEB events were labeled fourfold more frequently with the anti-ubiquitin antibody than lipid droplets (18 gold/um^2) (Fig 2.4C). These results confirm the presence of ubiquitin in both EDC and the NEB events found during heat shock in *S. cerevisiae*. Therefore, we hypothesize that the contents of NEB are targeted for degradation via a ubiquitin-dependent pathway.

Upon visual inspection, we noticed that many of the labeled NEB events appeared to be labeled near the membrane of the vesicle contained in the perinuclear space. Indeed, this observation was confirmed when 88% of gold particles were found within 30 nm, the length of the antibody sandwich used, either side of the NEB membrane. However, due to the small size of NEB events, most of the area within the vesicle is within 30 nm of the membrane, so it is difficult to judge whether the membrane or the contents of the vesicle have been labeled by this metric. We reasoned that if the membrane was the true structure that was labeled, gold particles should be equally likely to be located on either side of it, so if the distance of each gold particle were added the result should be close to zero. Instead, it was found that gold tended to be slightly within the NEB event, with an average distance of 5 nm towards the inside of the bud. Therefore, we conclude that two possibilities exist to explain the localization of gold: First, INM components

targeted for degradation could be ubiquitylated and removed via NEB, or a component of the bud membrane could recognize and bind soluble ubiquitylated proteins. In both cases the ubiquitin tag would be located near, but slightly inside the membrane of the vesicle within the NEB event.

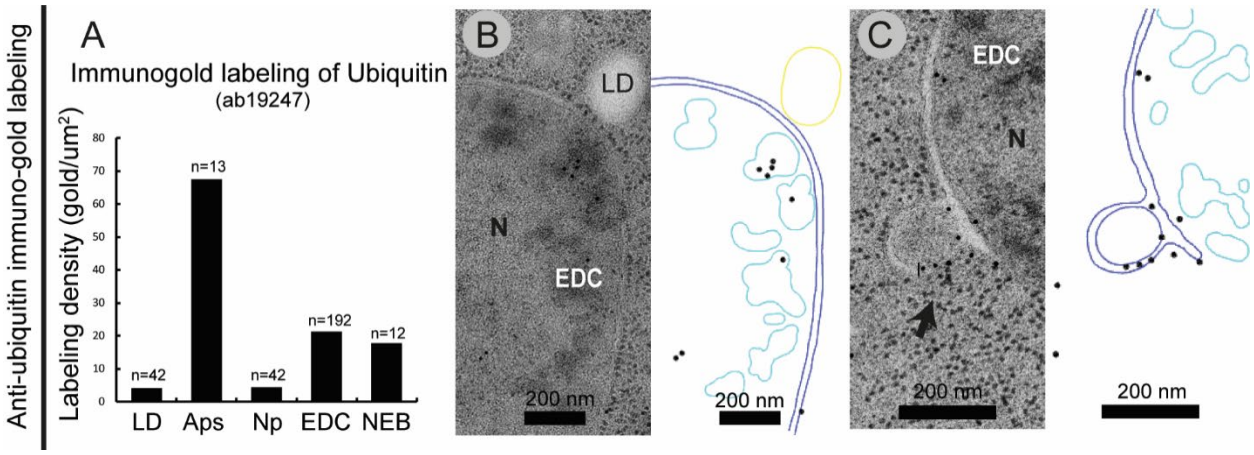

Figure 2.4 NEB events contain ubiquitin

Ubiquitin was detected inside of NEB events by immuno-electron microscopy. (A) Labeling of various organelles by Abcam antibody ab19247. (B) Ubiquitin was detected in nuclear electron dense content (protein aggregates). (C) Ubiquitin also localized to NEB events. Cartoons are drawn to the right of micrographs to more clearly illustrate location of gold particles. Abbreviations: LD, Lipid Droplet; Aps, autophagosome; Np, nucleoplasm; EDC, electron dense content; NEB, Nuclear Envelope Budding; N, nucleus.

2.5 NEB does not contain aggregated Guk1-7-GFP

The link established between NEB and cellular stress and the discovery that NEB events contained ubiquitin led to the hypothesis that misfolded proteins tagged with ubiquitin could be transported by NEB events. Aggregates of misfolded proteins are sequestered into various quality control compartments in *S. cerevisiae.* The two cytosolic compartments are known as the JUNQ, located beside the nucleus, and the IPOD which is located near the vacuole (66). It was later discovered that a portion of the JUNQ actually resides inside the nucleus, and this compartment was named the INQ (67). Ubiquitylated proteins amenable to degradation by proteasomes or refolding by chaperones are targeted to the JUNQ or INQ, while more toxic permanently insoluble aggregates such as amyloids are targeted to the IPOD (68). Shuffling of proteins between the JUNQ and INQ was shown to be dependent on the NPC component Nup42, however cytosolic aggregates are still found to enter the nucleus in Nup42 deletion strains much more slowly, implying Nup42 is not required for import and another mechanism may exist.

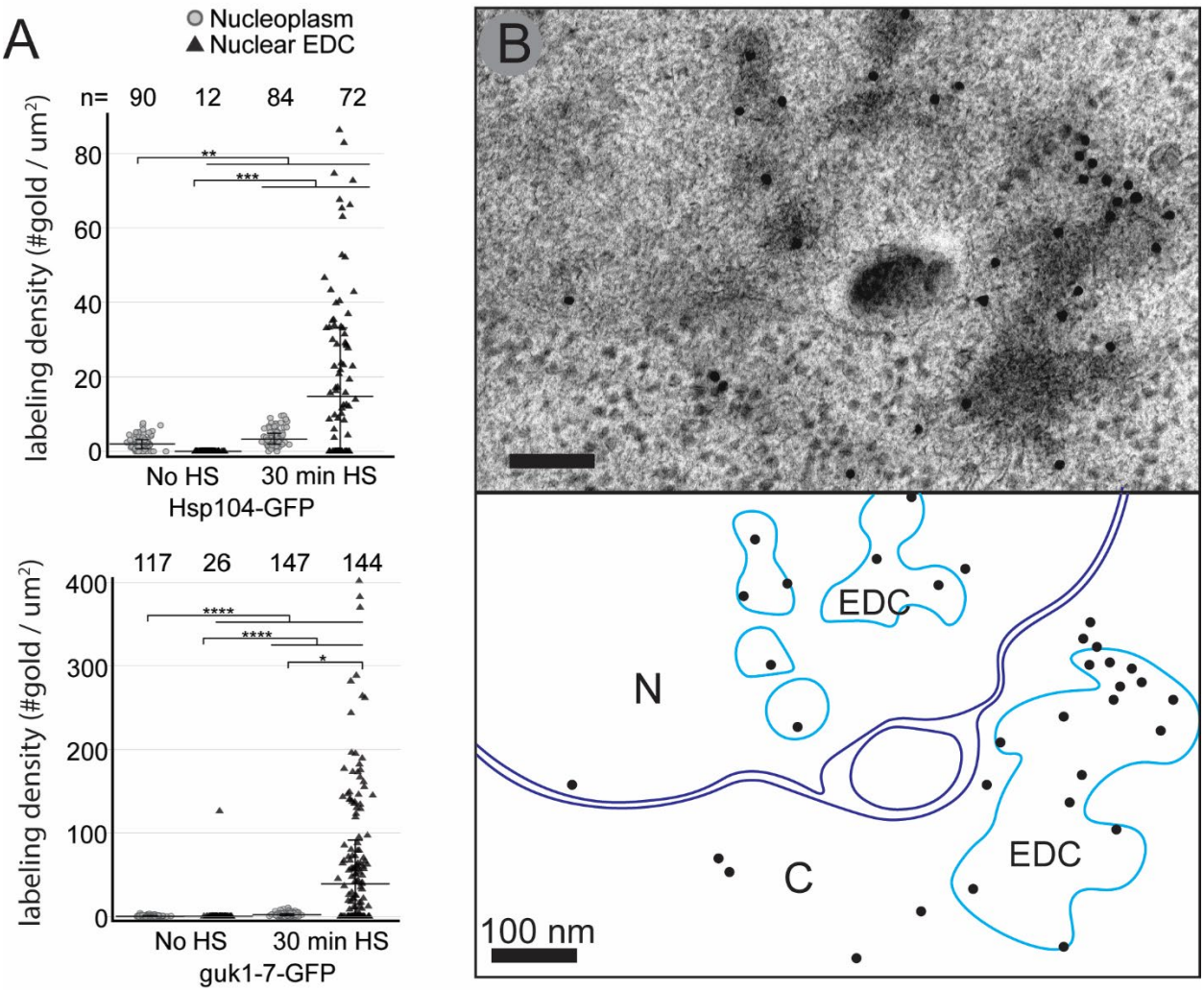

Figure 2.5 Guk-1-7-GFP forms nuclear aggregates during heat shock, but is not transported by NEB

(A) Immuno-gold labeling of Hsp104-GFP and Guk-1-7-GFP in nuclear protein aggregates (nuclear EDC) compared to the nucleoplasm (defined as area in nucleus no including aggregates) under normal conditions, and after 30 minutes of heat shock. Both proteins localize to nuclear aggregated during heat shock. (B) A representative micrograph demonstrating Guk-1-7-GFP is detected by immuno-EM in nuclear and cytoplasmic aggregates (EDC), but not NEB events. Below, a cartoon representation is drawn to aid in visualization of gold molecules. Scale bars: 100 nm.

To test whether NEB was involved in transport of ubiquitylated proteins between the JUNQ and INQ, we performed immuno-EM against Guk-1-7-GFP, a thermally unstable protein that is ubiquitylated in the cytosol and is degraded by proteasomes in cytosolic and nuclear compartments (69,70). Using immuno-EM, we localized Hsp104-GFP to the clusters of electron dense content in the nucleus, confirming that these clusters represent aggregations of misfolded proteins (Fig 2.5A). Then we checked for the presence of Guk1-7-GFP in these nuclear

aggregates, confirming that the protein does aggregate during heat shock (Fig 2.5A). Next, we scanned the grid for NEB, and did not detect guk-1-7-GFP at any of the NEB events (n=5). Therefore, we concluded that either NEB is not involved in shuttling ubiquitylated protein aggregates between the JUNQ and INQ for proteasomal degradation, or if it is, guk-1-7 specifically is not shuttled by this process. Since insoluble, toxic protein aggregates that may form harmful interaction with protein quality control machinery are targeted to the IPOD instead, it remains a possibility that these aggregates cannot be translocated across the NPC and are instead removed from the nucleus by NEB. However, since components of the IPOD are not ubiquitylated, this seems an unlikely candidate due to the presence of ubiquitin at NEB events. Due to the proximity of ubiquitin to the NEB membrane, and the absence of soluble aggregates such as guk-1-7-GFP in NEB events, a function in transferring ubiquitylated INM components to the ONM and ER seems more likely.

2.6 NEB and NPC malfunction are distinct phenomena

When certain key genes required for NPC assembly are deleted, herniations of the nuclear envelope similar to NEB events are observed (71). These herniations have a distinct morphology, which includes a 'neck' resembling formation between the vesicle and the INM. In another recent paper that investigated an ESCRT-mediated surveillance system for damage to the NE, the morphologies of two types of NEB were examined by cryo-ET (49). It was found that both had distinct morphology, in which the "neck" connecting the NEB-event to the INM was larger in herniations caused by NPC malfunction than in NEB caused by activation of ESCRT protein Chm7, and it was concluded that although both appear similar, they are in fact two distinct processes. Another recent study performed subtomogram averaging on the necks of NEB caused by NPC malfunction. It demonstrated that the neck of these herniations are partially formed NPCs that have been sealed off. Finally, another publication studying the effects of aging on the quality control of NPCs in mitotic cells, had also observed an increase in NEB (referred to as nuclear envelope herniation) in aged cells compared to a mixed population, and concluded this was the result of NPC malfunction (72).

In an attempt to clarify if our observations of NEB are result of malfunctioning NPCs or another process, we performed immuno-EM using an antibody that recognizes four NPC components (Nup62, Nup153, Nup214 and Nup358) on both undisturbed *S. cerevisiae* cultures (Fig 2.6A-C) as well as the aged cells (Fig 2.6D). We selected this antibody because it has been used successfully in immuno-EM experiments (73). However, we still wanted to validate the effectiveness of the antibody, so we first quantified labeling of intact NPCs in our sections in micrographs of randomly chosen cells. In both wild type and aged cells, the majority of NPCs observed were labeled by gold particles (67% in wild type with n = 95 NPCs, 81% in aged cells with n = 100) (Fig 2.6E). We chose to quantify nonspecific labeling by counting the number of lipid droplets that contained a gold molecule in each sample (4.8% in wild type with n = 82 lipid droplets, 8% in aged cells with n=100) (Fig 2.6E). Since lipid droplets are much larger than NPCs, the specificity is even greater than the percentages would indicate but we chose not to use

gold/area as a metric since the area of a single NPC is so small. The immuno-labeled sections were then scanned for NEB events. In wild type cells, only in one case was a NEB event labeled (16.7 %, n=6) whereas all the rest were unlabeled. Similarly, in aged cells there was one NEB event of atypical morphology that was labeled by one gold particle (10%; n= 10). We concluded that although a small subset of the nuclear envelope herniations that we classify as NEB may in fact be NPC-related structures, the vast majority of NEB events in our data are distinct from NPCs.

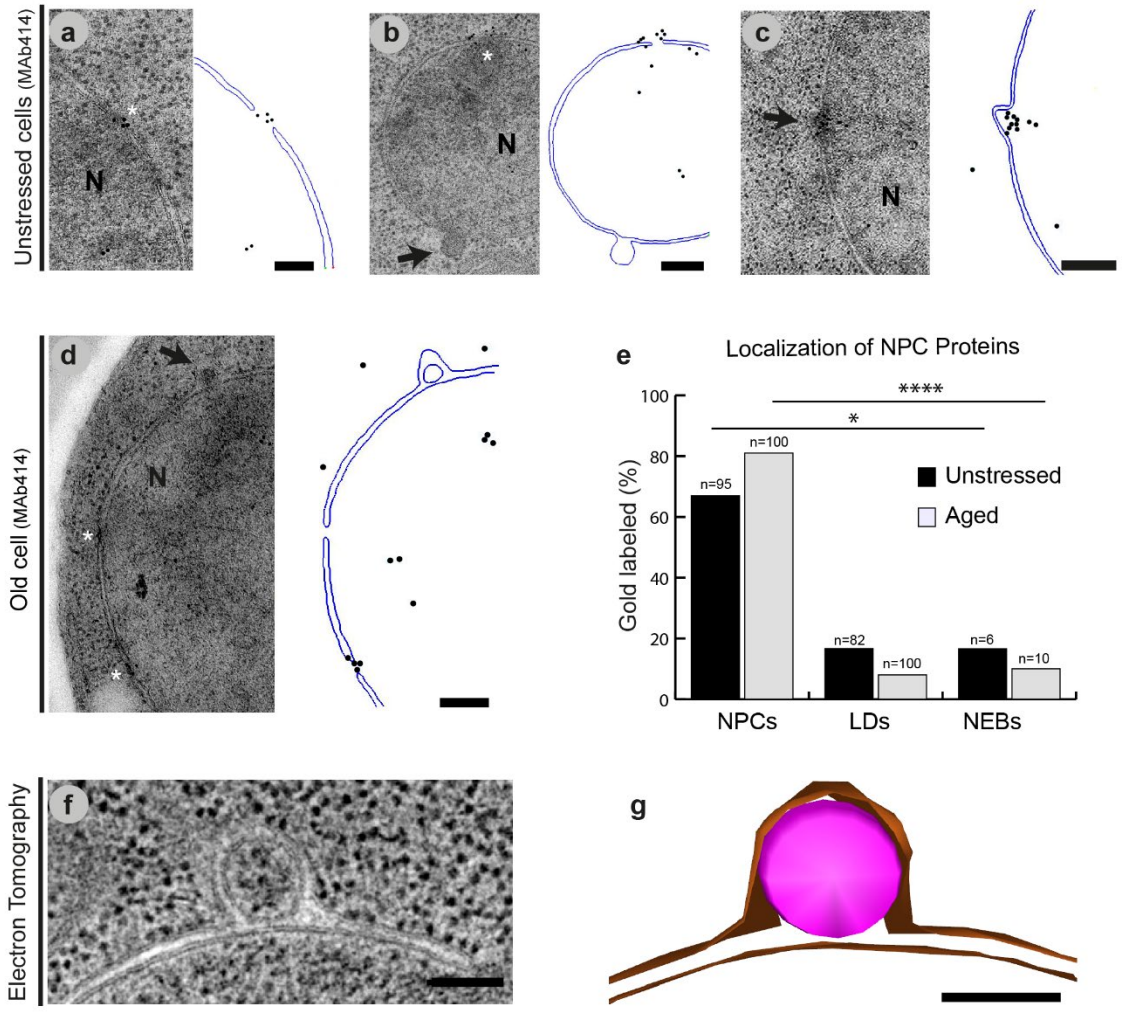

Figure 2.6 Immuno-gold labeling of NPC proteins

Antibody Mab414 which recognizes 4 NPC components was used to label cell sections containing unstressed cells (A-C) and aged cells (D). Examples of raw micrographs are shown, with a cartoon interpretation beside them to aid in visualization. Labeling of NPCs, Lipid droplets, and NEB events was quantified (E). Electron tomography reveals vesicles within some NEB events are continuous, and do not contain a "neck" connecting them to the INM (F-G). Abbreviations: NPC, nuclear pore complex; LD, lipid droplet; N, nucleus; NEB, nuclear envelope budding.

In an effort to further support this distinction, a comparison of the detailed morphology of NEB events with the previously reported herniations was accomplished through dual-axis electron tomography of the nuclear envelope in *S. cerevisiae* carried out by another member of our lab (Fig 2.6F-G). In some cases of the NEB events examined, the vesicle contained between the membranes was complete and not attached to either nuclear membrane by a 'neck', a different morphology than is seen by malfunctioning NPCs. In other cases, the membranes of the vesicle within the NEB event could not be distinguished, but no neck-like structure was evident either.

In conclusion, both the immuno-EM results and the 3D morphology of NEB events, suggest that failed NPC assembly and NEB are two separate processes, however, a small fraction of the protrusions quantified as NEB events in our data may still be NPC related structures, which can take on a similar morphology.

Collectively, our data shows a link between protein misfolding due to cellular stress and NEB. Although we have been unsuccessful as of yet in identifying specific cargoes of NEB events, this work represents a step forward in the understanding of these mysterious structures and has opened up several possible avenues to further investigate NEB function. Further work by our lab into this topic will investigate possible involvement of ESCRT proteins in the remodeling of membranes during NEB, possible links to the relationship between NEB and both autophagy and the ubiquitin-proteasome systems, as well as other candidate cargoes such as misfolded inner nuclear membrane proteins.

In the next chapter, we will leave NEB behind, and instead investigate the structure of the eukaryotic flagellum.

Chapter 3: The eukaryotic flagella tip varies throughout evolution

3.0 Introduction to flagella structure and function

Eukaryotic flagella (also known as cilia) are long cellular appendages found throughout the eukaryotes, as well as in diverse cell types throughout the human body. These organelles can both serve sensory functions like an antenna (74–77), or act as a large molecular motor either propelling the cell forward such as in human sperm (78–80), or creating a flow of fluid above a layer of cells as in the lungs (81). As defects in human flagella can lead to a wide range of diseases collectively referred to as ciliopathies, understanding the flagellum is of direct medical relevance (82–85).

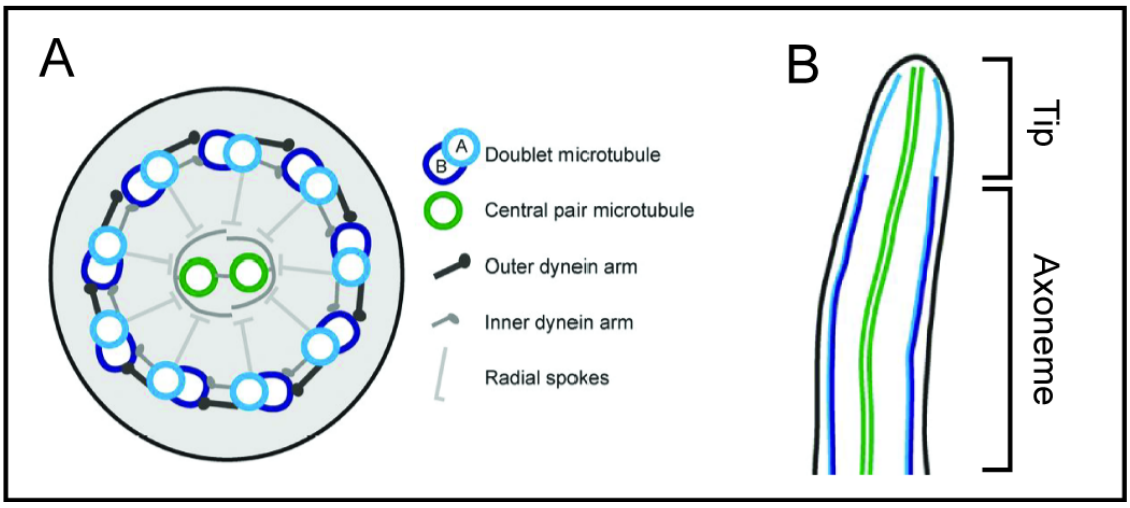

Figure 3.0.1 Motile flagella ultrastructure

(A) Cross section of the axoneme detailing the central pair complex, radial spokes, and 9 sets of doublet microtubules connected by inner and outer dynein arms. (B) Side view of a flagella. The axoneme comprises most of the structure, while the singlet region found at the flagella tip is much shorter.

Inside the motile flagellum is a symmetrical arrangement of microtubules referred to as the axoneme, in which the basic structure is generally conserved throughout evolution (Fig 3.0.1A) (86,87). The axoneme is a complex molecular machine arranged around two singlet microtubules called the central pair. The central pair and associated proteins, called the central pair complex, are attached to 9 doublet microtubules arranged in a ring by the radial spokes (88). Doublet microtubules are composed of an incomplete 10-protofilament B-tubule connected to an A-tubule containing 13 protofilaments (88). Neighboring doublets are attached to each other by dynein, the motor protein responsible for creating the flagellar beat by sliding neighboring

doublets past each other (89). All of these components work together to create and coordinate motion, and remarkably this molecular machine can coordinate several different motions of the flagella (90).

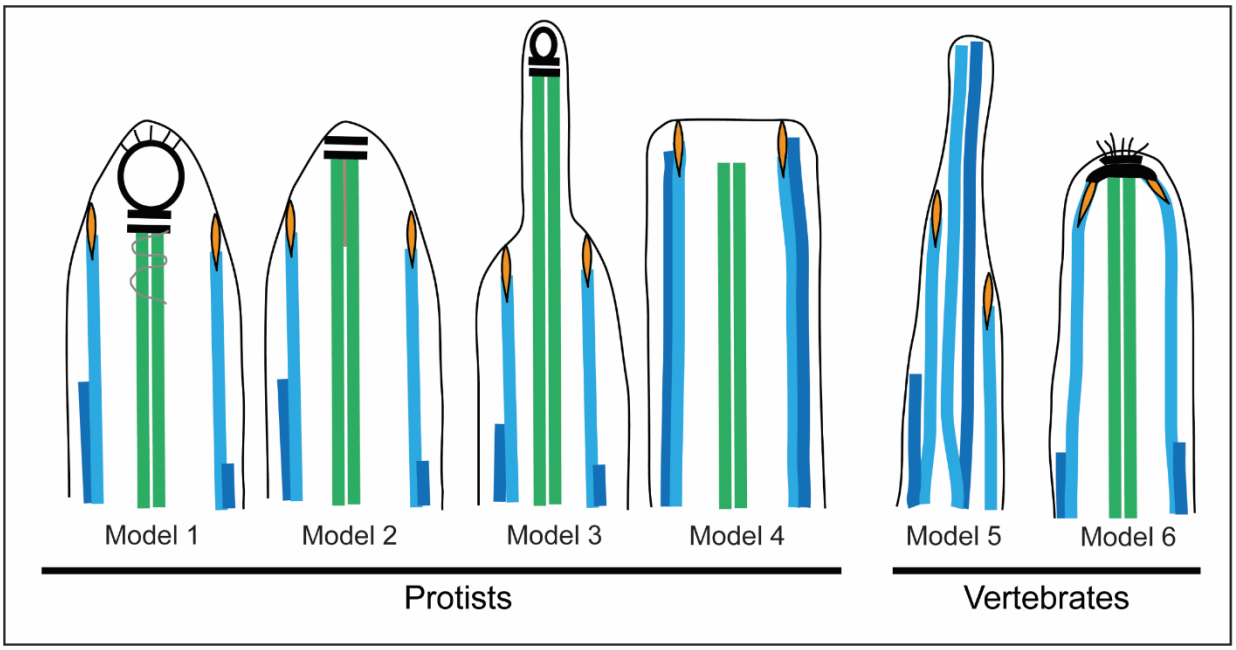

Figure 3.0.2 The distal tip of flagella throughout evolution

The distal tip of flagella takes on a variety of structures throughout evolution, featuring different arrangements of microtubules as well as different capping structures. Doublet microtubules and singlets originating from doublet microtubules are shown in blue (A tubule in light blue and B-tubule in darker blue), central pair microtubules in green, capping structures called the "carrot" in orange, and other capping structures in black and grey. Organisms exhibiting each structure are listed as follows: Model 1 (91)*, C. reinhardtii; Model 2* (56,92–95)*, C. reinhardtii, A. irridans; Model 3* (96–99)*, T. thermophila, S. caeca, S. similis; Model 4* (100,101)*, T. brucei, L. major, C. deanei, H. megaseliae; Model 5* (27,103, Paper III)*, B. Taurus, M. auratus, R. norvegicus, H. sapiens, M. musculus; Model 6* (103–105)*, B. taurus, B. cucumis, O. cuniculus, G. gallus, E. complanatis. Note, some organisms are listed twice due to interpretations in different publications, possibly resulting from differing sample preparation techniques.*

The length of the axoneme can be between 10-50 μm, depending both on the species and type of cell it belongs to (Fig 3.0.1B). The axoneme ends near the distal end of the flagellum, where it is often generalized that the B-tubules terminate along with other axonemal components, and the A-tubules and the central pair extend into a region called singlet zone which extends all the way to the flagellar tip. The tip region however, can take on a variety of structures in different organisms (Fig 3.0.2) (56,94,95,98,103, Paper II, Paper III). This is reviewed in **Paper II,** which was the first comprehensive review article about the flagellum tip.

Compared to common model organisms such as *C. reinhardtii* and *T. brucei*, relatively little is known about the structure of human flagella, especially the structure and function of its distal tip. Nevertheless, the tip of the flagellum is an important site for regulation of flagellar length, intraflagellar transport, as well as signaling (Paper II). Much less is known about the flagellar tip than the rest of the flagellum. Therefore, our lab set out to investigate the structure of the flagellar tip in humans as well as in a variety of organisms across evolution.

3.1 Structure of the human flagellar tip

Motile flagella are found in many tissues in the human body, however our model of choice was the human spermatozoa. The small size of the spermatozoan's cell body is perfectly suited to cryo-preparation by plunge freezing, and has the added benefit that it allows the study of human cells without requiring tissue collection or cell culture. While flagella from these sources have been used for cryo-EM (85), they must be isolated from the cell prior to plunge-freezing which may alter their structure. In contrast, flagella from human sperm cells are intact and functional, propelling the cells around the EM grid right up to the moment they are immobilized in a layer of vitreous ice.

The tail of the mammalian spermatozoan contains additional components besides the flagellar axoneme, and these structures divide the flagellum into 3 pieces (Fig. 3.1.1) (107). Starting at the distal tip, the endpiece contains the plasma membrane and the singlet region which then transits into a proper axoneme more proximally to the cell (27,83,103). The longest segment of the sperm tail, called the principal piece, contains additional structures called outer dense fibers which are thought to protect the flagellum (108), stabilize the axoneme (109) and modulate the flagellar beat (110,111). The outer dense fibers and axoneme are also surrounded by a mesh-like structure called the fibrous sheath in the principal piece (107,112). The most proximal region, called the mid-piece, is characterized by a mitochondrion that wraps around the axoneme and outer dense fibers, providing energy in the form of ATP to the flagella (107).

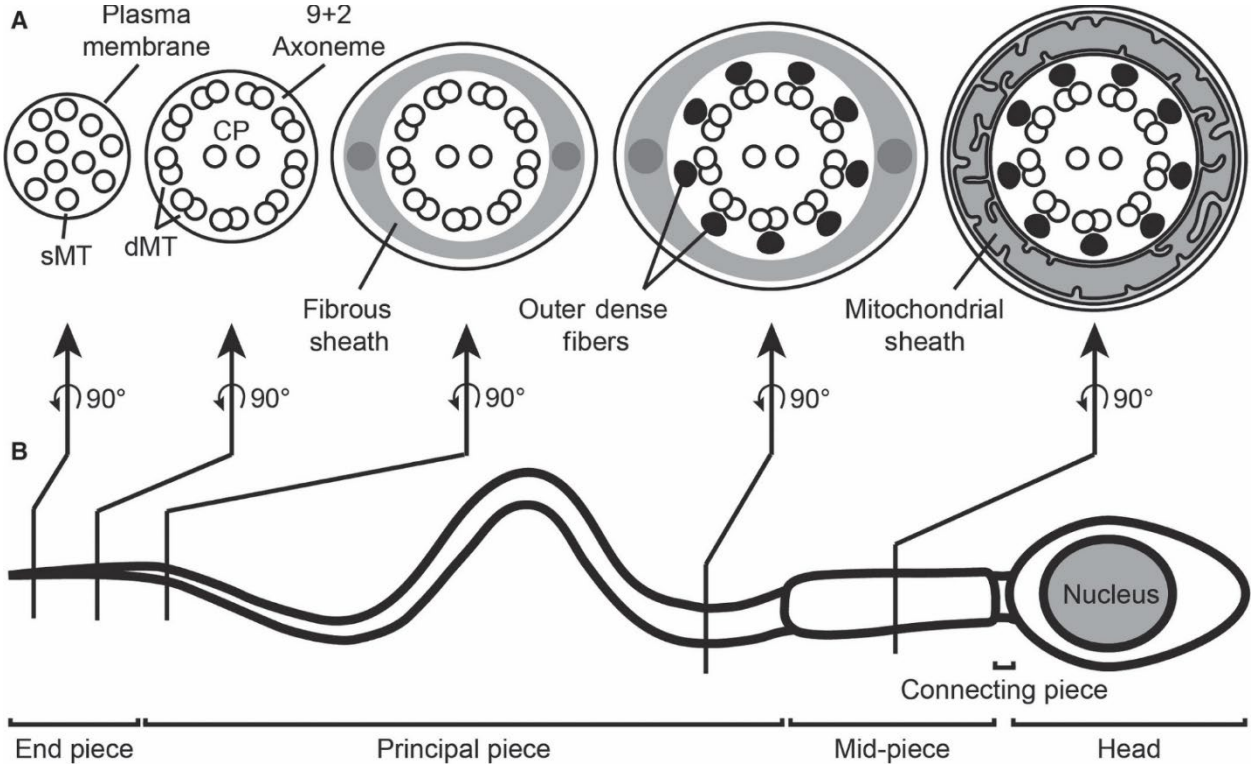

Figure 3.1.1 Ultrastructure of mammalian spermatozoa

An overview of the mammalian spermatozoon, with the location of cross sections (A) along the tail shown in (B). Starting with the connection to the cell body, the midpiece of the tail contains the flagellar axoneme, outer dense fibers, and a mitochondrial sheath. In the midpiece, the mitochondrial sheath is replaced by the fibrous sheath, and outer dense fibers end more distally. In the endpiece, only the axoneme and cell membrane remain until finally axonemal doublet microtubules terminate forming the singlet region.

Up to 18 singlet MTs have been observed in the singlet region of human flagella (27,83,111). Since a maximum of 11 microtubules would be expected if only the A-tubules of doublets and the central pair extended into the singlet region, this raises the question of where these additional microtubules originate from. Our hypothesis was therefore that the B-tubule can extend as a singlet microtubule in human sperm tails. To test this hypothesis, we examined the structure of the flagellar tips and the singlet region in human spermatozoa using cryo-ET.

When investigating the human singlet region a novel helical structure was surprisingly found inside the microtubules that we named TAILS (27). Many microtubule-associated proteins (called MAPs) that bind on the outside of the microtubule have been well characterized, however the subgroup of MAPs called MIPs (microtubule inner proteins) which bind inside the microtubule lumen have not received as much attention until recently and have mostly been studied in axonemal doublet microtubules (113,114). Not until recently were the identities of many of these proteins discovered (115–118). Before the discovery of TAILS, MIPs in the

singlet region had not been observed and it is the only known MIP complex exhibiting such an extensive helical arrangement, this complex will be discussed in further detail in chapter 4.

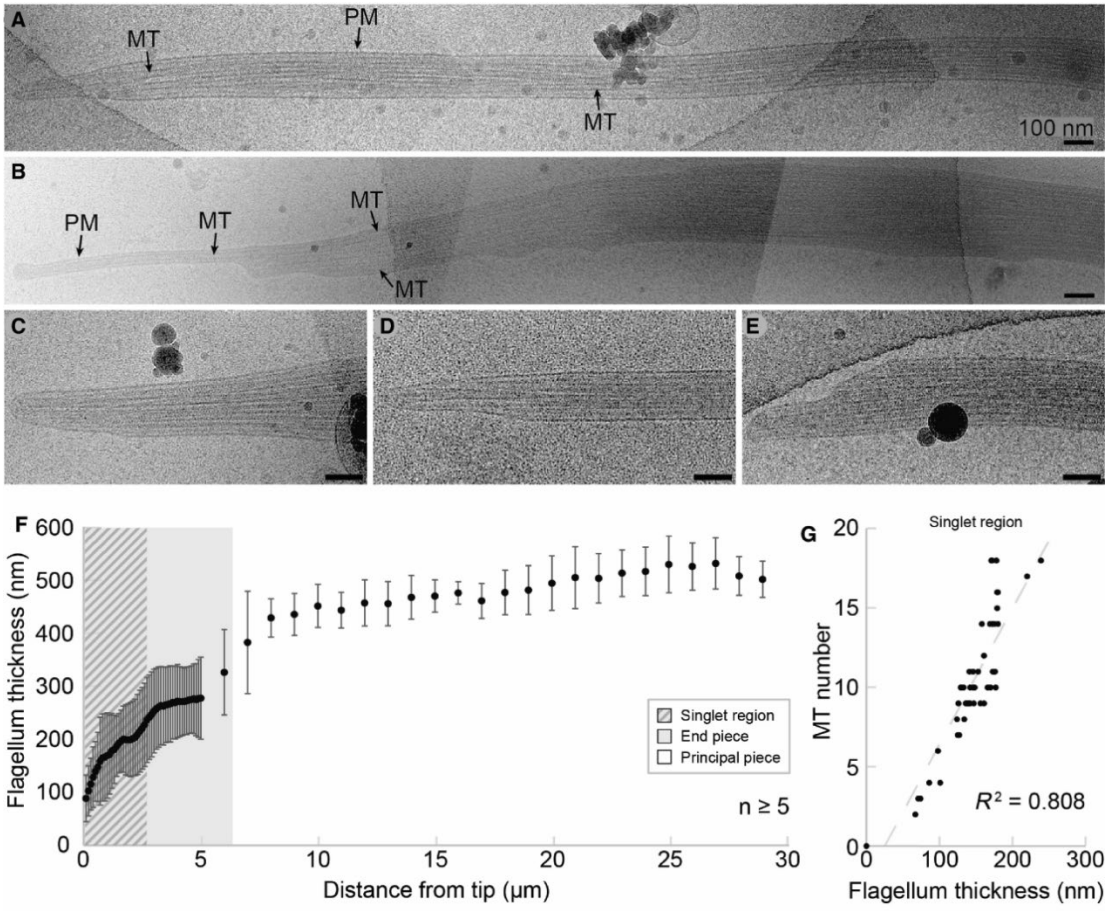

Figure 3.1.2 Electron tomography reveals variable morphology of human sperm flagella tip

Electron tomography reveals the morphology of the human sperm distal tip. (A-E) Variable morphologies were observed in flagella from different cells revealing more gradual (A, C, D) or more stepwise (B, E) decreases in thickness. (F) Thickness of the tip region was measured and plotted relative to distance from the tip. (G) Thickness in the singlet region was correlated with microtubule number. In some cases, more than 11 singlet MTs were observed.

We used cryo-ET to investigate the morphology of the endpiece of human spermatozoa, and these findings are presented in **Paper III**. In cryo-EM images of human spermatozoa, the morphology of the endpiece varied between cells (Fig 3.1.2). Some endpieces had constant thickness before gradually tapering at the end (Fig 3.1.2A), another sperm tip tapered in a in a fashion resembling a staircase, until only 1 singlet MT surrounded by membrane extended for close to 1 um (Fig 3.1.2B). Other intermediate morphologies were seen (Fig 3.1.2C-E) Individual sperm cells also showed large variability in flagellum thickness and number of singlet microtubules (Fig 3.1.2F-G). Flagellum thickness in the singlet region correlated with number of

microtubules it contained (Fig 3.1.2G). Since microtubules did not always terminate in similar patterns, thickness varied with respect to distance from tip in individual cells.

In order to gain more insight into the ultrastructure of the singlet region, the MT number was counted in 3 tomograms containing the flagellar tip, revealing diverse MT termination patterns. Most microtubule terminated between 300-400 nm from the tip, although some terminated as far as 1 um away. The MT number varied between the three tips, which contained 10, 11, and 14 singlet MTs. We hypothesized that the extra singlet microtubules in the tip containing 14 may have originated from the splitting of doublet microtubules at the transition into the singlet region.

To test this hypothesis, tomograms of human spermatozoa that were acquired between 1 and 3.5 μm away from the tip were examined. Three different modes of transition of doublets MTs into the singlet region were observed (Fig 3.1.3). As hypothesized, some doublet MTs split into two complete singlet MTs (n = 3; Fig 3.1.3A). In other MTs, the canonical mode of entry into the singlet region was observed in which the B-tubule simply terminated while the A-tubule extended (n = 2; Fig 3.1.3B). Finally, on one unique occasion, the A and B-tubules split apart but the B-tubule never formed a complete microtubule (Figs 3.1.3). Tomograms of two other cells also included the transition of the complete axoneme into the singlet region, however, they did not contain more than 11 sMTs. In these tomograms, all B-tubules terminated while the A-tubules extended to the tip, once again revealing a structural variability in the human sperm tip.

All MTs could be successfully used for subtomogram averaging, confirming that even the singlets formed from the B-tubule are complete 13 protofilament microtubules. Therefore, 3 new protofilaments were somehow initiated and the 13 protofilament architecture was assumed. While the TAILS complex was found in every MT with splitting microtubules, no obvious density was located at the splitting points. Possibly splitting is initiated by a transient complex or post-translational modification of tubulin. In the highly unusual sensory cilia of the nematode *C. elegans,* a similar phenomenon occurs in which doublet microtubules split to become two complete singlet microtubules that later combine to once again form a doublet microtubule in a process regulated by tubulin poly-glutamylation (119–121). However, very little is known about glutamylation patterns at the tip of human flagella. A possible function for TAILS could be stabilizing singlet microtubules after doublet splitting occurs, and imposing the 13-protofilament geometry. The (+)-end tracking protein EB1 is known to promote 13-protofilament formation *in vitro*, it is therefore another possible candidate to performing this function (122).

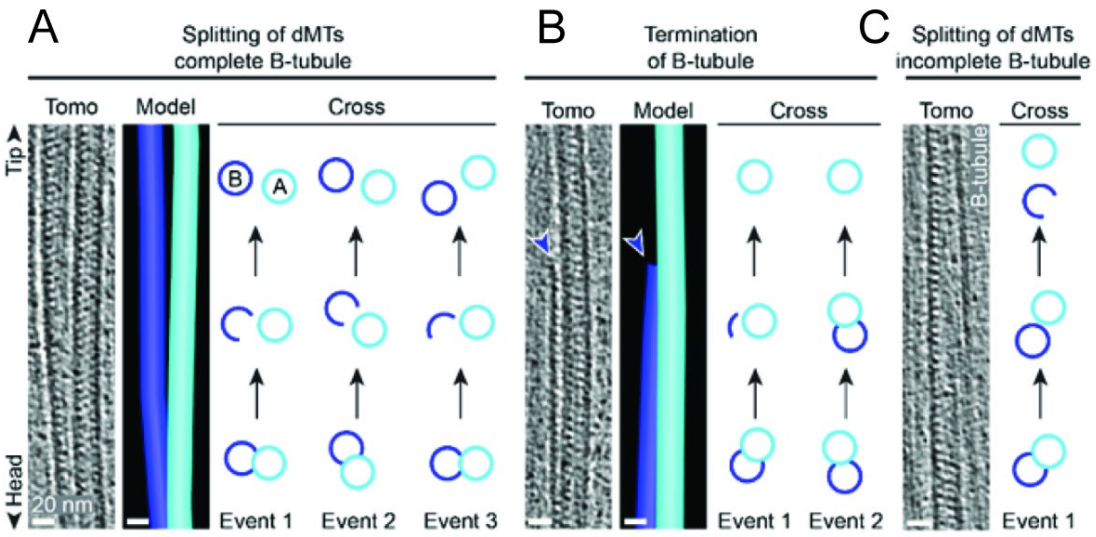

Fig 3.1.3 Doublets microtubules terminate in 3 ways in the tips of human sperm flagella

Tomograms of the transition region between the axoneme and singlet region reveal 3 modes of doublet termination. Models of each tomogram are drawn in blue to aid in visualization. (A) The B tubule splits apart, forming a complete 13 protofilament microtubule. (B) In other cases, the B-tubule simply terminates. (C) One event was seen in which the doublet MT split, but the B-tubule never formed a complete microtubule and instead extended as a C-shaped incomplete tubule.

3.2 Variability of the flagellum tip across evolution

While the basic structure of the axoneme is generally conserved throughout evolution, the structure of the flagellum tip can vary considerably (Figure 3.0.2) (56, Paper II). In both *Chlamydomonas reinhardtii* or *Tetrahymena thermophila*, the B-tubule of doublets terminate resulting in a singlet region containing only the A-tubules and central pair MTs (92,97,123). In contrast, organisms such as *Leishmania mexicana* and *Trypanosoma brucei* doublet MTs extend all the way to the tip and no singlet region exists (56,124). As highlighted in chapter 3.1, human flagellar tips have a distinct morphology in which doublets split into two complete singlet MTs, and rodents exhibit a similar morphology in which the singlet region is composed of pairs of singlets called "duplex-microtubules", which originate from the same doublet (124).

While single celled organisms such as *C. reinhardtii* have short generation times and lend themselves quite well to genetic manipulation, they are not a suitable model for probing the function of the human flagella tip, therefore we set out to characterize the flagellum tip of a variety of organisms in order to find a more applicable model. While human spermatozoa work well for studies of the wild type flagellum, and motility mutants can be isolated from dysfunctional sperm samples, they are not suitable for genetic manipulation. Therefore a genetically tractable model is desired.

First, we were curious about the extent of doublet-splitting throughout evolution. Therefore, we prepared sperm from 3 organisms by HPF/FS, and searched thin sections of these samples for cross sections of the tip region, which would contain microtubules not arranged with the distinct

"9 + 2" axonemal geometry (Fig 3.2, axoneme F-G). The species examined were bovine sperm (*Bos taurus*), and sperm from the sea urchins *Strongylocentrotus purpuratus* (purple urchin) and *Strongylocentrotus droebachiensis* (green urchin).

The only species in which cross sections containing more than 11 microtubules were found was *Bos taurus* (Fig 3.2 A-D). Cross sections of the singlet region containing anywhere between 6 and 18 MTs were found, so we hypothesized that doublet splitting occurs in bovine flagella tips as well. This was later confirmed in cryo-electron micrographs (Fig 3.2 E) and tomograms of bovine sperm. Since doublet splitting or endpieces with greater than 11 singlet microtubules have now been described in human, bovine, and mouse, and hamster sperm, we expect this morphology to be generally conserved in mammalian sperm.

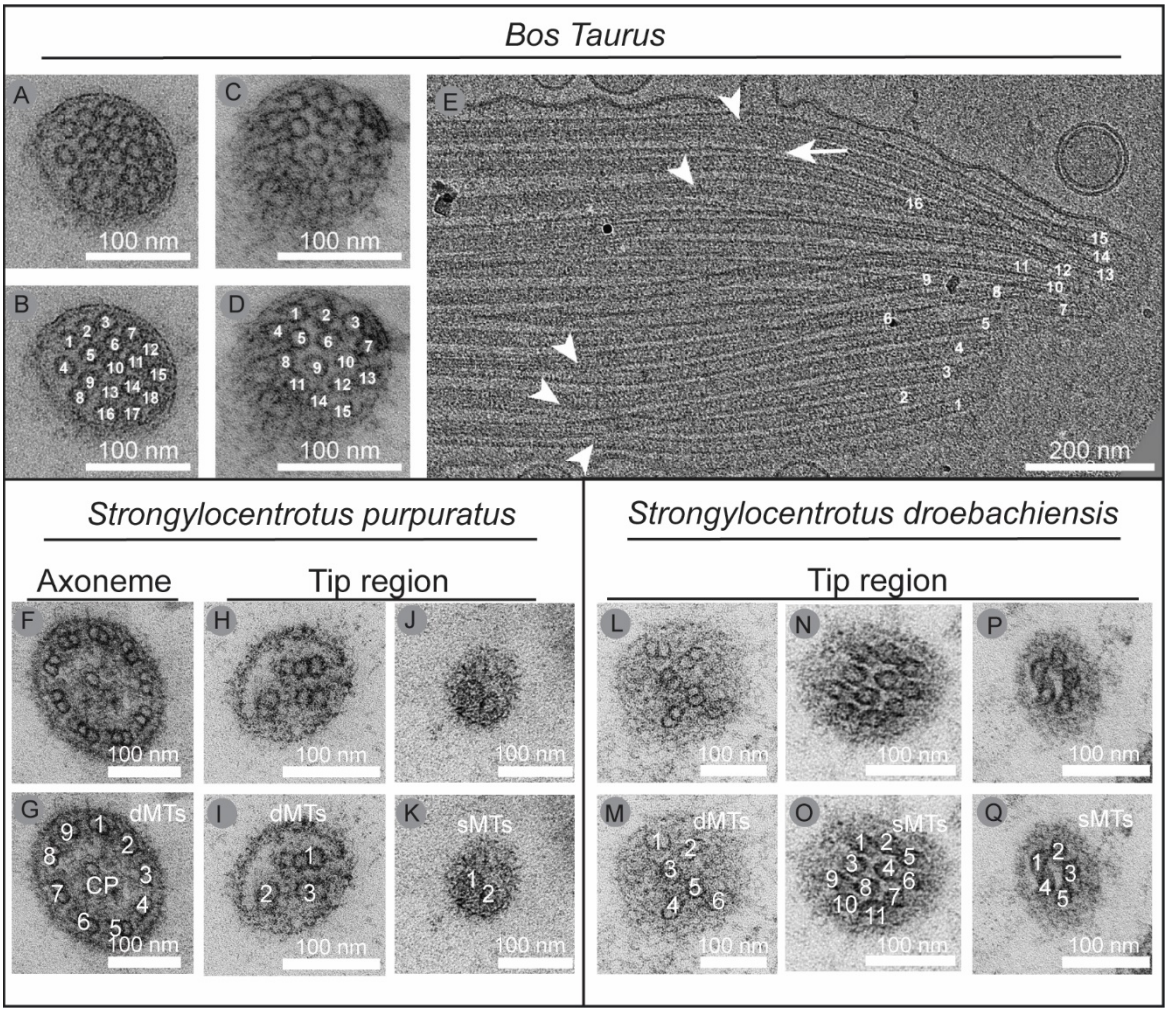

Fig 3.2 Flagellum tip morphology in bovine and sea urchin sperm

Thin sections through the singlet region of bovine sperm cells show at least 18 (A–B) and 15 (C–D) sMTs. Panels A–B and C–D, respectively, show the same images, but sMTs are counted in panels B and D. (E) Cryo-EM of a flattened bovine sperm flagellum tip. Five events of dMTs splitting into two sMTs are shown (arrowheads) and at least 16 sMT ends are visible (numbered). One event of B-tubule termination is shown by the white arrow. Thin sections of the

axoneme (F-G) and tip region (H-K) of Strongylocentrotus purpuratus sperm, and of the tip region of Strongylocentrotus droebachiensis sperm (L-Q). Pairs of panels (F-G), (H-I), (J-K), (L-M), (N-O), (P-Q) show the same micrographs but the bottom panel is annotated to count MTs. Panels containing doublet MTs are labeled dMTs, singlets are labeled sMTs, and the central pair is labeled CP. Scale bars are all 100 nm in panels except in panel E, which is 200 nm.

In contrast, no cases were found in the tips of sea urchin sperm in which greater than 11 singlet MTs were present. In both species of sea urchin, tips containing between 2 and 6 doublets were found (Fig 3.2 H-I, L-M), or between two 2 and 11 singlet microtubules (Fig 3.2 J-K, N-Q). The doublet MTs in these tips were no longer arranged symmetrically like axonemal doublets (Fig 3.2 F-G), and the central pair MTs appear to have terminated. However, the tip containing 11 singlet MTs could have stemmed from termination of the B-tubule of all 9 doublet MTs and the central pair MTs. This would suggest a variability in sea urchin sperm tips in which some flagella end in long disordered doublet regions lacking the central pair and others contain a singlet region similar to the architecture seen in *C. reinhardtii.* However, since we didn't follow these tips in serial sections, it is impossible to say whether the 11 singlets stemmed from each of the doublets and the central pair, or if this was preceded by a region of disordered doublets in which some split, while the B-tubules of others terminated. Either way, the distal tip of sea urchin flagella is morphologically distinct from mammalian flagella, where regions containing only a few disordered doublets were never observed. Therefore, possibly mouse sperm would be the best model for human sperm flagella since genetic manipulation of mice is well-established.

3.3 Evolutionary conservation of TAILS

Cryo-tomograms of the flagella tip of spermatozoa from a range of species were acquired to investigate the conservation of TAILS throughout evolution. A decoration similar to TAILS was visible in the lumen of microtubules in the bovine singlet region, so we performed subtomogram averaging to compare the structures. A total of 115 microtubules from 10 cryo-electron tomograms were modelled, resulting in 14753 sub-tomogram volumes were extracted for sub-tomogram averaging. The resulting average had the same structure as our average from human sperm, but at increased resolution (Fig 3.3A-D). TAILS was present as a complete decoration of the internal microtubule wall with a periodicity of 8 nm, consisting of helical segments that follow the tubulin lattice. The improved resolution also revealed that TAILS consists of a head that is localized centrally between two tubulin subunits where it forms interactions with both of them (Fig 3.3A-B). Another novel feature was a thin bridge that appeared to connect two consecutive TAILS segments over the gap (Fig 3.3B, red arrow), coinciding with a small density appearing every 4 nm near the gap in TAILS. The outside of the microtubule appeared completely void of microtubule binding proteins.

We progressed to examining the presence of TAILS in sperm endpieces on intact spermatozoa from chicken (*Gallus gallus domesticus*), the western clawed frog (*Xenopus tropicalis*) and the protist *Trypanosoma brucei* using cryo-ET. TAILS was present in all the animal sperm tails investigated, but not in the protist *T. brucei* (Fig 3.3E). From a previous publication it is also

apparent to be lacking in the microtubules at the tip of the green algae *C. reinhardtii* flagellum tip (125).

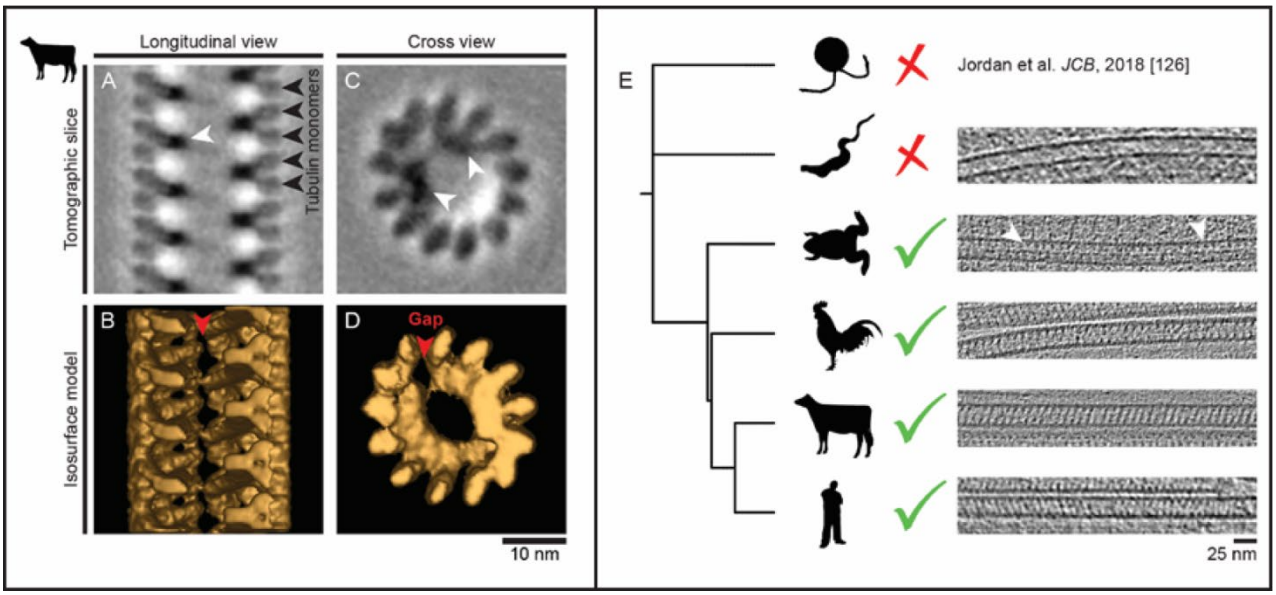

Fig 3.3.2 Conservation of TAILS across evolution

Subtomogram averaging reveals the structure of TAILS in the bovine flagellum tip. Panels A and C contain the raw data, B and D depict an isosurface model of the structure. Tubulin monomers are marked with black arrows, TAILS which repeats every 8 nm is marked with a white arrow. The red arrow in (B) points out the bridge that connects segments of TAILS, and the gap in the structure in (D). Panel E contains a phylogenetic tree displaying the conservation of TAILS across evolution, with sections of tomograms of microtubules from the flagellum tip of each organism to the right. White arrows point out TAILS in Xenopus microtubules.

The tomograms of bovine flagella revealed a similar tip morphology to human sperm, in which doublets split into two complete singlet microtubules containing TAILS (Fig 3.3.3A). In contrast, the tip of chicken sperm flagella did not contain a long singlet region, and was instead characterized by a disordered array of doublet microtubuless which sporadically terminate completely instead of forming singlets (B). This morphology was more similar to what was observed in some of the cross sections of sea urchin sperm (Chapter 3.2). In some cases, doublets terminated one by one until only a single doublet microtubule remained which extended all the way to the tip. In addition to the doublet microtubule, there appeared to be an additional density between the microtubule and the membrane. Furthermore, the doublets at the tip of chicken sperm contained TAILS, which was also observed in the doublets of human and bovine sperm in the transition to the singlet region (27). The discovery of TAILS in other organisms was helpful in narrowing down candidates for the proteins that form TAILS, which will be discussed further in the next chapter, and is presented in **Paper IV**.

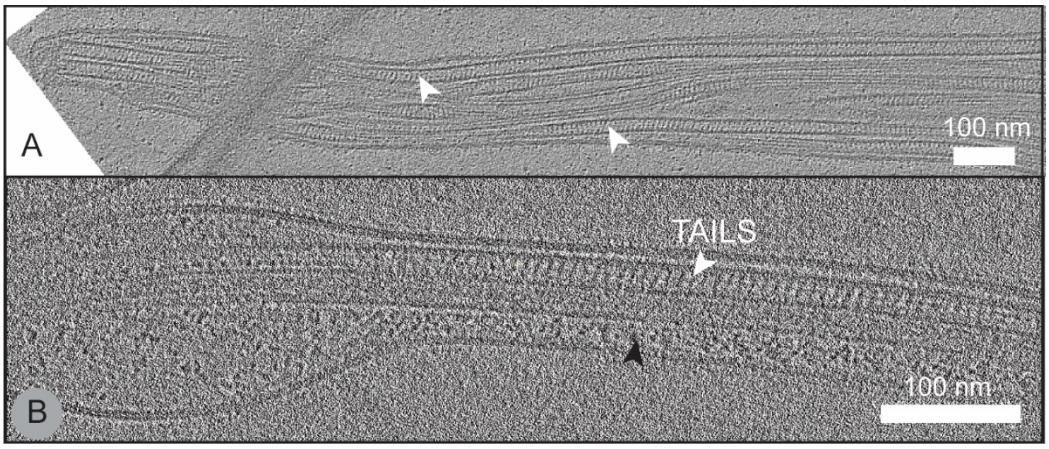

Figure 3.3.3 Flagellum tip architecture of Bos taurus and Gallus gallus

Cryo-electron tomography revealed different ultrastructures in the tip of bovine (Bos taurus) and chicken (Gallus gallus) sperm. The tips of bovine sperm flagella are characterized by a singlet region, in which TAILS decorates the lumen of singlet microtubules, indicated by white arrows (A). The tip of chicken sperm flagella contains long regions of disordered doublets decorated by TAILS (white arrow), which are sometimes decorated by a density on the outside of the microtubule as well indicated by the black arrow (B). Scale bars: 100 nm.

Chapter 4: High-resolution structure of TAILS

4.0 Introduction

Perhaps the most intriguing feature of the human flagella tip was the presence of TAILS, an extensive pseudo-helical structure decorating the lumen of singlet MTs (27). While we were able to visualize the 3D structure by subtomogram averaging, the protein(s) forming this structure remains a mystery. Therefore, we designed a multi-pronged approach to determine the identity of the protein(s) forming TAILS: involving proteomics, bioinformatics, and structural determination by SPA. This approach is described in **Paper IV**.

Proteomic studies of the human sperm tail show it to be composed of 700-1500 different proteins (126–130), many of which of unknown functions, localizations, or completely uncharacterized. Therefore, to narrow down this list of protein candidates that could be the TAILS structure, another member of the lab developed a protocol based on sonication of sperm cells and separation by density gradient to enrich a sample for flagellum tips, and obtain a tip proteome. Then, by scanning for the existence of TAILS throughout evolution (Chapter 3.3), we were able to narrow this list down further by comparative genomics.

The final portion of the strategy was to determine a high-resolution structure of TAILS. Several aspects of TAILS structure could not be determined in the original subtomogram average. For example; does TAILS bind between tubulin heterodimers or within heterodimers? How does TAILS affect the microtubule lattice? And finally, most pertinent to identifying TAILS; is TAILS composed of a single repeating protein segment, or is there variation within each repeat of TAILS at different points around the helix?

Furthermore, if sufficient resolution was achieved, we aimed to identify the protein components directly by essentially "reading" sequences of side chains (131). Or, at somewhat lower resolution, it would be possible to identify candidate protein folds by using molecular replacement software to fit a library of known structures into our unknown density, then compare this information to the list of candidates generated by proteomics (132). Both of these strategies have been used by others to identify proteins in cryo-EM structures, and shortly after we began our efforts another group identified over 30 unknown MIPs in the structure of purified axonemal doublet microtubules, demonstrating the potential effectiveness of the strategy (115). Our method of choice for high-resolution structural determination was SPA. Although the effectiveness of this approach was limited by difficulties in sample preparation (discussed in Chapter 4.1), we were still able to determine the structure at an overall resolution of 5-6 Å and gain valuable insights to its composition and function.

4.1 Preparation of TAILS-containing singlets for single particle analysis

SPA is usually applied to purified proteins, of which the identity is known, which can be biochemically purified at sufficient quantities and plunge frozen on EM grids free of contaminants. Then, images can automatically be collected, resulting in large quantities of

particles for averaging. Since the identity of TAILS is unknown, and we cannot purify it and co-polymerize it with MTs, somehow singlet MTs must be isolated in order to determine their structure by EM. Although axonemal doublet microtubules can readily be isolated for SPA (115), the singlet MTs make up a very small fraction of flagellar microtubules and exhibit lower stability, making their isolation more difficult. Therefore, the strategy adopted was to perturb the flagellar membrane such that bare microtubules at the tip extend from the cell and can be imaged without cellular material above and below them. In this way, whole sperm cells which have been partially demembranated are applied to EM grids and images are acquired at manually chosen positions near the tip of the flagella.

A variety of combinations of buffers and detergents were tested to partially demembranate cells without causing depolymerization of singlet microtubules, and EM grids were prepared negative stain was used to assess each condition (Fig 4.1A). Each preparation was assessed for several characteristics:

(1) Successful removal of membrane at the flagellar tip.

(2) Length of singlet microtubules extending from the tip.

(3) "Splaying" of the microtubules, meaning lack of microtubule clumping, as microtubules laying on top of each other cannot be used for SPA.

The optimal preparation conditions were determined to be as follows: Purified sperm cells were incubated for 20 minutes in HBSS buffer (Hank's balanced salt solution) containing 0.25% Triton X-100 (by volume) for demembranation, an additional 50 mM KCl to reduce microtubule clumping, and 1 mM PMSF to inhibit cellular proteases. The microtubule stabilizing drug taxol was used in initial preparations, however it was later determined to be unnecessary and SPA datasets were collected without addition of taxol.

Once suitable conditions had been identified in negatively stained samples, cells were prepared in the same way but plunge frozen and imaged by cryo-EM. Several datasets were collected, and in images taken at a greater defocus TAILS could be seen decorating the microtubule lumen (Fig 4.1B). Furthermore, layer lines corresponding to a 40 Å repeat and an 80 Å repeat could clearly be visualized in 2D Fourier transforms generated from images of individual microtubules, confirming the presence of a consistent decoration every 80 Å corresponding to TAILS. Alpha and beta tubulin are not distinguished in the FFT, and appear as the 40 Å layer line.

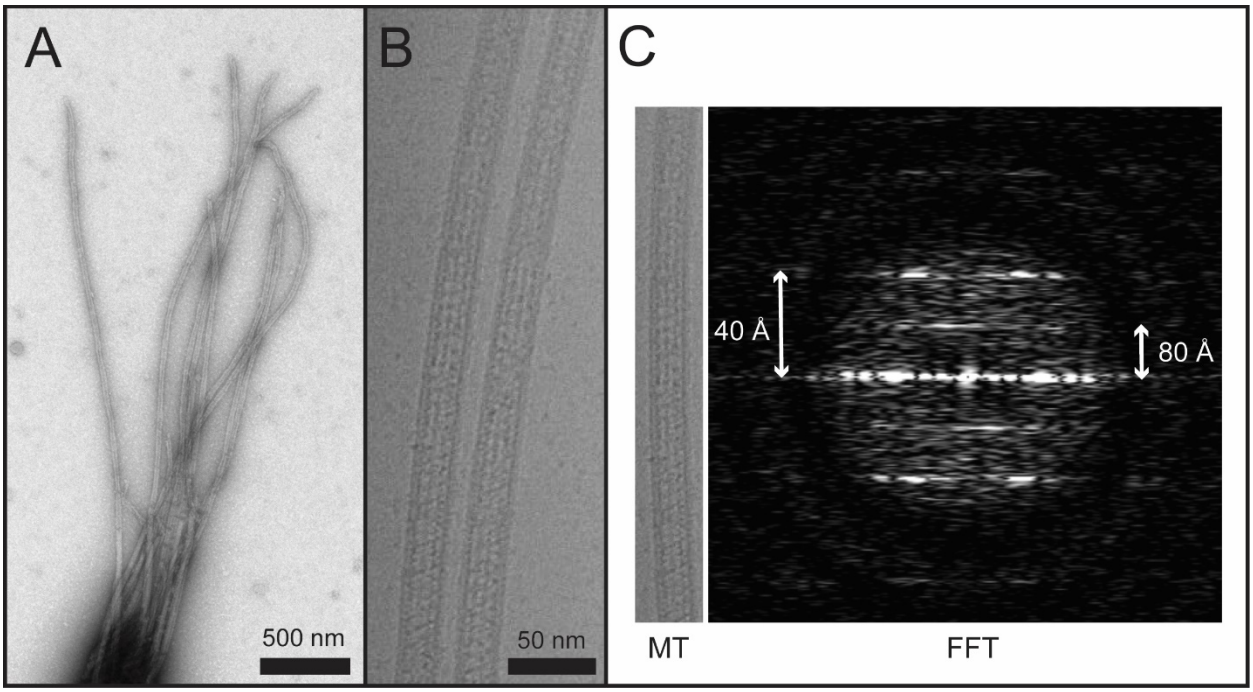

Figure 4.1 Preparation of TAILS-containing microtubules for single particle analysis

Singlet microtubules containing TAILS were prepared for SPA by applying demembranated spermatozoa to EM grids and imaging near the tip. (A) Negative stain micrograph of a "splayed" flagella tip, in which singlet MTs are exposed. (B) Cryo-electron micrograph of two singlet MTs emanating from the tip of a demembranated flagella, prepared by the same method as the flagella in Panel A, but plunge frozen. A faint repeat every 8 nm can be seen within the MT, indicating the presence of TAILS. (C) 2D Fourier transform of one of the microtubules in panel B, with layer line spacing indicated. Presence of the 80 Å layer line confirms presence of TAILS within the microtubule.

4.2 Overview of data processing strategy

Microtubule structural determination is complicated by the presence of the seam, a feature of 13-protofilament microtubules that breaks the otherwise helical symmetry of the filament (133). At the seam, alpha and beta-tubulin monomers form lateral contacts in contrast to the rest of the microtubule in which alpha-subunits contact alpha-subunits, and beta contacts beta (Fig 4.2.2 A). Several software packages have been developed to perform helical refinement which can be used to robustly determine the structure of helical filaments given a rough approximation of the correct helical parameters, and apply this helical symmetry to the final reconstruction to improve resolution (35).

However, since 13-protofilament microtubules are only pseudo-helical in nature, helical symmetry cannot be applied and care must be taken in order to correctly align the microtubule seam. Human alpha and beta-tubulin share approximately 40% sequence identity and fold with the same tertiary structure, differing only slightly in secondary structure at a few locations (134). Therefore, in individual particles images with low signal-to-noise ratio, the locations of alpha

and beta tubulin are difficult to decipher and become averaged together in automatic refinements. Consequently, data processing strategies specifically designed for microtubules have been developed (33,34), which rely on the relationships between particles belonging to the same microtubule. Initial classification steps are performed using "super-particles" or "segment averages", in which a few neighboring particles in the same microtubule are combined to increase contrast. Since the seam location should be consistent within each microtubule, the shifts and rotations of neighboring particles within a microtubule are related. After initial alignments for each particle are obtained, the seam location can be deduced by linear regression analysis of particles belonging to the same microtubule because particles will be biased towards the true seam location. Then, the rotations of each particle along a microtubule can be unified to be consistent with each other. The X/Y shifts of neighboring particles can be made consistent in a similar way. Next, the seam location can then be validated, and then adjusted if necessary, by 3D classification without alignment to 26 reference maps representing all thirteen possible rotations, and both possible 4 nm shifts. Addition of microtubule-binding proteins, such as EB3 (34), the CKK-domains of CAMSAP1 (33), or kinesin (135) can be helpful in alignment of particles. These proteins bind microtubules with a periodicity of 8 nm, allowing the tubulin register to be aligned, and do not bind the seam therefore assisting in seam alignment. Although microtubule-binding proteins are generally used, seam location has be correctly deduced by these methods in undecorated microtubules as well providing insights on the structural effects of microtubule-binding proteins (34). This study revealed the effects of GTP hydrolysis in the absence of microtubule binding proteins, demonstrating compaction of the microtubule lattice and a slight opening occurs at the seam after GTP hydrolysis.

The data processing strategy we used was as follows: Movies containing microtubules were motion corrected in Relion (32), and CTF correction was also performed in Relion using ctffind4 (136). Filaments were picked manually in Relion, and particles were extracted every 82 Å along filaments, corresponding to the length of one tubulin heterodimer (Fig 4.2.1A). Particles were binned to a pixel size of 1.06 Å / pixel during extraction (movies were collected in super-resolution mode with pixel size of 0.53 Å / pixel) and combined into a single stack for import into cisTEM (36), which was used for all the remaining steps. 2D classification was performed to filter out "junk" particles (Fig 4.2.1B), and multi-reference refinement was used to separate doublet and singlet microtubule particles (Fig 4.2.1C). Initial references for multireference refinement were low-pass filtered versions structures of an undecorated 13-protofilament singlet microtubule, and an empty doublet microtubule. The class containing singlet particles was refined using cisTEM's autorefine, using an empty microtubule as a reference. Particles were then subjected to 3D classification with 3 classes again. The remainder of the processing was performed using particles from one of the classes, which corresponded to a TAILS-containing microtubule (~90% out of the 45,538 singlet particles). Resolution was improved with subsequent rounds of manual refinement to generate an overall structure of TAILS (Fig 4.2.1D), and then individual densities were refined using masked refinement of individual pairs of protofilaments, and B-factor sharpening was applied (Fig 4.2.1E). The structure was used to assess TAILS candidate proteins (Fig 4.2.1F), discussed further in Chapter 4.4.2.

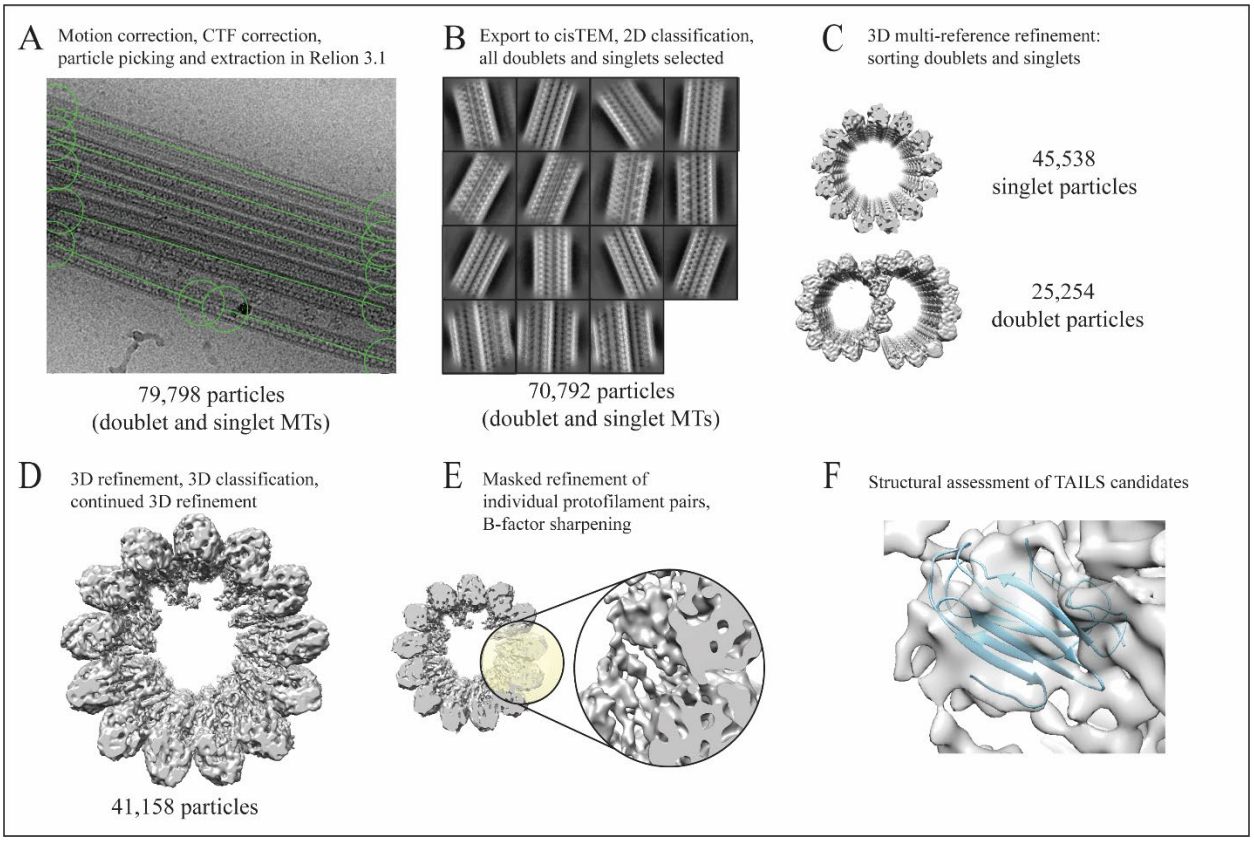

Figure 4.2.2 Single particle data processing strategy

3D reconstruction of TAILS-bound microtubules by SPA was performed using Relion (32) *and cisTEM* (36). *(A) Motion correction, CTF correction, particle picking (displayed in panel A), and extraction were performed in Relion. Remaining steps were performed in cisTEM. (B) 2D class averages of singlet and doublet microtubules were generated. (C) Singlet and doublet microtubules were separated by multi-reference refinement. References used are displayed. (D) 3D refinement resulted in the overall structure of the TAILS-bound singlet shown. (E) Masked refinement of pairs of protofilaments were used to improve local resolution of individual regions of the structure. An example of a cylindrical mask over protofilaments 4 and 5 is shown, with the result enlarged. (F) TAILS candidates were assessed by fitting homology models into the SPA structure.*

In our reconstruction of TAILS-bound microtubules, the strong signal of TAILS repeating every 8nm and the gap in TAILS combined with differences in its subunits were sufficient to correctly align the microtubule lattice, so we continued without the seam-finding techniques described above. Alpha and beta-tubulin can be differentiated in our structure based on the presence of a small alpha helix that occurs in residues 33-50 of beta-tubulin, but forms a disordered loop in alpha tubulin (Fig 4.2.2 B). In our reconstruction, beta-tubulin fits this density quite well in one register along each protofilament (Fig 4.2.2 C), but the helix sticks out from the density if shifted 4nm to the other register (Fig 4.2.2 D). In this way, the correct alpha-beta register was

determined for each protofilament individually, confirming the previously proposed seam location (27). Although the microtubule specific data processing strategies explained above were not required to resolve the correct tubulin lattice, we plan on going back and implementing them on the data in hopes of improving the resolution achieved.

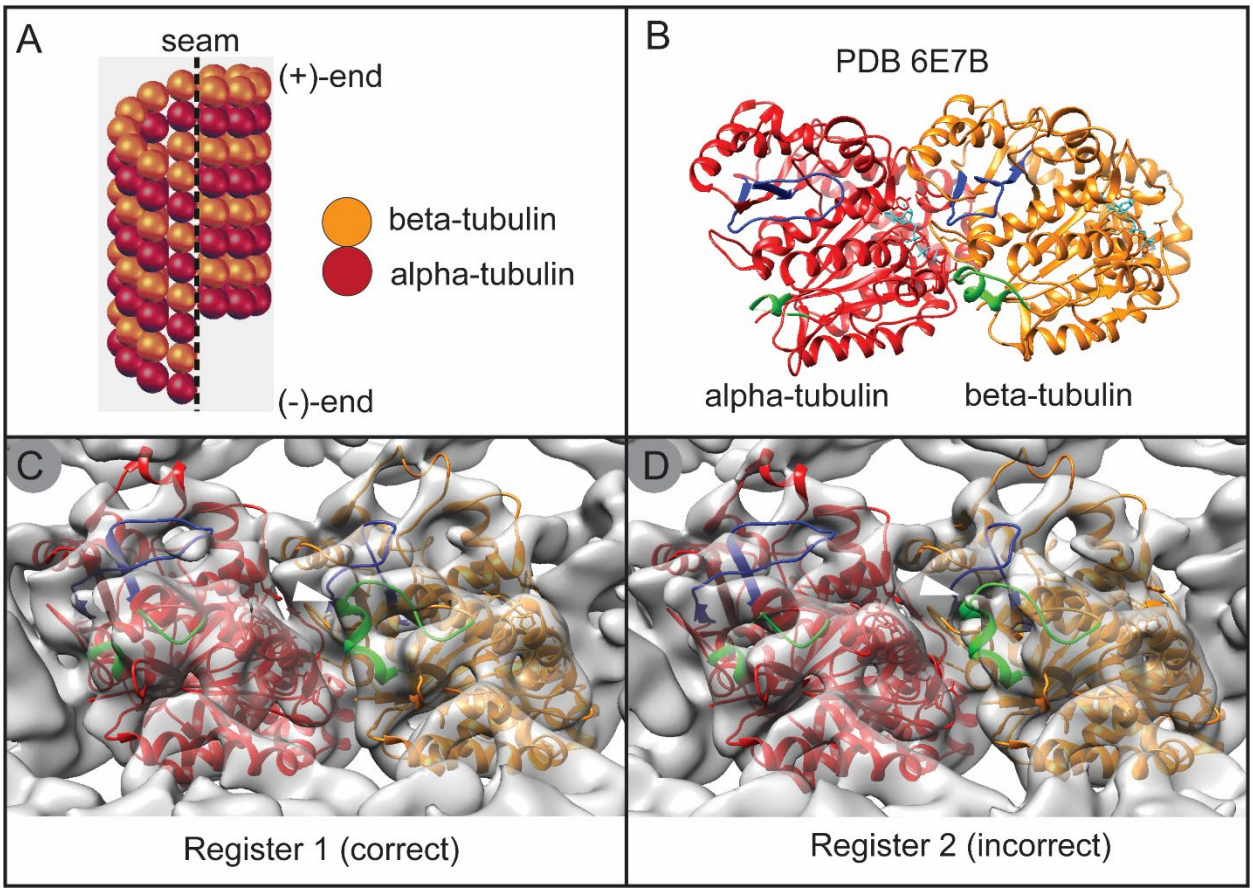

Figure 4.2.2 Determining of microtubule seam location

(A) The seam is a unique point in microtubule structure, breaking the helical arrangement of tubulin heterodimers. The seam is the only point in the microtubule at which alpha (red) and beta-tubulin (orange) contact each other laterally. The (+)-end of the microtubule is the end capped by beta-tubulin, and is where the microtubule exhibits dynamic instability. The (-)-end is the end capped by alpha-tubulin, and is found in the basal body of the flagella. (B) Alpha and beta-tubulin share considerable structural similarity. Two areas exhibiting differences are colored: The first is the S9/S10 loop, colored blue, which is longer in alpha-tubulin. The second is residues 36-50, colored green, which form an alpha-helix in beta-tubulin and a disordered loop in the alpha-subunit. Both subunits bind guanine nucleotides, colored cyan. Both subunits bind GTP, however this is hydrolyzed to form GDP in the beta subunit after microtubule formation. (C-D) Tubulin heterodimers were fit into each protofilament in two registers, two examples in protofilament 12 are displayed. Panel C contains the correct register, while panel D contains the incorrect register, as judged by the fit of residues 36-50 (colored green and marked by white arrowheads). Differences in the S9/S10 loop (blue) are not easily discernible.

By determining the correct tubulin register of each protofilament in this way, the seam was located at the gap in TAILS, shown in Fig 3.3.1.

4.3 High resolution structure of TAILS

4.3.0 SPA reveals TAILS secondary structure and microtubule binding location

Using data collected in this way, the structure of flagellar microtubules containing TAILS was solved to an overall resolution of about 6 Å, revealing secondary structure of its subunits for the first time (Fig 4.3.0A). Local resolution of some MIPs was then improved to between 4.5 and 6 Å by masked refinement of protofilament pairs (Fig 4.3.0A, zoom-in views).

Similar to what was observed in bull sperm, TAILS formed a C-shaped structure which follows the helical lattice, binding between alpha and beta tubulin of the same heterodimer (Fig 4.3.0B-C). Each MIP subunit forming the C-shaped structure was assigned a number (MIP1 – MIP11), based on the protofilament it binds to (Fig 4.3.0A, numbering indicated inside microtubule). Furthermore, each subunit is tilted with respect to the radius of the microtubule, such that it contacts the adjacent subunit. Thus, this suggests a mechanism by which TAILS could provide a stabilizing role, stabilizing lateral contacts between tubulin heterodimers and forming lateral interactions with the adjacent TAILS subunit. Since GDP hydrolysis in the microtubule results in weakening of lateral contacts between tubulin, but tightening of longitudinal contacts (137,138), this provides an obvious explanation for why TAILS is arranged laterally rather than longitudinally, consistent with a stabilizing role.

Fig 4.3.0 High-resolution structure of the TAILS-decorated microtubule (next page)

The high-resolution structure of the TAILS bound microtubule was determined using SPA on images of microtubules from demembranated flagella tips. (A) The overall structure is displayed in the center, with MIPs labeled on the inside and protofilaments labeled on the outside (pf1-13). 11 MIP folds decorate the inside of the microtubule (1-11), in addition to 2 "zipper" MIPs (z). The "bridge" interaction between MIP1 and Z2 is indicated by an asterisk. Improved structures of smaller regions of the microtubule are shown in the circular zoom-ins. The seam location is indicated with an arrow, between protofilaments 13 and 1. (B&C) Two different views of the C-shaped structure from inside the lumen. The structure binds within tubulin heterodimers, with a periodicity of 8 nm. Perspectives of each view are indicated by arrows in panel A. (D) View of the zipper MIPs (Z1 and Z2) from inside the microtubule lumen. The bridge interaction is indicated by an asterisk.

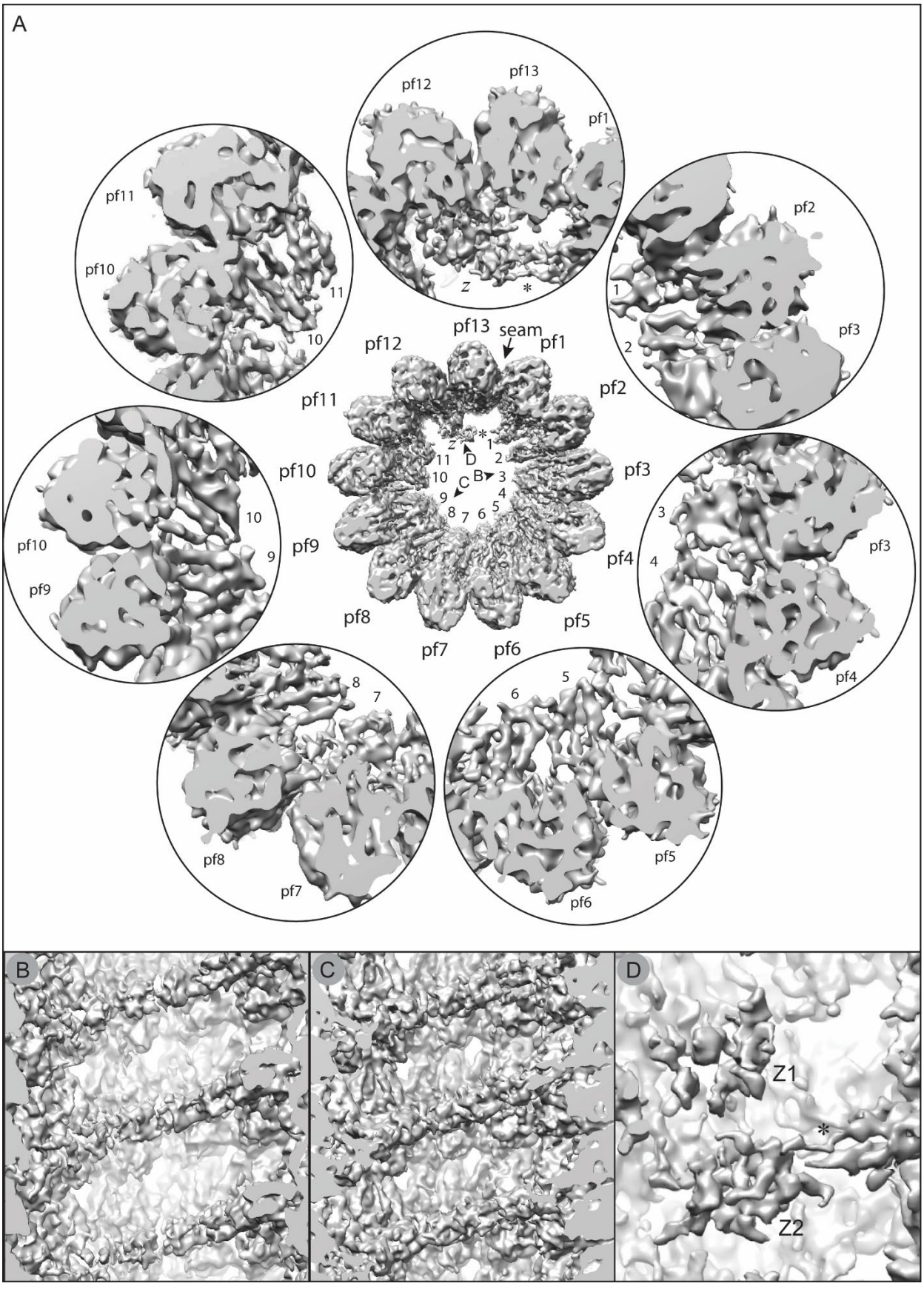
A
pf12
pf13
pf1
pf11
pf10
11
10
z
*
pf2
1
pf3
2
seam
pf12
pf13
pf1
pf11
pf2
z
*
1
11
D
2
10
B
3
C
4
9
8
7
6
5
pf10
pf3
pf9
pf4
pf8
pf5
pf7
pf6
10
pf10
9
pf9
3
pf3
4
pf4
8
7
pf8
pf7
6
5
pf5
pf6
B
C
D
Z1
*
Z2

4.3.2 The TAILS C-shaped segment is made up of 4 unique folds, plus an additional two folds forming the zipper

The high-resolution structure of TAILS revealed 3 major classes of MIP fold, which we have designated fold A, B, and C (Fig 4.3.1A). Fold A comprises 2 different but similar folds, which we have classified "A1" and "A2" respectively. Fold A1 is formed by a total of 4 alpha-helices, whereas 3 only of these helices are retained in A2. The A2 fold is always found in close association with an A1 fold, as in MIPs 5&6, 8&9, 10&11, while MIP4 is the only location in which the A1 fold has no accompanying A2 fold (Fig 4.3.1B). The B fold is formed by MIPs 1 and 2, and is the smallest of all of the folds. Both MIPs exhibiting the B fold were reconstructed at lower resolution than the rest of the structure, implying flexibility of this region and making it difficult to ascertain whether or not they are the same (Fig 4.3.1A). However, due to their similar size and basic shape, for now they have been classified as the same fold. In contrast to A and B folds, the C fold is easily recognized by the prevalence of beta sheets throughout its structure, most obvious from the top view (Fig 4.3.1A). Furthermore, the C fold is always followed by a copy of the A1 fold. The overall arrangement of folds, starting from protofilament 1 are as follows: 2 copies of the B fold, followed by the C fold and an A1 fold, then an A1-A2 pair followed by another C fold, and finally ending in two more A1-A2 pairs. Although there are some consistencies in this arrangement (C is always followed by A1, A2 is always preceded by A1), the structure as a whole forms a single asymmetric unit for each 8 nm repeat (Fig 4.3.1). Unfortunately, it cannot be ascertained at the current resolution how many distinct polypeptide chains make up the structure, so whether or not neighboring folds are part of the same protein remains unclear. The close association of A1 and A2 folds however would suggest these two belong to the same protein, although this is contradicted by the lone A1 fold that forms MIP4.

In addition to TAILS, a structure that we here name the "zipper" binds between protofilaments 12 and 13, repeating in the gap left by the TAILS complex (Fig 4.3.0A (marked by "z"). Unlike the C-shaped structure of TAILS, which has a periodicity of 8 nm, leaving an empty tubulin monomer between repeats, zipper densities occur every 4 nm (Fig 4.3.0D). However, the zipper comprises two different folds that each have a periodicity of 8 nm, alternating every 4 nm. We have named these folds Z1 and Z2. Each zipper density forms contacts with one side of the C-shaped structure (Fig 4.3.0A, D). Zipper density Z1 contacts MIP11 in such a way that it could be considered the final density of the C-shaped segment. The Z2 density, however, is connected to MIP1 of the C-shaped segment by a unique "bridge" structure (Fig 4.3.0A, D (indicated by asterisks)). This bridge was visualized in the subtomogram averaging as well, albeit only at high density threshold. Likewise, the bridge is not as clearly resolved in the single particle structure as the Z1, Z2, or MIP1 densities, all of which were reconstructed at lower resolution than the remaining components of the C-shaped structure (6.5 Å vs 4.8 Å estimated resolution after masked refinement), indicating the flexibility of the zipper and bridge densities.

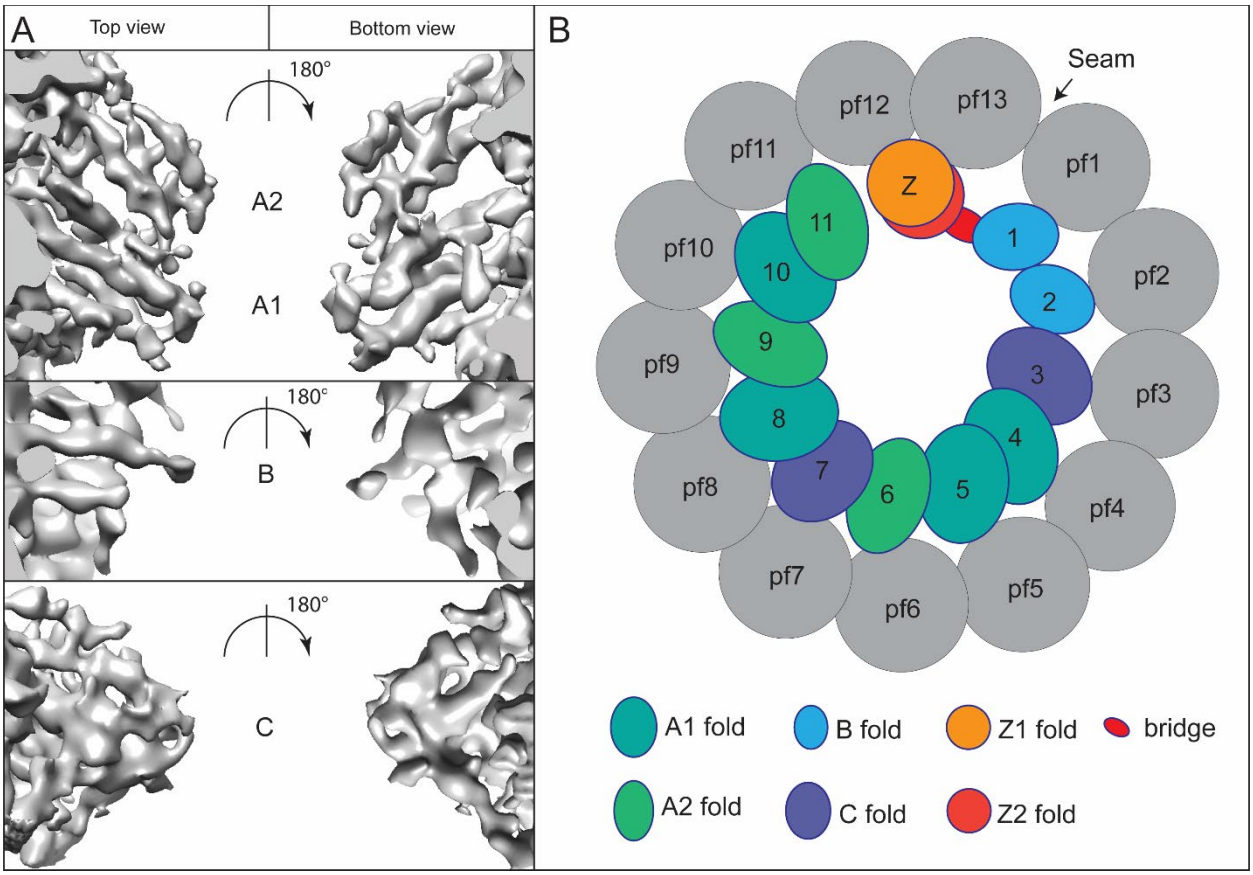

Figure 4.3.1 Several repeated folds form an asymmetric pattern in TAILS

TAILS is made up of unique folds that repeat in an asymmetric pattern throughout the C-shaped segment, and an additional two folds that make up the zipper (Shown in detail in Fig 4.3.1) that interacts with MIP1 via the bridge. (A) Close up views of each unique fold are shown from the same perspective as Fig 4.3.1 on the left, and as viewed from below on the right. Folds are labeled A1, A2, B, and C folds. (B) A cartoon model of TAILS demonstrates the arrangement of these folds throughout the structure. Protofilaments are labeled "pf1-pf13", and MIP designations are simply numbered 1-11. Although the structure is asymmetric when taken as a whole, two basic rules apply. C folds are always followed by an A1 fold, and A2 folds are always preceded by an A1 fold. The A1 fold does not have to be followed by an A2 fold however, which is the case for MIP4. Since the zipper folds alternate every 4 nm, the Z2 fold is drawn underneath the Z1 fold and connected to MIP1 by the bridge.

4.3.2 TAILS and the zipper alter the rotation of each protofilament

Since MIPs have been shown to change the angles between protofilaments, and thereby the lattice structure (139), we measured the distance between tubulin monomers and the angles between protofilaments. The average inter-dimer distance of the TAILS-bound microtubule was 40.5 Å, consistent with the compact lattice that exists in GDP-bound microtubules (140).

In a perfectly symmetrical 13 protofilament microtubule, neighboring protofilaments would be expected to be rotated 27.7 degrees with respect to each other. However, in a TAILS-bound microtubule, pairs of protofilaments deviated from this value with a range of about 3 degrees in either direction (Fig 4.3.2A-B). Strikingly, both the greater and lesser extremes were found in the angles on either side of protofilament 1 (angles labeled a and m), demonstrating that this protofilament was rotated outwards by about 3 degrees. The microtubule seam was located between protofilaments 13 and 1, the pair of protofilaments that form the widest angle. This is consistent with a slight opening of the seam observed in undecorated microtubules, polymerized *in vitro* (140). Another large positive deviation in protofilament angles occured between protofilaments 4 and 5 (Fig 4.3.2A-B, labeled angle d). Notably, these protofilaments were the only two linked by two copies of the A1 fold. All of the angles formed where pairs of A1/A2 folds interact show slight negative deviations demonstrating the interaction between two A1 folds has a different effect on the microtubule than the A1/A2 pair, despite the similarity in structure.

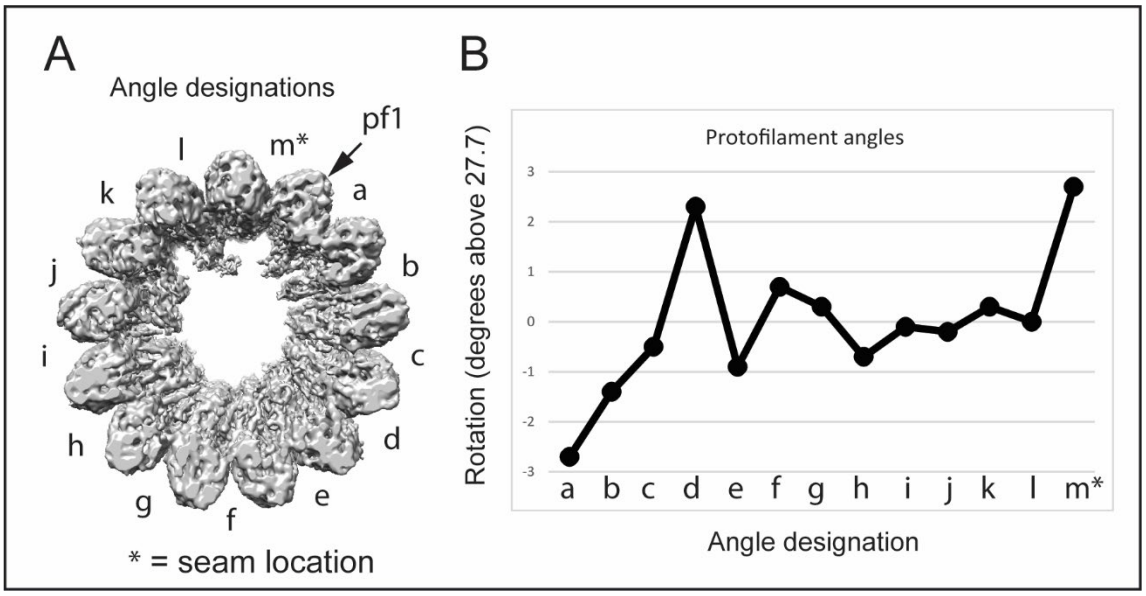

Fig 4.3.3 TAILS affects the rotation of individual protofilaments

The angles between each protofilament of the TAILS-bound microtubule were measured. (A) Angles were designated with letters starting with angle a between protofilament 1 and 2 (B) Plot of deviation of each angle from the value 27.7 expected from a symmetrical microtubule. Values on the Y axis indicate the difference between the angle measure and 27.7, in degrees.

Interestingly, there are no MIPs that contact the seam directly. Instead, an interaction we are calling "the bridge" is formed between MIP1 which binds between protofilaments 1 and 2, and Z2, which binds between protofilaments 12 and 13. The bridge must either be rather flexible, or formed by another protein exhibiting lower occupancy, because it is not as clearly resolved as the rest of our structure and is only visible after masked refinement. Similarly, the bridge only appears at high density threshold in the subtomogram average. Nevertheless, the bridge establishes

continuity between adjacent segments of TAILS, and likely adds support to the seam, which is usually thought of as a point of weakness in the microtubule (138).

Furthermore, the presence of the bridge implies that despite the gap in the TAILS C-shaped structure, TAILS is likely able to influence stability around the entire circumference of the microtubule and establish continuity with the next 8 nm repeat of TAILS in the following manner: Each of the 11 segments of the C-shaped structure form interactions with their neighboring MIPs, starting from MIP1 all the way around to the Z1 density, which could be considered the end of the C-shaped structure. Although Z1 binds within a heterodimer, Z2 binds at interface formed by the next heterodimer longitudinally, and is also connected to MIP1 by the bridge. Thus, the chain of interactions begins again for the next 8 nm repeat.

4.4 Assessment of TAILS candidates

4.4.0 Proteomics of the human sperm flagellum tip

Since proteomics studies have detected well over one thousand proteins to be present in the mammalian sperm flagella (126–130), many of which are of unknown function, a method for enriching flagella tips was developed. Bovine spermatozoa were broken up by light sonication, and fractionated by a series of two sucrose density gradient centrifugations (Fig 4.4.0A). Since each segment of the mammalian sperm flagellum decreases in thickness distally, sperm heads, midpieces, principal pieces and endpieces are expected to sediment at different rates. Negative stain EM was used to assess the content of each fraction (Fig 4.4.0A). Endpieces can easily be differentiated from broken pieces of other segments of the flagella in negative stain images due to their reduced thickness, and the number or tips vs. “necks” (the connecting piece between the midpiece and sperm head) was compared in each sample. Since perfect isolation of tip fractions could not be achieved by this method, “tip-enriched” fractions exhibiting at least 2-fold enrichment in tips vs necks as well as “tip-depleted” fractions were analyzed using quantitative mass-spectroscopy. A total of 1913 proteins in total were identified in both samples, and using a cut-off value of 50% enrichment in the tip-enriched sample compared to the tip-depleted sample, a total of 70 proteins were identified (Fig 4.4.0B). To our knowledge, this represents the first proteome of the flagellum tip in any species.

Notably, among the proteins enriched at the tip was DCDC2C, which was previously found to be localized at the endpiece of the human spermatozoon (130). We wanted to confirm this finding, so we performed immunofluorescence against DCDC2C and tubulin in bovine spermatozoa (Fig 4.4.0C). Tubulin exhibited staining across the length of the flagellum, albeit with higher intensity at the endpiece and necks, indicating these regions are more easily made permeable to antibodies than regions encased in the fibrous sheath and other accessory structures. DCDC2C, however, was only detected at the flagellum tip, confirming previous findings and is a first indication of successful enrichment of tip proteins in our proteomics data. To be certain of our flagellar tip proteome more protein localizations need to be tested. We are currently working to identify

potential TAILS candidates from this list of 70 using a combination of approaches, before testing their location along the sperm tail as well.

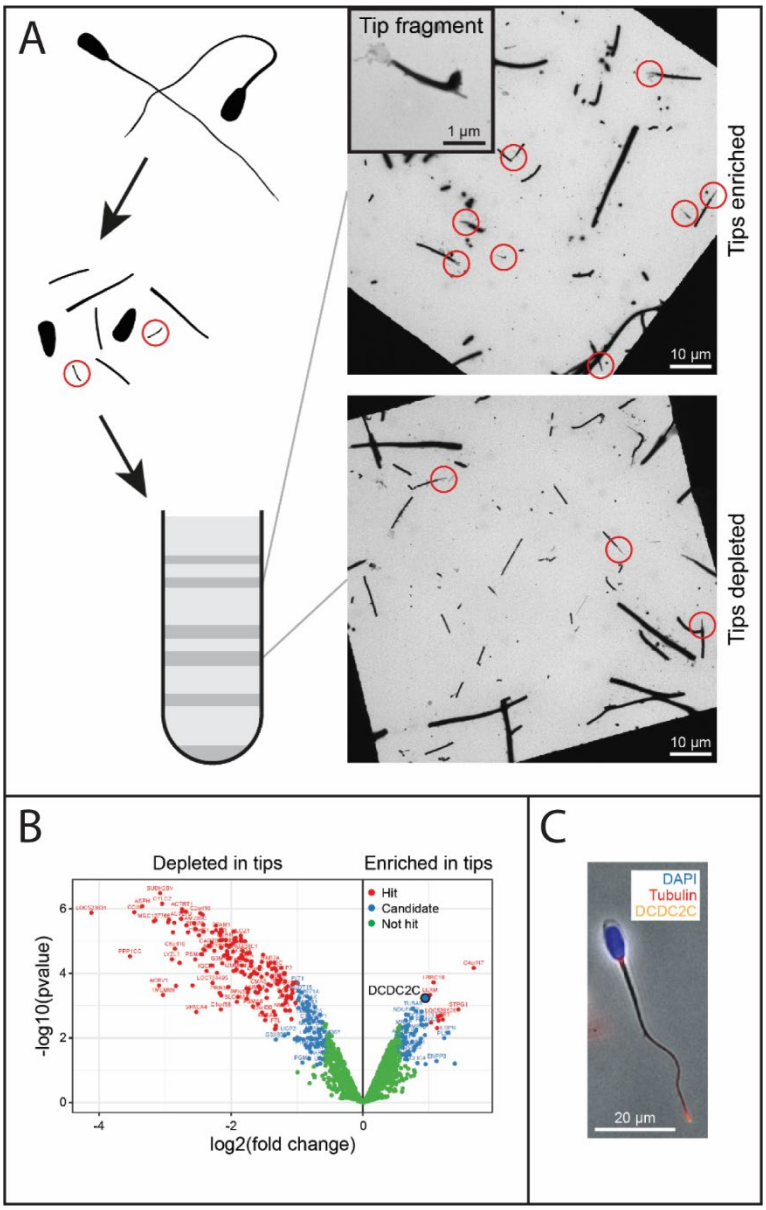

Figure 4.4.0 Enrichment and proteomics of flagella tips

(A) Sonication was used to fragment sperm cells, and these fragments were separated on a sucrose density gradient. Negative staining was used to assess for enrichment of tips, which are indicated with red circles. (B) Samples enriched in tips, as well as a depleted (control) sample were analyzed by mass spectrometry. The volcano plot indicates enrichment of proteins in either fraction compared to the other. Green dots represent proteins that were not enriched in either,

blue dots are slightly enriched proteins, and red dots indicate highly enriched proteins. (C) Immunofluorescence of tip protein DCDC2C confirms its predicted tip localization.

4.4.1 Narrowing down the candidate list

To further narrow down the 70 proteins enriched in flagellum tips, a comparative genomics approach was used (Fig 4.4.1A). All the species investigated for the presence of TAILS using cryo-ET have had their genomes sequenced and annotated. For each candidate we performed BLAST searches against the genomes of all species investigated to ascertain which contain homologous proteins, using an e value of .001 as an arbitrary cutoff to define homology. Using this information, we excluded candidates that did not have homologous proteins predicted in all of animal species investigated, as well candidates that also had homologs in the protists (Fig 4.1.1A). Like this, we could narrow the list to only 20 candidate proteins. Of these, 8 are either known or predicted to be membrane proteins, leaving just 12 high priority candidates (Table 4.4).

Gene name	Description
FAM228B	family with sequence similarity 228 member B
RACGAP1	Rac GTPase activating protein 1
DNASE1L3	deoxyribonuclease 1 like 3
FAM81B	family with sequence similarity 81 member B
CSRP1	cysteine and glycine rich protein 1
RNASE4	ribonuclease A family member 4
TFPI2	tissue factor pathway inhibitor 2
MDM1	Mdm1 nuclear protein
POF1B	POF1B actin binding protein
LEXM	lymphocyte expansion molecule
DCDC2C	doublecortin domain containing 2C
EFCAB12	EF-hand calcium binding domain 12

Table 4.4 TAILS candidates identified by proteomics and comparative genomics

TAILS candidate proteins identified in the bovine sperm tip proteome and 20 were selected because they have homologs in human, chicken and frog but they do not have homologs trypanosomes nor in Chlamydomonas. This list was further narrowed down to this list of 12 by removing predicted membrane proteins.

A weakness of this approach is that it assumes the same set of proteins forms TAILS in each of the vertebrate species containing it, and that there are not homologous proteins that perform different roles or decorate the inside of non-flagellar microtubules in the protist species that were used to exclude candidates. Nevertheless, this list contains several promising candidates. The three candidates MDM1, DCDC2C, and EFCAB12 all contain known microtubule binding domains. EFCAB12 contains an EF-hand calcium binding domain, which is shared by at least 8 known MIPs in the doublet microtubule of *C. reinhardtii* (115). Other candidates, such as FAM228B and FAM81B are interesting because they are completely uncharacterized.

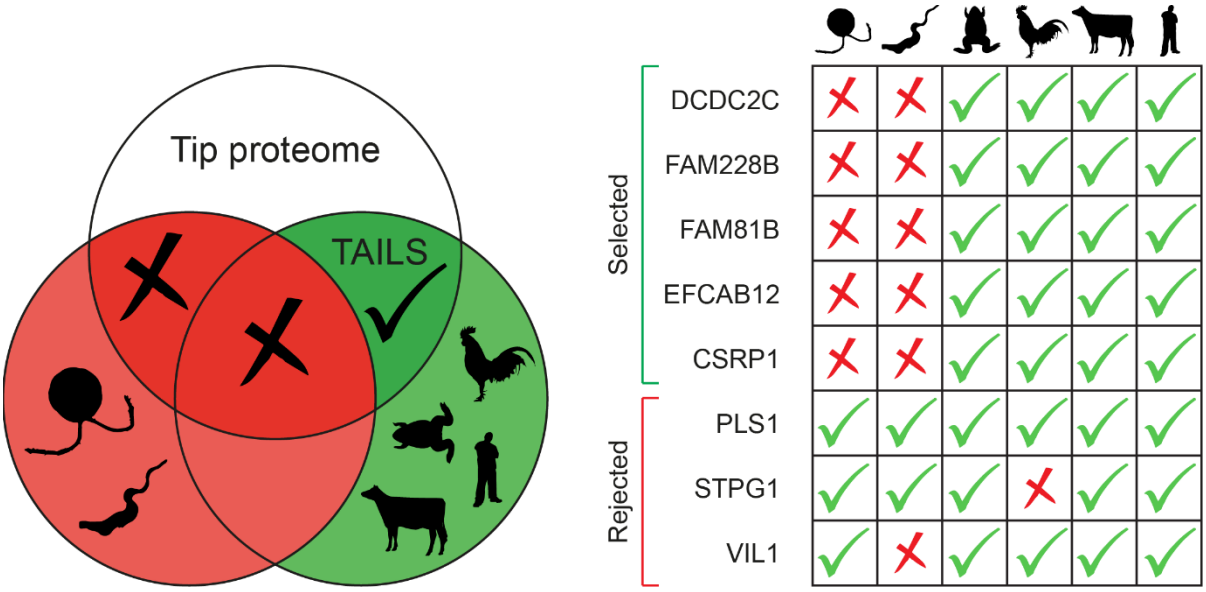

Figure 4.2.1 Narrowing down candidates by comparative genomics

A visual representation of the comparative genomics approach. BLAST searches were performed for all 70 proteins in the tip proteome against the 6 organisms that have been investigated for presence of TAILS. Only proteins homologues shared in the organisms Xenopus laevis, Gallus gallus, Bos taurus, Homo sapiens, but not present Chlamydomonas reinhardtii or Trypanosoma brucei were kept as high priority candidates.

4.4.2 Assessing candidates by structure

In addition to narrowing down candidates in the tip proteome by comparative genomics, a structural approach was taken to identify potential TAILS proteins as well. The work in this section is currently ongoing, although has provided some initial findings detailed here.

Three approaches are being implemented to identify possible TAILS proteins by structural methods:

1) Fitting of over 30,000 unique domains via the molrep/BALBES pipeline into the electron density maps generated by SPA.
2) Fitting of homology models generated for each of the candidates identified by comparative genomics into the electron density maps generated by SPA.
3) Fitting of structures of known MIPs into the electron density maps generated by SPA.

The first approach, using molecular replacement software to individually fit the BALBES library of over 30,000 unique protein domains has yielded some plausible fits, yet so far none of the identified domains have been consistent with proteins enriched in the tip region as identified by our proteomics data, and neither fits or candidate proteins identified this way are convincing enough to warrant biochemical validation of any of these proteins. Several unknown proteins

have been identified by other groups via this method (115), although with structures exhibiting greater resolution. Therefore, we plan to increase resolution of repeating folds in our data by imposing local symmetry, and then try again with this approach.

To carry out the second approach, homology models were created for each of the candidate proteins in table 4.4 using SWISS-MODEL (141). This program generates a series of homology models for individual domains, resulting in multiple models for each protein. So far, some small domains have yielded plausible fits, although no obvious best candidate has emerged. We will continue by trying to fit multiple domains simultaneously, and generating homology models for whole proteins with I-TASSER (142).

The third approach has yielded some interesting results. Although not all structures of known MIPs have been fit into each fold yet, a promising candidate for the beta-sandwich structure of the C-fold has emerged (Fig 4.4.2). The structure of FAP363, which contains an Hsp70 domain, appears to fit this fold quite well. The human homologue of this protein, HSPA9, was enriched in the flagellum tip in our proteomics data, although is not listed in our 70-protein tip proteome because it is just below the arbitrary cutoff value. Interestingly, this protein has a known function in the mitochondrion (143), although it is possible it could perform a different function in the flagellum. Due to the quality of the fit into the C-fold, and the known localization of HSPA9 homologue FAP363 in the A-tubule lumen of the *C. reinhardtii's* doublet, this protein is a viable candidate.

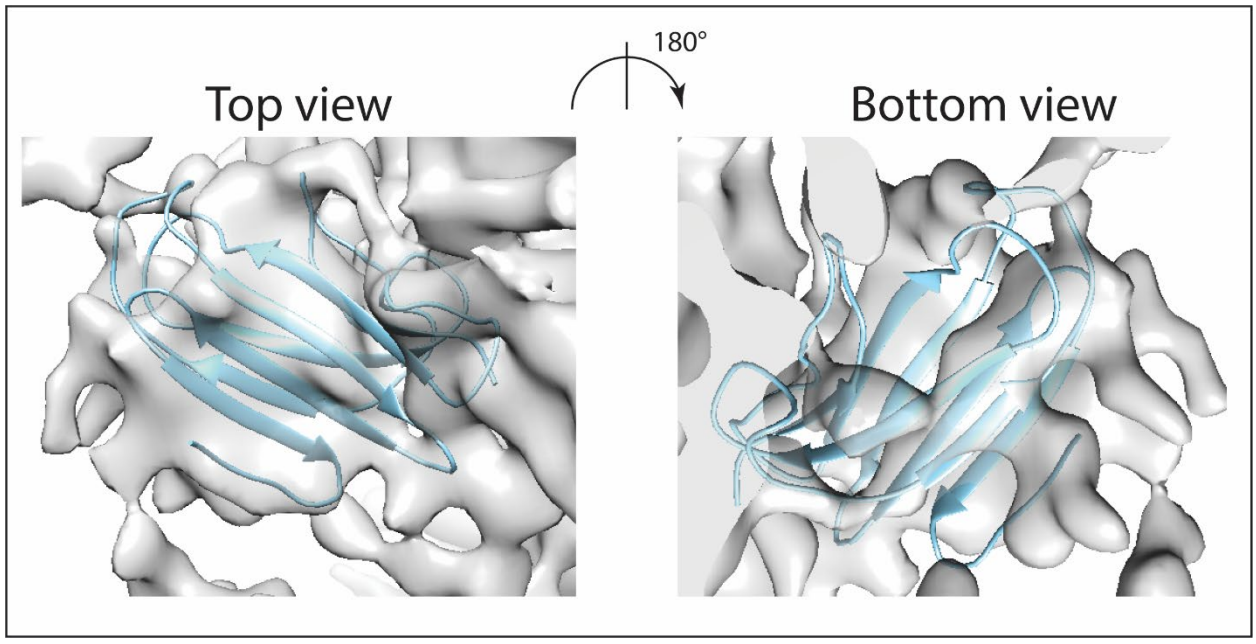

Figure 4.4.2 Fitting of Chlamydomonas MIP FAP363 into the TAILS C-fold MIP3

The structure of the Hsp70 domain of FAP363 (Blue), a known doublet MIP, yielded a convincing fit into MIP3 of TAILS, which forms a C fold. The PDB accession number for FAP363 is 6U42, chain 5L (115).

Chapter 5: Structure of human doublet microtubules

5.0 Introduction

In contrast to the cytoplasm, in which only singlet microtubules occur, the doublet microtubule is the primary form microtubules assume in the flagellum. Together with the dynein arms attached along their lengths, the doublet microtubules are the motor behind the flagellar movement and its structure has received a lot of attention especially by cryo-electron microscopists (87,114–116,118,139,144,145). However, the structure of doublet microtubules in human flagella are less studied. The first, and only, high-resolution investigation of human doublet structure revealed it to be different to that found in the common model organisms *C. reinhardtii* and *T. thermophila,* and more similar to the doublet microtubule structure found in the sperm flagellum of a sea urchin (85). Another unanswered question is if there are structural variations in the doublet microtubules along the flagellum length, as it is not always possible to determine where along the flagellum length the structural data has been acquired. Doublet microtubules derived from model organisms are often detached from the cell and isolated in a flagellar preparation. In our human sperm cell preparations, the head is still attached to the tails and images can be acquired of only the microtubules near the distal tip. Therefore, we present here the highest resolution structure of human flagellar doublet microtubules, and its associated MIPs, to date, from the most distal part of the sperm tail.

However, from studies of model organisms have revealed a lot about flagellar structure. The central pair and doublet microtubules are connected to each other by a variety of structures which collectively make up the axoneme, which repeats every 96 nm (87,146). Doublets are connected to each other every 24 nm by the outer dynein arms, which are responsible for generating the force to create the flagellar beat (147). Additionally, they are linked by 7 inner dynein arms, of which one is heterodimeric and 6 are monomeric, and are not evenly spaced throughout the 96 nm repeat (85,114,146). In addition, the nexin-dynein regulatory complex occurs once per repeat and is responsible for the regulation of dynein (148). The central pair microtubules are linked to each other by the central pair complex (149), and to the doublet microtubules by three radial spokes (85,150).

Doublet microtubules are formed by an A-tubule, which is essentially a normal 13-protofilament singlet microtubule, attached to a 10 protofilament B-tubule. The B-tubule attach to the outside of the A-tubule at two locations: the outer and inner junctions, of which both differ in structure and composition. At the outer junction, protofilament 1 of the B-tubule contacts two protofilaments of the A-tubule, and a few small proteins stabilize the interactions (115). The structure of the inner junction is more complicated, and tubulin from the A and B tubules do not directly contact each other at this site. Instead they are tethered by a complex of several different proteins, exhibiting periodicities of 8 and 16 nm (115,118). Two of these proteins, PACRG and FAP20, alternate forming a filament between protofilament b10 of the B-tubule and the A-tubule (115,118) that was once thought to be an eleventh tubulin protofilament.

The doublet microtubules themselves are held together by a complicated web of proteins binding both within their lumen, as well as on their outside surface. This network of doublet MIPs has a periodicity of 48 nm, occurring twice during each repeat of the axoneme. Originally, doublet MIPs were discovered by electron tomography (87,114) and their identities were unknown, but distinct structures with different periodicities were recognized. These structures are thought to stabilize the doublet, and some perform the role of "molecular ruler", by creating unique binding sites along the 48 nm repeat for the others (115,151). Axonemal doublets of several different organisms were investigated by electron tomography, revealing some similarities but also variations in each network of MIPs (85,115,139,144,152). For example, the partition region formed by the protofilaments of the A-tubule that are located between attachment points of the B-tubule is twice as thick in the doublets of *S. purpuratus* compared to *C. reinhardtii* (144), however whether or not this extra density is filamentous has been debated (87,144). Later, higher resolution averages of doublets from *T. thermophila* revealed that in addition to the previously observed large globular MIPs in the microtubule lumen, another class of filamentous MIPs called "fMIPs" exist, usually taking the form of a single alpha-helix binding between two protofilaments at various points in the doublet microtubule (139). Recently, SPA was used to characterize the structure of the inner junction MIPs at high resolution and identify the locations of protein components at this site (118), and another group determined the structure of the entire *C. reinhardtii* doublet, thereby identifying 38 new proteins and revealing the complex web of interactions they form to create the 48 nm repeat (115). Individual components of this structure repeat every 8, 16, 24, or 48 nm, and the network spans from the inside to the outside of the microtubule, establishing binding sites for the inner and outer dynein arms, as well as the nexin-dynein regulation complex.

Many of the 38 proteins identified in *C. reinhardtii* have orthologs in humans, and defects in several of these proteins are associated with disease (115). This highlights the importance in identifying all of the MIPs in human flagella in order to better understand the mechanisms of ciliopathies. However, at least 18 of these proteins do not have human orthologs, indicating the human flagella may have its own set of unique proteins. Subtomogram averaging has been performed on the human axonemes, revealing MIPs in the doublet lumen (85). However, this study was mainly focused on the radial spokes, and since the subtomogram averaging was performed on a large region containing several axonemal structures, the resolution of the doublet MIPs is limited making it difficult to compare to the higher resolution structures of doublet in other organisms. In the only study involving post-axonemal human doublet microtubules to date, TAILS was discovered binding in the doublet just before the transition to the singlet region (27).

When micrographs were collected of microtubules exposed by the demembranation protocol outlined in Chapter 4.1, the dataset contained a mixture of doublet and singlet microtubules. While initially the doublets were considered to be "contaminating" the micrographs, we later realized they provided an opportunity to study the small fraction of doublet microtubules that is found distal to the axoneme: the doublets occurring between the axoneme and the singlet region. We therefore refer to this population of doublets as post-axonemal doublets, and reconstructed their 8 nm repeat using SPA at a resolution of ~7 Å, revealing a unique filamentous structure in

the A-tubule. At time of printing of the thesis, this work is ongoing. Several populations of doublets existed in the data set, including a class which appeared to be decorated by TAILS in the A-tubule, and possibly in the B-tubule as well although this region isn't well resolved in the current reconstruction. To date most of the work on the doublet structure has been conducted on the class containing filamentous structures, since this was the most unique and striking finding.

5.1 Methodology

The method of preparing singlet microtubules for SPA described in Chapter 4 also allowed for doublet microtubules located in the endpiece to be imaged as well. Therefore, the same sample preparation procedure described in Chapter 4.1 was used for the doublets. In fact, doublets and singlets were imaged at the same time, resulting in a dataset containing micrographs of just doublet microtubules, mixtures of doublet and singlet microtubules, and just singlet microtubules.

While the data collection was identical to that described in Chapter 4.2, the data processing strategy was similar but adapted to suit the doublets. Motion correction and CTF correction were applied in Relion exactly the same as described in Chapter 4.2 (32,136). However, particles were extracted with a larger box size (600 Å for the doublets vs 500 Å for the singlets), in order to accommodate the larger size of doublet particles. A spacing of 82 Å between particles, and pixel size of 1.06 Å / pixel were used. Particles were then exported to cisTEM, junk particles removed by 2D-classification, and multireference refinement used to separate doublet and singlet particles. Since a doublet microtubule laying on its side resembles a singlet microtubule, all microtubules in the images were picked and heterogeneity was sorted out at this step. Autorefine was performed in cisTEM, using a doublet microtubule only featuring tubulin, with no MIPs, as an initial reference. After initial alignment, 3D-classification revealed 3 classes of doublets. One class exhibited large filament bundles in the A-tubule, and was refined further. Similar to the singlet microtubules, masked refinements were performed to increase resolution of individual regions. The second class contained a decoration similar to TAILS with a periodicity of 8 nm in the A-tubule, and third class had very few particles and has a filled A -tubule and a very disordered B-tubule. These classes will be further refined, but have not been studied extensively at the time of writing.

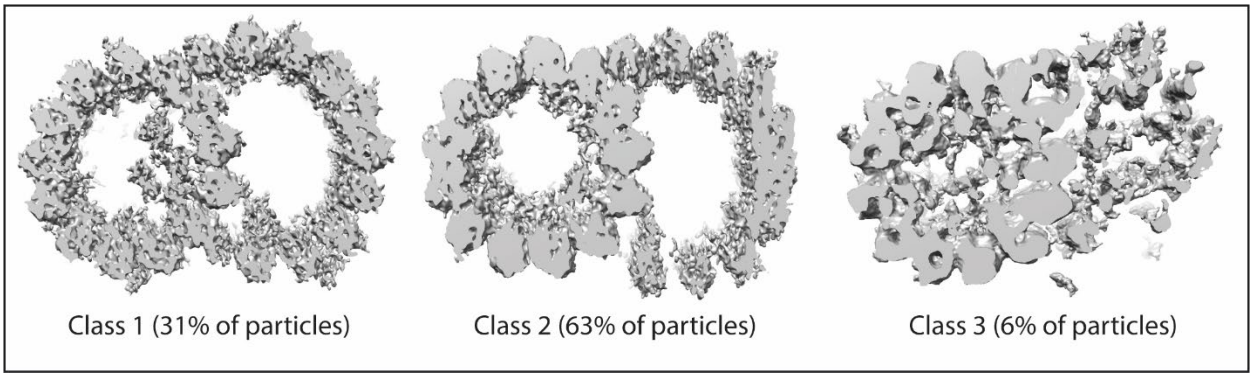

Fig 5.1 Structural heterogeneity in post-axonemal doublets

3D-classification of doublets extending from the tips of demembranated sperm flagella revealed 3 subsets of particles. Class 1 was dissimilar to any doublets structures that have been reported to date, containing large filamentous densities in the A-tubule lumen. Therefore, most of the work thus far has focused on this class. The second class appeared to contain TAILS, and was the most populated of the three classes. This reconstruction suffered from high amounts of solvent noise and will be improved after the publication of this thesis. The third class, containing only 6% of particles, did not have a complete B-tubule and also a variety of other structures. This class may not be biologically relevant, and likely represents a combination of damaged doublets in the dataset.

5.2 Structure of human post-axonemal doublet microtubules

The structure of the 8 nm repeat of doublet microtubules from the tip of human sperm flagella was determined to an overall resolution of 7 Å. In this overall structure containing all of the particles, the resolution was sufficient to differentiate alpha and beta tubulin by the same method discussed in Chapter 4.2. The seam was located between protofilaments a9 and a10, consistent with the seam location in the doublets of other organisms (115,139). Subsequently, 3D-classification revealed 3 main structural classes of particles. Strikingly, one class, containing 31% of the particles, contained a filamentous structure in the A-tubule lumen (Fig 5.2.1A-C). Another class had a C-shaped decoration similar to TAILS with a periodicity of 8 nm in the lumen of the A-tubule (63% of particles), although exhibited some differences to the TAILS decoration in singlet microtubules. The final class most likely represented doublets with damaged or aberrant B-tubule structure (6% of particles).

Then, the class containing large filamentous densities in the A-tubule was separated and processed further, using cylindrical masked refinements to improve resolution of several areas. The filament bundles appear connected to protofilaments a10, a12, a13, and a1 (Fig 5.2.1A). Viewed from inside the lumen, two distinct morphologies of filaments are evident (Fig 5.2.1 B-C). The filament that is connected to protofilament a10 appears to be formed by stacked subunits taking on more of a globular fold. However, the filaments contacting protofilament a1 are more accurately described as a bundle of extended filamentous densities aligned close to parallel with the microtubule axis. Although, filamentous actin has found inside the lumen of microtubules extruded from HAP1 cells (153), the morphology of the filaments found in our structure differs from that of actin (154). Instead, we find it likely that these filaments are composed of proteins from the tektins family. Tektins are intermediate filament-like proteins that are known to bind the microtubules of flagella, occurring throughout evolution although varying significantly in sequence and number of tektins proteins encoded between organisms (155). Periodicities of tektins filaments are consistent with multiples of the 8 nm tubulin lattice (156), and have been proposed to carry out stabilizing roles and molecular ruler functions. Furthermore, the treatment of axonemal doublet with the detergent sarkosyl strips all of the protofilaments except those in the partition region between the A and B tubule, forming stable protofilament “ribbons” which contain tektins and other coiled-coil proteins (157).

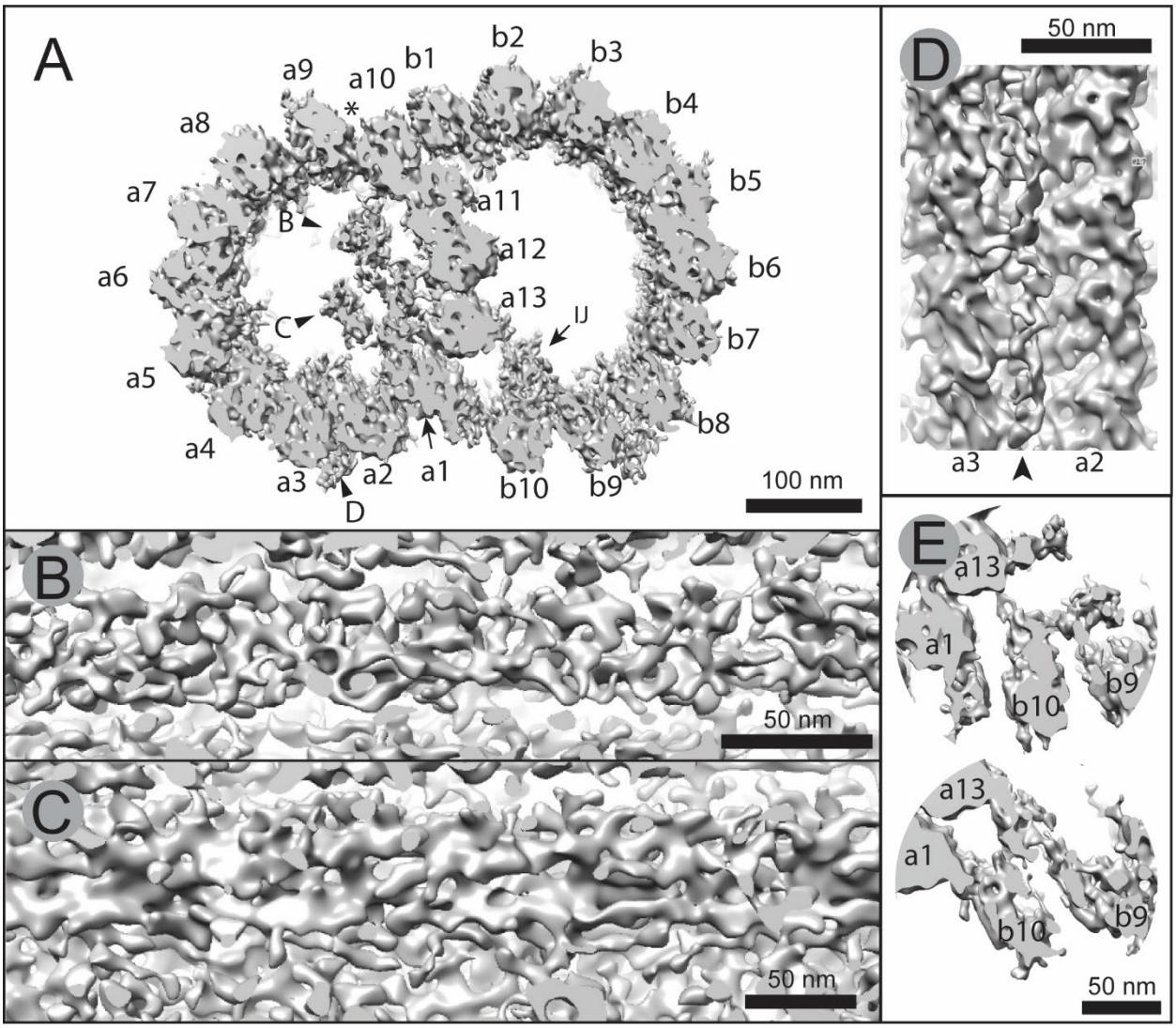

Fig 5.2.1 The A-tubule of human doublet microtubules contains extensive filamentous densities

SPA of human doublet microtubules from near the tip region of sperm flagella revealed a class of doublets containing large filamentous structures in the A-tubule. (A) The overall structure is shown, with protofilaments of the A-tubule labeled a1-13, and of the B-tubule labeled b1-10. An additional smaller 11th "protofilament" is visible contacting protofilament a1, which is known to be composed of PACRG and FAP20 rather than tubulin (116)*. Additional inner junction densities are labeled IJ and indicated with an arrow. (B-C) Intralumenal views of the filamentous structures within the A-tubule. Perspectives of each view are indicated by arrowheads in the lumen of the A-tubule in panel A. (D) A coiled-coil structure binds outside the A-tubule between protofilaments a2 and a3. It is known to be formed by a complex of CCDC39/40* (151)*. The perspective of panel D is indicated by an arrowhead in panel A. (E) Two different structures occurring at the inner junction are shown, revealed by 3D-classification.*

In addition to the large filamentous densities within the A-tubule, several other densities decorate the doublet microtubule. For example, a small coiled-coil density binds along the cleft between protofilaments a2 and a3 on the outside of the microtubule (Fig 5.2.1D). This is consistent with the location of a complex of the proteins CCDC39 and CCDC40, which has been shown to function as a molecular ruler and define the 96 nm repeat of axonemal complexes on the outside of the doublet such as radial spokes and the nexin dynein regulatory complex (115,151,158). Since the periodicity of this protein is known to be 96 nm, and our particles were extracted every 8 nm, different segments of this protein must have been averaged together in our data, yet the basic coiled-coil structure was consistent throughout. Additionally, there is a globular density binding on the inside between protofilaments a2 and a3 as well. Another coiled-coil structure formed by the outer dynein arm docking complex is known to bind between protofilaments a8 and a9 (115), however our structure is lacking a density in this location. It would make sense that this structure would not be present in post-axonemal doublets, although it is interesting that the CCDC39/40 complex, which provides a binding site for the radial spokes is retained. In contrast to these coiled-coil structures, a globular density binds to the outside of the B-tubule between protofilaments b8 and b9 in our structure. Furthermore, additional structures connect the B-tubule to the A-tubule.

The region which connects protofilaments b1 to a10 and a11, is termed the outer junction, whereas the region that connects protofilaments b10 to a1 and a13 is termed inner junction. While protofilament b1 contacts protofilaments of the A-tubule directly at the outer junction, it is supported by only a few small additional structures. At the inner junction this connection is formed by a complex of several proteins with a periodicity of 16 nm (115,116,118). To account for this 16 nm periodicity, we performed 3D-classification of our 8 nm particles focused on the inner junction region with two classes (Fig 5.2.1E). This revealed two distinct structures at the inner junction, although the reconstruction of tubulin in protofilaments b10 and b9 was poor, and we resolve to improve our reconstruction before drawing any conclusions about the conservation of the inner junction of human doublets with structures studied in other organisms. Furthermore, the resolution of tubulin in the B-tubule in the overall structure is lesser than that of the A-tubule, and appears somewhat smeared indicating the B-tubule is likely more flexible.

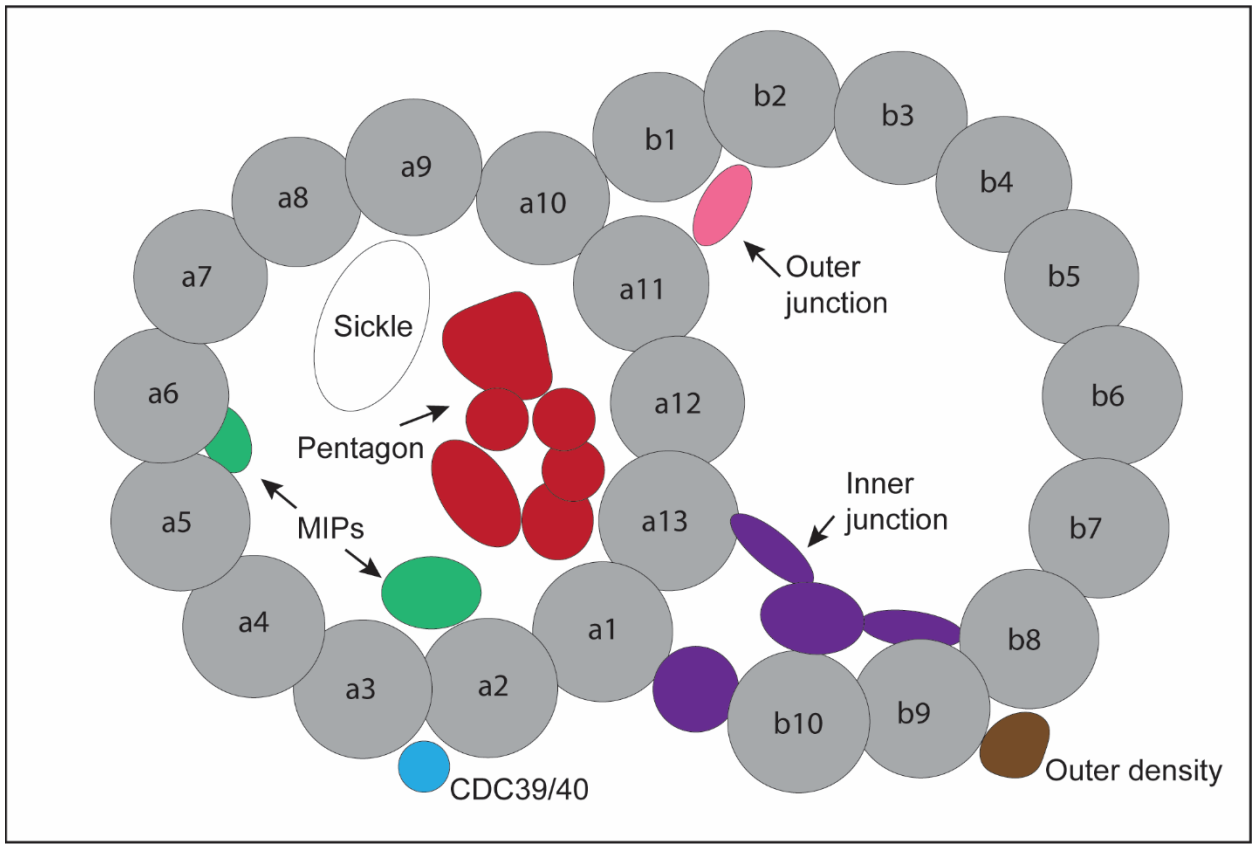

Fig 5.2.2 Model of post-axonemal doublet microtubules

A cartoon representation of the structure of doublet microtubules occurring after the loss of axonemal components, but before the appearance of TAILS in the doublet lumen. Filamentous densities previously called the "pentagon" (red) and the "sickle"(transparent) (83) *extend in axonemal doublets, but the sickle terminates along with the axonemal components. We postulate these structures may be composed of tektins. Globular MIPs (green) are located between protofilaments a2/a3 and a5/a6, of unknown identity. A small coiled coil (blue) located on the outside of the A-tubule between protofilaments a2 and a3 is consistent with the location of the CDC39/40 complex in other organisms* (115,151)*, and performs a molecular ruler function. The outer junction (pink) and inner junction (purple) are composed of several MIPs and appear similar to structure published of this region in other organisms. Finally, a density is seen binding the outside of the B-tubule (brown) between protofilaments a8 and a9.*

The most unique feature of these post-axonemal doublets, compared to the axonemal doublets of other organisms, was the presence of large filaments inside the A-tubule. Similar structures, called "the pentagon" were visualized in the axonemal doublet microtubules of human sperm in another study by averaging images of microtubules cut in cross section (83). This clever method of averaging cross sections to create a 2D image with increased contrast was devised before the advent of modern 3D-EM techniques, and due to the morphological similarity of both structures, we conclude that the pentagon structure is composed of filaments that extend the entire length of the axoneme and continues after loss of other axonemal components. Another density, called

"the sickle", appearing beside the pentagon was present in the axonemal doublets of healthy spermatozoa, but not from those obtained from men with immotile cilia that lack dynein arms (83). A density corresponding to the sickle does appear in our reconstruction, but only at very high density threshold. Further 3D classification will be performed to determine if this is due to low occupancy of the sickle in our particles. Although the donors in our study were confirmed to produce healthy, motile spermatozoa, the lack of the sickle in our structure is consistent with doublets lacking dynein arms. Furthermore, similar filamentous structures can be seen in the previously published subtomogram average of human nasal axonemes that also appear connected to tubulin at protofilaments a3 and a6, as well as filamentous density in the B-tubule (158). Since this study did not focus on MIPs, but instead on the structure of other axonemal components, this is not mentioned in the paper but is clear in the deposited EM map (EMDB entry 5950). This suggests the filamentous "pentagon" structure is not just unique to the doublets of human sperm, but is found in doublets of other human tissues as well. The density in the B-tubule is not resolved in our post-axonemal structure, but is evident in averaged cross sections of sperm axoneme (83), indicating this structure terminates along with other axonemal components.

Based on these data and previously published findings, we hypothesize that the sickle and pentagon structures in the axonemal doublets of human spermatozoa are actually formed by filamentous densities in the A-tubule, a morphology that is unique as compared to the MIPs that have been studied in other organisms (115,139,144,152). In other organisms, much smaller filaments and globular MIPs decorate the microtubule lumen but do not form large filamentous arrangements. Sea urchin flagella also filamentous structures in the same region of the A-tubule (87,144), which have also been suggested to contain tektins (155), although these structures are relatively small compared to the filaments found in human doublets. After the termination of axonemal structures, the sickle density also terminates, as well as the outer dynein arm docking complex. Due to the coincident disappearance of both of these structures in post-axonemal doublets, and their locations on the inside and outside of protofilaments a8 and a9, we hypothesize the sickle plays a role as molecular ruler, and must somehow transfer this information to the outside of the microtubule to regulate spacing of dynein.

After the termination of the sickle density and other axonemal structures, post-axonemal doublets contain only the pentagon filaments and a few other structures. Then, the pentagon structure is replaced by TAILS in the doublets leading up to the singlet region. Although TAILS was not resolved in the B-tubule by SPA, it was found in the B-tubule by subtomogram averaging (27). At the time of writing this thesis, processing of the TAILS-containing doublets is at a preliminary stage, so possibly this will change with better alignment of the flexible B-tubule or further 3D-classification. Finally, doublets either terminate or split to form two complete singlets microtubules containing TAILS, although the details of the splitting process remain to be elucidated.

Concluding Summary

The work in this thesis investigates two very different structures in eukaryotic cells. In both cases, new structural insights gained from EM shed light on possible functions of these structures. In **Paper I**, we explore a phenomenon called nuclear envelope budding (NEB) and discover formation of NEB events to be a conserved feature of the eukaryotic NE. We go on use immune-EM to show that this process is distinct from malfunction of the NPC, and that NEB events contain ubiquitin, indicating they may transport material targeted for degradation. In support of this idea, we show that NEB is upregulated in response to several types of cellular stress: heat shock, oxidative stress, exposure to sodium arsenite, and cellular aging. All of these stressors result in protein misfolding, so we investigate the effect of proteotoxic stress on NEB directly by exposing cells to AZC, a drug that causes misfolding of newly translated proteins, which results in the greatest increase in NEB of all the stressors tested.

In **Paper II,** we present the first review article that focuses specifically on the distal tip region of the flagella. As this region has not received as much attention as the axoneme, we hope this review brings attention to this important area of flagellar function and provides a useful source of information for those entering the field. **Papers III** and **IV** are research papers, which present our labs recent contributions to this field. In **Paper III**, we present the first description of the 3D structure of the tip of the human sperm flagellum by cryo-ET. We confirm old hypotheses (103) that doublet microtubules are able to split into two complete singlet microtubules in the tips of mammalian sperm flagella, and visualize this splitting process directly. In **Paper IV**, produce the first proteome of the flagellum tip, and use SPA to produce a high resolution structure of TAILS, a helical arrangement of unknown proteins that binds within the microtubule lumen in the tip of human sperm flagella that was discovered by our lab, revealing secondary structures of TAILS for the first time as well as the arrangement of TAILS structural elements. We also discover a new structural element, called the zipper, which is smaller than the C-shaped segment of TAILS and binds with two distinct densities alternating every 4 nm. Furthermore, we investigate the evolutionary conservation of TAILS, discovering this structure in the flagella of a total of 3 new organisms **(Paper III and Paper IV**). Furthermore, we describe our initial efforts to identify the proteins that form TAILS, demonstrating how this new structural data will assist in identification of these proteins. The data in **Paper IV** has already generated a short list of TAILS candidate proteins, which will be further investigated by our lab.

Chapter 5 of this thesis, which will serve for the basis of a manuscript once the data processing is completed, also investigates the distal tip of human sperm flagella but focuses on the doublet microtubules that occur in this region. We discover two classes of post-axonemal doublet microtubules, one containing an extensive array of filaments in the A-tubule and another containing TAILS. We present a case that the mysterious filaments correspond to a structure previous referred to as “the pentagon” in axonemal microtubules of human sperm, and that this structure is likely composed of tektins. Further analysis of this dataset will investigate this structure further, and compare the structures of TAILS in doublet vs. singlet microtubules.

In conclusion, the work in this thesis can be thought of as an application of the new “reverse structural biology” approach, in which mysterious structures visualized inside cells by EM are

then probed to reveal both their composition and function. While many mysterious remain concerning NEB and the flagellum tip, this approach has already yielded a wealth of new information about both of these topics.

References

1. Scherzer O. The Theoretical Resolution Limit of the Electron Microscope. J Appl Phys. 1949 Jan;20(1):20–9.

2. Jia CL, Lentzen M, Urban K. Atomic-resolution imaging of oxygen in perovskite ceramics. Science. 2003 Feb 7;299(5608):870–3.

3. Kühlbrandt W. Cryo-EM enters a new era. eLife [Internet]. 2014 Aug 13 [cited 2020 Sep 1];3. Available from: https://www.ncbi.nlm.nih.gov/pmc/articles/PMC4131193/

4. Nakane T, Kotecha A, Sente A, McMullan G, Masiulis S, Brown PMGE, et al. Single-particle cryo-EM at atomic resolution. Nature. 2020 Nov 5;587(7832):152–6.

5. Yu H. Extending the Size Limit of Protein Nuclear Magnetic Resonance. Proc Natl Acad Sci U S A. 1999;96(2):332–4.

6. Herzik MA, Wu M, Lander GC. High-resolution structure determination of sub-100 kDa complexes using conventional cryo-EM. Nat Commun. 2019 Dec;10(1):1032.

7. Dunstone MA, de Marco A. Cryo-electron tomography: an ideal method to study membrane-associated proteins. Philos Trans R Soc B Biol Sci. 2017 Aug 5;372(1726):20160210.

8. Behrmann E, Loerke J, Budkevich TV, Yamamoto K, Schmidt A, Penczek PA, et al. Structural Snapshots of Actively Translating Human Ribosomes. Cell. 2015 May;161(4):845–57.

9. Nguyen VS, Douzi B, Durand E, Roussel A, Cascales E, Cambillau C. Towards a complete structural deciphering of Type VI secretion system. Curr Opin Struct Biol. 2018 Apr;49:77–84.

10. Allegretti M, Zimmerli CE, Rantos V, Wilfling F, Ronchi P, Fung HKH, et al. In-cell architecture of the nuclear pore and snapshots of its turnover. Nature. 2020 Oct 29;586(7831):796–800.

11. Fischer ER, Hansen BT, Nair V, Hoyt FH, Dorward DW. Scanning electron microscopy. Curr Protoc Microbiol. 2012 May;Chapter 2:Unit 2B.2.

12. Harris JR. Transmission electron microscopy in molecular structural biology: A historical survey. Arch Biochem Biophys. 2015 Sep 1;581:3–18.

13. Mielańczyk Ł, Matysiak N, Klymenko O, Wojnicz R. Transmission Electron Microscopy of Biological Samples. In: Maaz K, editor. The Transmission Electron Microscope - Theory and Applications [Internet]. InTech; 2015 [cited 2021 Feb 19]. Available from: http://www.intechopen.com/books/the-transmission-electron-microscope-theory-and-applications/transmission-electron-microscopy-of-biological-samples

14. Lyumkis D. Challenges and opportunities in cryo-EM single-particle analysis. J Biol Chem. 2019 Mar 29;294(13):5181–97.

15. Vanhecke D, Graber W, Studer D. Chapter 9 Close-to-Native Ultrastructural Preservation by High Pressure Freezing. In: Methods in Cell Biology [Internet]. Elsevier; 2008 [cited 2021 Jan 19]. p. 151–64. Available from: https://linkinghub.elsevier.com/retrieve/pii/S0091679X08004093

16. Dubochet J, Sartori Blanc N. The cell in absence of aggregation artifacts. Micron. 2001 Jan;32(1):91–9.

17. Dubochet J, McDowall AW. VITRIFICATION OF PURE WATER FOR ELECTRON MICROSCOPY. J Microsc. 1981 Dec;124(3):3–4.

18. Hall CE, Jakus MA, Schmitt FO. The Structure of Certain Muscle Fibrils as Revealed by the Use of Electron Stains. J Appl Phys. 1945 Aug;16(8):459–65.

19. Scarff CA, Fuller MJG, Thompson RF, Iadanza MG. Variations on Negative Stain Electron Microscopy Methods: Tools for Tackling Challenging Systems. J Vis Exp JoVE. 2018 Feb 6;(132).

20. Dobro MJ, Melanson LA, Jensen GJ, McDowall AW. Plunge freezing for electron cryomicroscopy. Methods Enzymol. 2010;481:63–82.

21. Höög JL, Gluenz E, Vaughan S, Gull K. Ultrastructural Investigation Methods for Trypanosoma brucei. In: Methods in Cell Biology [Internet]. Elsevier; 2010 [cited 2021 Jan 19]. p. 175–96. Available from: https://linkinghub.elsevier.com/retrieve/pii/S0091679X10960081

22. Kishimoto-Okada A, Murakami S, Ito Y, Horii N, Furukawa H, Takagi J, et al. Comparison of the envelope architecture of E. coli using two methods: CEMOVIS and cryo-electron tomography. J Electron Microsc (Tokyo). 2010;59(5):419–26.

23. Schaffer M, Pfeffer S, Mahamid J, Kleindiek S, Laugks T, Albert S, et al. A cryo-FIB lift-out technique enables molecular-resolution cryo-ET within native Caenorhabditis elegans tissue. Nat Methods. 2019 Aug;16(8):757–62.

24. Webster P, Schwarz H, Griffiths G. Preparation of cells and tissues for immuno EM. Methods Cell Biol. 2008;88:45–58.

25. Kremer JR, Mastronarde DN, McIntosh JR. Computer Visualization of Three-Dimensional Image Data Using IMOD. J Struct Biol. 1996 Jan;116(1):71–6.

26. Sanchez RM, Zhang Y, Chen W, Dietrich L, Kudryashev M. Subnanometer-resolution structure determination in situ by hybrid subtomogram averaging - single particle cryo-EM. Nat Commun. 2020 Jul 24;11(1):3709.

27. Zabeo D, Heumann JM, Schwartz CL, Suzuki-Shinjo A, Morgan G, Widlund PO, et al. A lumenal interrupted helix in human sperm tail microtubules. Sci Rep. 2018 Dec;8(1):2727.

28. Li X, Mooney P, Zheng S, Booth CR, Braunfeld MB, Gubbens S, et al. Electron counting and beam-induced motion correction enable near-atomic-resolution single-particle cryo-EM. Nat Methods. 2013 Jun;10(6):584–90.

29. Danev R, Baumeister W. Cryo-EM single particle analysis with the Volta phase plate. eLife. 2016 Mar 7;5.

30. Zhang K. Gctf: Real-time CTF determination and correction. J Struct Biol. 2016 Jan;193(1):1–12.

31. Wagner T, Merino F, Stabrin M, Moriya T, Antoni C, Apelbaum A, et al. SPHIRE-crYOLO is a fast and accurate fully automated particle picker for cryo-EM. Commun Biol. 2019 Dec;2(1):218.

32. Scheres SHW. RELION: implementation of a Bayesian approach to cryo-EM structure determination. J Struct Biol. 2012 Dec;180(3):519–30.

33. Cook AD, Manka SW, Wang S, Moores CA, Atherton J. A microtubule RELION-based pipeline for cryo-EM image processing. J Struct Biol. 2020 Jan;209(1):107402.

34. Zhang R, Nogales E. A new protocol to accurately determine microtubule lattice seam location. J Struct Biol. 2015 Nov;192(2):245–54.

35. He S, Scheres SHW. Helical reconstruction in RELION. J Struct Biol. 2017 Jun;198(3):163–76.

36. Grant T, Rohou A, Grigorieff N. cisTEM, user-friendly software for single-particle image processing. eLife. 2018 Mar 7;7:e35383.

37. Punjani A, Rubinstein JL, Fleet DJ, Brubaker MA. cryoSPARC: algorithms for rapid unsupervised cryo-EM structure determination. Nat Methods. 2017 Mar;14(3):290–6.

38. Zivanov J, Nakane T, Scheres SHW. A Bayesian approach to beam-induced motion correction in cryo-EM single-particle analysis. IUCrJ. 2019 Jan 1;6(Pt 1):5–17.

39. Watson ML. Pores in the mammalian nuclear membrane. Biochim Biophys Acta. 1954 Dec 1;15(4):475–9.

40. Schwartz J, Roizman B. Concerning the egress of herpes simplex virus from infected cells: Electron and light microscope observations. Virology. 1969 May 1;38(1):42–9.

41. Wang I-H, Burckhardt CJ, Yakimovich A, Greber UF. Imaging, Tracking and Computational Analyses of Virus Entry and Egress with the Cytoskeleton. Viruses [Internet]. 2018 Mar 31 [cited 2020 Sep 1];10(4). Available from: https://www.ncbi.nlm.nih.gov/pmc/articles/PMC5923460/

42. Gay H. NUCLEO-CYTOPLASMIC RELATIONS IN SALIVARY-GLAND CELLS OF Drosophila*. Proc Natl Acad Sci U S A. 1955 Jun 15;41(6):370–5.

43. Hadek R, Swift H. Nuclear extrusion and intracisternal inclusions in the rabbit blastocyst. J Cell Biol. 1962 Jun;13:445–51.

44. Afzelius BA. THE NUCLEUS OF NOCTILUCA SCINTILLANS Aspects of Nucleocytoplasmic Exchanges and the Formation of Nuclear Membrane. J Cell Biol. 1963 Oct 1;19(1):229–38.

45. Longwell AC, Yerganian G. Some Observations on Nuclear Budding and Nuclear Extrusions in a Chinese Hamster Cell Culture. JNCI J Natl Cancer Inst. 1965 Jan 1;34(1):53–69.

46. Szollosi D. EXTRUSION OF NUCLEOLI FROM PRONUCLEI OF THE RAT. J Cell Biol. 1965 Jun 1;25(3):545–62.

47. Speese SD, Ashley J, Jokhi V, Nunnari J, Barria R, Li Y, et al. Nuclear envelope budding enables large ribonucleoprotein particle export during synaptic Wnt signaling. Cell. 2012 May 11;149(4):832–46.

48. Jokhi V, Ashley J, Noma A, Ito N, Wakabayashi-Ito N, Moore MJ, et al. Torsin mediates primary envelopment of large ribonucleoprotein granules at the nuclear envelope. Cell Rep. 2013 Apr 25;3(4):988–95.

49. Thaller DJ, Allegretti M, Borah S, Ronchi P, Beck M, Lusk CP. An ESCRT-LEM protein surveillance system is poised to directly monitor the nuclear envelope and nuclear transport system. eLife. 2019 Apr 3;8:e45284.

50. Rose A, Schlieker C. Alternative nuclear transport for cellular protein quality control. Trends Cell Biol. 2012 Oct;22(10):509–14.

51. Shor E, Fox CA, Broach JR. The Yeast Environmental Stress Response Regulates Mutagenesis Induced by Proteotoxic Stress. Jinks-Robertson S, editor. PLoS Genet. 2013 Aug 1;9(8):e1003680.

52. Shibata Y, Morimoto RI. How the Nucleus Copes with Proteotoxic Stress. Curr Biol. 2014 May;24(10):R463–74.

53. Erjavec N, Larsson L, Grantham J, Nystrom T. Accelerated aging and failure to segregate damaged proteins in Sir2 mutants can be suppressed by overproducing the protein aggregation-remodeling factor Hsp104p. Genes Amp Dev. 2007 Oct 1;21(19):2410–21.

54. Mehrtash AB, Hochstrasser M. Ubiquitin-dependent protein degradation at the endoplasmic reticulum and nuclear envelope. Semin Cell Dev Biol. 2019 Sep;93:111–24.

55. Koch B, Yu H-G. Regulation of inner nuclear membrane associated protein degradation. Nucleus. 2019 Jan 1;10(1):169–80.

56. Höög JL, Lacomble S, O'Toole ET, Hoenger A, McIntosh JR, Gull K. Modes of flagellar assembly in Chlamydomonas reinhardtii and Trypanosoma brucei. eLife [Internet]. 2014 Jan 21 [cited 2018 Jul 2];3. Available from: https://elifesciences.org/articles/01479

57. Höög JL, Antony C. Whole-Cell Investigation of Microtubule Cytoskeleton Architecture by Electron Tomography. In: Methods in Cell Biology [Internet]. Academic Press; 2007 [cited 2020 Sep 1]. p. 145–67. (Cellular Electron Microscopy; vol. 79). Available from: http://www.sciencedirect.com/science/article/pii/S0091679X06790069

58. Zeng X-C, Bhasin S, Wu X, Lee J-G, Maffi S, Nichols CJ, et al. Hsp70 dynamics in vivo: effect of heat shock and protein aggregation. J Cell Sci. 2004 Oct 1;117(21):4991–5000.

59. Erjavec N, Larsson L, Grantham J, Nyström T. Accelerated aging and failure to segregate damaged proteins in Sir2 mutants can be suppressed by overproducing the protein aggregation-remodeling factor Hsp104p. Genes Dev. 2007 Oct 1;21(19):2410–21.

60. Weids AJ, Ibstedt S, Tamás MJ, Grant CM. Distinct stress conditions result in aggregation of proteins with similar properties. Sci Rep. 2016 Apr 18;6:24554.

61. Fowden L, Richmond MH. Replacement of proline by azetidine-2-carboxylic acid during biosynthesis of protein. Biochim Biophys Acta. 1963 Jan 1;71:459–61.

62. Trotter EW, Kao CM-F, Berenfeld L, Botstein D, Petsko GA, Gray JV. Misfolded proteins are competent to mediate a subset of the responses to heat shock in Saccharomyces cerevisiae. J Biol Chem. 2002 Nov 22;277(47):44817–25.

63. Berke SJS, Paulson HL. Protein aggregation and the ubiquitin proteasome pathway: gaining the UPPer hand on neurodegeneration. Curr Opin Genet Dev. 2003 Jun;13(3):253–61.

64. Pankiv S, Clausen TH, Lamark T, Brech A, Bruun J-A, Outzen H, et al. p62/SQSTM1 binds directly to Atg8/LC3 to facilitate degradation of ubiquitinated protein aggregates by autophagy. J Biol Chem. 2007 Aug 17;282(33):24131–45.

65. Khaminets A, Behl C, Dikic I. Ubiquitin-Dependent And Independent Signals In Selective Autophagy. Trends Cell Biol. 2016 Jan;26(1):6–16.

66. Kaganovich D, Kopito R, Frydman J. Misfolded proteins partition between two distinct quality control compartments. Nature. 2008 Aug;454(7208):1088–95.

67. Miller SB, Ho C, Winkler J, Khokhrina M, Neuner A, Mohamed MY, et al. Compartment-specific aggregases direct distinct nuclear and cytoplasmic aggregate deposition. EMBO J. 2015 Mar 12;34(6):778–97.

68. Tyedmers J, Treusch S, Dong J, McCaffery JM, Bevis B, Lindquist S. Prion induction involves an ancient system for the sequestration of aggregated proteins and heritable changes in prion fragmentation. Proc Natl Acad Sci. 2010 May 11;107(19):8633–8.

69. Khosrow-Khavar F, Fang NN, Ng AHM, Winget JM, Comyn SA, Mayor T. The Yeast Ubr1 Ubiquitin Ligase Participates in a Prominent Pathway That Targets Cytosolic Thermosensitive Mutants for Degradation. G3amp58 GenesGenomesGenetics. 2012 May;2(5):619–28.

70. Comyn SA, Young BP, Loewen CJ, Mayor T. Prefoldin Promotes Proteasomal Degradation of Cytosolic Proteins with Missense Mutations by Maintaining Substrate Solubility. Gardner R, editor. PLOS Genet. 2016 Jul 22;12(7):e1006184.

71. Wente SR, Blobel G. A temperature-sensitive NUP116 null mutant forms a nuclear envelope seal over the yeast nuclear pore complex thereby blocking nucleocytoplasmic traffic. J Cell Biol. 1993 Oct 15;123(2):275–84.

72. Rempel IL, Crane MM, Thaller DJ, Mishra A, Jansen DP, Janssens G, et al. Age-dependent deterioration of nuclear pore assembly in mitotic cells decreases transport dynamics. Weis K, Akhmanova A, editors. eLife. 2019 Jun 3;8:e48186.

73. Otsuka S, Bui KH, Schorb M, Hossain MJ, Politi AZ, Koch B, et al. Nuclear pore assembly proceeds by an inside-out extrusion of the nuclear envelope. eLife. 2016 Sep 15;5.

74. Hilgendorf KI, Johnson CT, Jackson PK. The primary cilium as a cellular receiver: organizing ciliary GPCR signaling. Curr Opin Cell Biol. 2016 Apr;39:84–92.

75. Pazour GJ, Witman GB. The vertebrate primary cilium is a sensory organelle. Curr Opin Cell Biol. 2003 Feb;15(1):105–10.

76. Bloodgood RA. Sensory reception is an attribute of both primary cilia and motile cilia. J Cell Sci. 2010 Feb 15;123(Pt 4):505–9.

77. Shah AS, Ben-Shahar Y, Moninger TO, Kline JN, Welsh MJ. Motile cilia of human airway epithelia are chemosensory. Science. 2009 Aug 28;325(5944):1131–4.

78. Gadelha C, Wickstead B, Gull K. Flagellar and ciliary beating in trypanosome motility. Cell Motil Cytoskeleton. 2007 Aug;64(8):629–43.

79. Rikmenspoel R. Movement of sea urchin sperm flagella. J Cell Biol. 1978 Feb;76(2):310–22.

80. Silflow CD, Lefebvre PA. Assembly and motility of eukaryotic cilia and flagella. Lessons from Chlamydomonas reinhardtii. Plant Physiol. 2001 Dec;127(4):1500–7.

81. Bustamante-Marin XM, Ostrowski LE. Cilia and Mucociliary Clearance. Cold Spring Harb Perspect Biol. 2017 Apr 3;9(4).

82. Afzelius BA. The immotile-cilia syndrome: a microtubule-associated defect. CRC Crit Rev Biochem. 1985;19(1):63–87.

83. Afzelius BA, Dallai R, Lanzavecchia S, Bellon PL. Flagellar structure in normal human spermatozoa and in spermatozoa that lack dynein arms. Tissue Cell. 1995 Jun;27(3):241–7.

84. Armengot M, Milara J, Mata M, Carda C, Cortijo J. Cilia motility and structure in primary and secondary ciliary dyskinesia. Am J Rhinol Allergy. 2010 Jun;24(3):175–80.

85. Lin J, Yin W, Smith MC, Song K, Leigh MW, Zariwala MA, et al. Cryo-electron tomography reveals ciliary defects underlying human RSPH1 primary ciliary dyskinesia. Nat Commun. 2014 Dec;5(1):5727.

86. Carvalho-Santos Z, Azimzadeh J, Pereira-Leal JB, Bettencourt-Dias M. Evolution: Tracing the origins of centrioles, cilia, and flagella. J Cell Biol. 2011 Jul 25;194(2):165–75.

87. Downing KH, Sui H. Structural insights into microtubule doublet interactions in axonemes. Curr Opin Struct Biol. 2007 Apr;17(2):253–9.

88. Afzelius B. Electron microscopy of the sperm tail; results obtained with a new fixative. J Biophys Biochem Cytol. 1959 Mar 25;5(2):269–78.

89. King SM. Axonemal Dynein Arms. Cold Spring Harb Perspect Biol. 2016 Nov 1;8(11).

90. Sleigh MA, Barlow DI. How are different ciliary beat patterns produced? Symp Soc Exp Biol. 1982;35:139–57.

91. Dentler WL, Rosenbaum JL. Flagellar elongation and shortening in Chlamydomonas. III. structures attached to the tips of flagellar microtubules and their relationship to the directionality of flagellar microtubule assembly. J Cell Biol. 1977 Sep;74(3):747–59.

92. Ringo DL. Flagellar Motion and Fine Structure of the Flagellar Apparatus in Chlamydomonas. J Cell Biol. 1967;33(3):543–71.

93. Melkonian M, Preisig HR. Twist of central pair microtubules in the flagellum of the green flagellate Scourfieldia caeca. Cell Biol Int Rep. 1982 Mar;6(3):269–77.

94. Dentler WL. Structures linking the tips of ciliary and flagellar microtubules to the membrane. J Cell Sci. 1980 Apr;42:207–20.

95. Dentler WL, LeCluyse EL. The effects of structures attached to the tips of tracheal ciliary microtubules on the nucleation of microtubule assembly in vitro. Prog Clin Biol Res. 1982;80:13–8.

96. Vannuccini E, Paccagnini E, Cantele F, Gentile M, Dini D, Fino F, et al. Two classes of short intraflagellar transport train with different 3D structures are present in Chlamydomonas flagella. J Cell Sci. 2016 May 15;129(10):2064–74.

97. Reynolds MJ, Phetruen T, Fisher RL, Chen K, Pentecost BT, Gomez G, et al. The Developmental Process of the Growing Motile Ciliary Tip Region. Sci Rep. 2018 Dec;8(1):7977.

98. Dentler WL. Attachment of the cap to the central microtubules of Tetrahymena cilia. J Cell Sci. 1984 Mar;66:167–73.

99. Melkonian M, Preisig HR. Ultrastructure of the flagellar apparatus in the green flagellateSpermatozopsis similis. Plant Syst Evol. 1984;146(3–4):145–62.

100. Gluenz E, Ginger ML, McKean PG. Flagellum assembly and function during the Leishmania life cycle. Curr Opin Microbiol. 2010 Aug;13(4):473–9.

101. Höög JL, Lacomble S, Bouchet-Marquis C, Briggs L, Park K, Hoenger A, et al. 3D Architecture of the Trypanosoma brucei Flagella Connector, a Mobile Transmembrane Junction. PLoS Negl Trop Dis. 2016 Jan;10(1):e0004312.

102. Zabeo D, Croft JT, Höög JL. Axonemal doublet microtubules can split into two complete singlets in human sperm flagellum tips. FEBS Lett. 2019 May;593(9):892–902.

103. Woolley DM, Nickels SN. Microtubule termination patterns in mammalian sperm flagella. J Ultrastruct Res. 1985 Mar;90(3):221–34.

104. Satir P. Studies on cilia. 3. Further studies on the cilium tip and a “sliding filament” model of ciliary motility. J Cell Biol. 1968 Oct;39(1):77–94.

105. Tamm SL, Tamm S. Visualization of changes in ciliary tip configuration caused by sliding displacement of microtubules in macrocilia of the ctenophore Beroë. J Cell Sci. 1985 Nov;79:161–79.

106. Croft JT, Zabeo D, Subramanian R, Höög JL. Composition, structure and function of the eukaryotic flagellum distal tip. Wakefield JG, Moores CA, editors. Essays Biochem. 2018 Dec 7;62(6):815–28.

107. Fawcett DW. The mammalian spermatozoon. Dev Biol. 1975 Jun;44(2):394–436.

108. Baltz JM, Williams PO, Cone RA. Dense fibers protect mammalian sperm against damage. Biol Reprod. 1990 Sep;43(3):485–91.

109. Zhao W, Li Z, Ping P, Wang G, Yuan X, Sun F. Outer dense fibers stabilize the axoneme to maintain sperm motility. J Cell Mol Med. 2018 Mar;22(3):1755–68.

110. Lindemann CB. Functional significance of the outer dense fibers of mammalian sperm examined by computer simulations with the geometric clutch model. Cell Motil Cytoskeleton. 1996;34(4):258–70.

111. Serres C, Escalier D, David G. Ultrastructural morphometry of the human sperm flagellum with a stereological analysis of the lengths of the dense fibres. Biol Cell. 1983;49(2):153–61.

112. Eddy EM, Toshimori K, O'Brien DA. Fibrous sheath of mammalian spermatozoa. Microsc Res Tech. 2003 May 1;61(1):103–15.

113. Ichikawa M, Bui KH. Microtubule Inner Proteins: A Meshwork of Luminal Proteins Stabilizing the Doublet Microtubule. BioEssays News Rev Mol Cell Dev Biol. 2018 Mar;40(3).

114. Nicastro D, Schwartz C, Pierson J, Gaudette R, Porter ME, McIntosh JR. The molecular architecture of axonemes revealed by cryoelectron tomography. Science. 2006 Aug 18;313(5789):944–8.

115. Ma M, Stoyanova M, Rademacher G, Dutcher SK, Brown A, Zhang R. Structure of the Decorated Ciliary Doublet Microtubule. Cell. 2019 Oct 31;179(4):909-922.e12.

116. Dymek EE, Lin J, Fu G, Porter ME, Nicastro D, Smith EF. PACRG and FAP20 form the inner junction of axonemal doublet microtubules and regulate ciliary motility. Mol Biol Cell. 2019 Jul 15;30(15):1805–16.

117. Owa M, Uchihashi T, Yanagisawa H-A, Yamano T, Iguchi H, Fukuzawa H, et al. Inner lumen proteins stabilize doublet microtubules in cilia and flagella. Nat Commun. 2019 Mar 8;10(1):1143.

118. Khalifa AAZ, Ichikawa M, Dai D, Kubo S, Black CS, Peri K, et al. The inner junction complex of the cilia is an interaction hub that involves tubulin post-translational modifications. eLife. 2020 Jan 17;9.

119. O'Hagan R, Piasecki BP, Silva M, Phirke P, Nguyen KCQ, Hall DH, et al. The Tubulin Deglutamylase CCPP-1 Regulates the Function and Stability of Sensory Cilia in C. elegans. Curr Biol. 2011 Oct;21(20):1685–94.

120. O'Hagan R, Silva M, Nguyen KCQ, Zhang W, Bellotti S, Ramadan YH, et al. Glutamylation Regulates Transport, Specializes Function, and Sculpts the Structure of Cilia. Curr Biol. 2017 Nov;27(22):3430-3441.e6.

121. Silva M, Morsci N, Nguyen KCQ, Rizvi A, Rongo C, Hall DH, et al. Cell-Specific α-Tubulin Isotype Regulates Ciliary Microtubule Ultrastructure, Intraflagellar Transport, and Extracellular Vesicle Biology. Curr Biol. 2017 Apr;27(7):968–80.

122. Howes SC, Geyer EA, LaFrance B, Zhang R, Kellogg EH, Westermann S, et al. Structural and functional differences between porcine brain and budding yeast microtubules. Cell Cycle Georget Tex. 2018;17(3):278–87.

123. Satish Tammana TV, Tammana D, Diener DR, Rosenbaum J. Centrosomal protein CEP104 (Chlamydomonas FAP256) moves to the ciliary tip during ciliary assembly. J Cell Sci. 2013 Nov 1;126(21):5018–29.

124. Woolley D, Gadelha C, Gull K. Evidence for a sliding-resistance at the tip of the trypanosome flagellum. Cell Motil Cytoskeleton. 2006 Dec;63(12):741–6.

125. Jordan MA, Diener DR, Stepanek L, Pigino G. The cryo-EM structure of intraflagellar transport trains reveals how dynein is inactivated to ensure unidirectional anterograde movement in cilia. Nat Cell Biol. 2018 Nov;20(11):1250–5.

126. Baker MA, Reeves G, Hetherington L, Müller J, Baur I, Aitken RJ. Identification of gene products present in Triton X-100 soluble and insoluble fractions of human spermatozoa lysates using LC-MS/MS analysis. Proteomics Clin Appl. 2007 May;1(5):524–32.

127. Baker MA, Naumovski N, Hetherington L, Weinberg A, Velkov T, Aitken RJ. Head and flagella subcompartmental proteomic analysis of human spermatozoa. Proteomics. 2013 Jan;13(1):61–74.

128. Amaral A, Castillo J, Estanyol JM, Ballescà JL, Ramalho-Santos J, Oliva R. Human sperm tail proteome suggests new endogenous metabolic pathways. Mol Cell Proteomics MCP. 2013 Feb;12(2):330–42.

129. Wang G, Guo Y, Zhou T, Shi X, Yu J, Yang Y, et al. In-depth proteomic analysis of the human sperm reveals complex protein compositions. J Proteomics. 2013 Feb 21;79:114–22.

130. Jumeau F, Chalmel F, Fernandez-Gomez F-J, Carpentier C, Obriot H, Tardivel M, et al. Defining the human sperm microtubulome: an integrated genomics approach. Biol Reprod. 2017 Jan 1;96(1):93–106.

131. Ho C-M, Li X, Lai M, Terwilliger TC, Beck JR, Wohlschlegel J, et al. Bottom-up structural proteomics: cryoEM of protein complexes enriched from the cellular milieu. Nat Methods. 2020 Jan;17(1):79–85.

132. Brown A, Long F, Nicholls RA, Toots J, Emsley P, Murshudov G. Tools for macromolecular model building and refinement into electron cryo-microscopy reconstructions. Acta Crystallogr D Biol Crystallogr. 2015 Jan 1;71(Pt 1):136–53.

133. Kikkawa M, Ishikawa T, Nakata T, Wakabayashi T, Hirokawa N. Direct visualization of the microtubule lattice seam both in vitro and in vivo. J Cell Biol. 1994 Dec;127(6 Pt 2):1965–71.

134. Nogales E, Wolf SG, Downing KH. Structure of the alpha beta tubulin dimer by electron crystallography. Nature. 1998 Jan 8;391(6663):199–203.

135. Alushin GM, Lander GC, Kellogg EH, Zhang R, Baker D, Nogales E. High-Resolution Microtubule Structures Reveal the Structural Transitions in αβ-Tubulin upon GTP Hydrolysis. Cell. 2014 May;157(5):1117–29.

136. Rohou A, Grigorieff N. CTFFIND4: Fast and accurate defocus estimation from electron micrographs. J Struct Biol. 2015 Nov;192(2):216–21.

137. Manka SW, Moores CA. The role of tubulin-tubulin lattice contacts in the mechanism of microtubule dynamic instability. Nat Struct Mol Biol. 2018 Jul;25(7):607–15.

138. Manka SW, Moores CA. Microtubule structure by cryo-EM: snapshots of dynamic instability. Essays Biochem. 2018 Dec 7;62(6):737–51.

139. Ichikawa M, Liu D, Kastritis PL, Basu K, Hsu TC, Yang S, et al. Subnanometre-resolution structure of the doublet microtubule reveals new classes of microtubule-associated proteins. Nat Commun. 2017 May 2;8:15035.

140. Zhang R, LaFrance B, Nogales E. Separating the effects of nucleotide and EB binding on microtubule structure. Proc Natl Acad Sci. 2018 Jul 3;115(27):E6191–200.

141. Waterhouse A, Bertoni M, Bienert S, Studer G, Tauriello G, Gumienny R, et al. SWISS-MODEL: homology modelling of protein structures and complexes. Nucleic Acids Res. 2018 Jul 2;46(W1):W296–303.

142. Yang J, Yan R, Roy A, Xu D, Poisson J, Zhang Y. The I-TASSER Suite: protein structure and function prediction. Nat Methods. 2015 Jan;12(1):7–8.

143. Wu P-K, Hong S-K, Starenki D, Oshima K, Shao H, Gestwicki JE, et al. Mortalin/HSPA9 targeting selectively induces KRAS tumor cell death by perturbing mitochondrial membrane permeability. Oncogene. 2020 May;39(21):4257–70.

144. Nicastro D, Fu X, Heuser T, Tso A, Porter ME, Linck RW. Cryo-electron tomography reveals conserved features of doublet microtubules in flagella. Proc Natl Acad Sci. 2011 Oct 18;108(42):E845–53.

145. Afzelius BA, Bellon PL, Dallai R, Lanzavecchia S. Diversity of microtubular doublets in insect sperm tails: A computer-aided image analysis. Cell Motil Cytoskeleton. 1991;19(4):282–9.

146. Bui KH, Sakakibara H, Movassagh T, Oiwa K, Ishikawa T. Molecular architecture of inner dynein arms in situ in Chlamydomonas reinhardtii flagella. J Cell Biol. 2008 Dec 1;183(5):923–32.

147. Nicastro D, McIntosh JR, Baumeister W. 3D structure of eukaryotic flagella in a quiescent state revealed by cryo-electron tomography. Proc Natl Acad Sci U S A. 2005 Nov 1;102(44):15889–94.

148. Heuser T, Raytchev M, Krell J, Porter ME, Nicastro D. The dynein regulatory complex is the nexin link and a major regulatory node in cilia and flagella. J Cell Biol. 2009 Dec 14;187(6):921–33.

149. Carbajal-González BI, Heuser T, Fu X, Lin J, Smith BW, Mitchell DR, et al. Conserved structural motifs in the central pair complex of eukaryotic flagella. Cytoskelet Hoboken NJ. 2013 Feb;70(2):101–20.

150. Barber CF, Heuser T, Carbajal-González BI, Botchkarev VV, Nicastro D. Three-dimensional structure of the radial spokes reveals heterogeneity and interactions with dyneins in Chlamydomonas flagella. Mol Biol Cell. 2012 Jan;23(1):111–20.

151. Oda T, Yanagisawa H, Kamiya R, Kikkawa M. A molecular ruler determines the repeat length in eukaryotic cilia and flagella. Science. 2014 Nov 14;346(6211):857–60.

152. Nicastro D. The Molecular Architecture of Axonemes Revealed by Cryoelectron Tomography. Science. 2006 Aug 18;313(5789):944–8.

153. Paul DM, Mantell J, Borucu U, Coombs J, Surridge KJ, Squire JM, et al. In situ cryo-electron tomography reveals filamentous actin within the microtubule lumen. J Cell Biol. 2020 Sep 7;219(9):e201911154.

154. Merino F, Pospich S, Funk J, Wagner T, Küllmer F, Arndt H-D, et al. Structural transitions of F-actin upon ATP hydrolysis at near-atomic resolution revealed by cryo-EM. Nat Struct Mol Biol. 2018 Jun;25(6):528–37.

155. Amos LA. The tektin family of microtubule-stabilizing proteins. Genome Biol. 2008;9(7):229.

156. Pirner MA, Linck RW. Methods for the isolation of tektins and Sarkosyl-insoluble protofilament ribbons. Methods Cell Biol. 1995;47:373–80.

157. Pirner MA, Linck RW. Tektins are heterodimeric polymers in flagellar microtubules with axial periodicities matching the tubulin lattice. J Biol Chem. 1994 Dec 16;269(50):31800–6.

158. Lin H, Zhang Z, Guo S, Chen F, Kessler JM, Wang YM, et al. A NIMA-Related Kinase Suppresses the Flagellar Instability Associated with the Loss of Multiple Axonemal Structures. PLoS Genet. 2015 Sep;11(9):e1005508.